



저작자표시-비영리-변경금지 2.0 대한민국

이용자는 아래의 조건을 따르는 경우에 한하여 자유롭게

- 이 저작물을 복제, 배포, 전송, 전시, 공연 및 방송할 수 있습니다.

다음과 같은 조건을 따라야 합니다:



저작자표시. 귀하는 원저작자를 표시하여야 합니다.



비영리. 귀하는 이 저작물을 영리 목적으로 이용할 수 없습니다.



변경금지. 귀하는 이 저작물을 개작, 변형 또는 가공할 수 없습니다.

- 귀하는, 이 저작물의 재이용이나 배포의 경우, 이 저작물에 적용된 이용허락조건을 명확하게 나타내어야 합니다.
- 저작권자로부터 별도의 허가를 받으면 이러한 조건들은 적용되지 않습니다.

저작권법에 따른 이용자의 권리는 위의 내용에 의하여 영향을 받지 않습니다.

이것은 [이용허락규약\(Legal Code\)](#)을 이해하기 쉽게 요약한 것입니다.

[Disclaimer](#)

공학박사학위논문

3차원 유한요소를 이용한 회전 복합재
블레이드의 구조동역학 특성에 관한 연구

**Study on Structural Dynamic Characteristics of
Rotating Composite Blades Using
Three Dimensional Finite Elements**

2015년 2월

서울대학교 대학원

기계항공공학부

기영중

3차원 유한요소를 이용한 회전 복합재
블레이드의 구조동역학 특성에 관한 연구

**Study on Structural Dynamic Characteristics of
Rotating Composite Blades Using
Three Dimensional Finite Elements**

지도교수 신 상 준

이 논문을 공학박사 학위논문으로 제출함

2014년 12월

서울대학교 대학원

기계항공공학부

기 영 중

기영중의 공학박사 학위논문을 인준함

2014년 12월

위원장	김 용 혁	
부위원장	신 상 준	
위원	정 성 남	
위원	이 관 중	
위원	김 능 호	

Abstract

Study on Structural Dynamic Characteristics of Rotating Composite Blades Using Three Dimensional Finite Elements

Young-Jung Kee

School of Mechanical and Aerospace Engineering

The Graduate School

Seoul National University

In this thesis, an eighteen-node solid-shell finite element was used for structural dynamics modeling of rotating composite blades. The analysis model includes the effects of transverse shear deformation, Coriolis effect and elastic couplings due to the anisotropic material behavior. Also, the out of plane warping was included without complicated assumptions for specific beam, plate or shell theories. The incremental total-Lagrangian approach was adopted to allow estimation on arbitrarily large rotations and displacements. The equations of motion for the finite element model were derived using Hamilton's principle, and the resulting nonlinear equilibrium equations were solved by utilizing Newton-Raphson method combined with the load control. A modified stress-strain relation was adopted to avoid the transverse shear

locking problem, and fairly reliable results were obtained with no sign of the locking phenomenon. In order to reduce the computational complexity of the problem, the Guyan and IRS reduction methods were adopted. Those model reduction methods gave not only reliable solutions, but also less computational effort for any geometric configurations and boundary conditions. The present numerical results were compared to the several benchmark problems, and the results show a good correlation with the experimental data and other finite element analysis results. The vibration characteristics of shell and beam type blades were investigated. For the case of shell type blades, blade curvature, pre-twist and geometric nonlinearity may significantly influence the dynamic characteristics, and only the geometric nonlinear analysis model can capture significant drops in frequency and frequency loci veering phenomena. For the case of beam type blades, one-dimensional beam and three-dimensional solid models give comparable prediction for the straight and large aspect ratio blade. As decreasing in the blade aspect ratio, considerable differences appear in bending and torsion modes. The tip sweep angle tends to decrease the flap bending frequencies, but the torsion frequency increases with the tip sweep angle. On the contrary, the tip anhedral enforces to decrease the torsion frequency.

**Keywords: Geometric Nonlinearity, Rotating Composite Blade,
Solid Element, Structural Dynamics Model,
Vibration Analysis**

Student Number: 2011-30946

Contents

	Page
Abstract	i
Contents	iii
List of Tables	vi
List of Figures	vii
List of Symbols	xi
Chapter 1. Introduction	1
1.1 Background.....	1
1.2 Literature Review	4
1.2.1 Beam Models.....	4
1.2.2 Plate and Shell Models.....	6
1.3 Objectives and Layout of Thesis	14
Chapter 2. Geometrically Nonlinear Formulation	17
2.1 Introduction.....	17
2.2 Strain and Stress Tensors	21
2.3 Strain Energy	23
2.4 Kinetic Energy	24
2.5 Equations of Motion	28
2.6 Composite Structures.....	30

Chapter 3. Finite Element Formulation.....	36
3.1 Coordinate Systems	37
3.1.1 Global Coordinate System	37
3.1.2 Local Coordinate System	37
3.1.3 Natural Coordinate System	40
3.2 Element Geometry and Displacement Field	40
3.3 Strain-Displacement Relation	41
3.4 Derivation of Matrices and Vectors	43
3.5 Layer-wise Thickness Integration	46
3.6 Nonlinear Solution Techniques	49
3.7 Model Reduction Method	55
3.7.1 Static Reduction.....	56
3.7.2 IRS(Improved Reduction System) Reduction	57
Chapter 4. Verification Problems	58
4.1 Static Behavior	58
4.1.1 Cantilevered Beam under Shear Force.....	58
4.1.2 Ring Plate under the Uniform Line Load.....	63
4.1.3 Pinched Semi-Cylindrical Shell.....	68
4.2 Dynamic Behavior.....	73

4.2.1 Plate-Type Blade Model	73
4.2.2 Shell-Type Blade Model	77
Chapter 5. Vibration Analysis of Shell Type Blades	80
5.1 Effect of Geometric Nonlinearity	80
5.1.1 Shallow Shell Model	80
5.1.2 Deep Shell Model	84
5.2 Effect of Pre-twist	89
Chapter 6. Vibration Analysis of Beam Type Blades	96
6.1 Effect of Tip Sweep Angle	97
6.1.1 Isotropic Blade Models	98
6.1.2 Composite Blade Models	110
6.2 Effect of Tip Sweep Ratio	122
6.3 Effect of Tip Anhedral	128
Chapter 7. Conclusions	133
7.1 Summary	133
7.2 Future Works	137
References	138
Appendix A	147
Appendix B	150
Appendix C	152
국문초록	154

List of Tables

	Page
Table 1. Material properties of the ring plate.....	64
Table 2. Material properties of the semi-cylindrical shell	69
Table 3. Nondimensional frequencies of pre-twisted plates: $L/C=1$, $C/h=20$	75
Table 4. Nondimensional frequencies of pre-twisted plates: $L/C=1$, $C/h=5$	76
Table 5. Natural frequencies (Hz) of an open cylindrical shell blade	78
Table 6. Material properties of E-glass/Epoxy	91
Table 7. Nondimensional frequencies of the twisted cantilevered shells with $L/C=1$, $C=305\text{mm}$, $C/t=100$, $R_x=2C$	92
Table 8. Mode shapes of the twisted cantilevered shells with $L/C=1$, $C=305\text{mm}$, $C/t=100$, $R_x=2C$, $\bar{\Omega}=1.0$	93
Table 9. Nondimensional frequencies of the twisted cantilevered shells with $L/C=1$, $C=305\text{mm}$, $C/t=100$, $R_x=C$	94
Table 10. Mode shapes of the twisted cantilevered shells with $L/C=1$, $C=305\text{mm}$, $C/t=100$, $R_x=C$, $\bar{\Omega}=1.0$	95
Table 11. Material properties of the composite beam type blade.....	112

List of Figures

	Page
Fig. 1 Various types of rotating blade in engineering practice	3
Fig. 2 Degeneration process of shell structure to solid-shell and degenerated shell elements.....	13
Fig. 3 Initial and deformed configurations of a solid body	20
Fig. 4 Configuration of a rotating twisted blade	27
Fig. 5 An example of fiber reinforced composites.....	33
Fig. 6 Material directions of a laminated layer and the local coordinate system	34
Fig. 7 Transformation of material properties between global, local and principal material coordinate system	35
Fig. 8 Configurations and coordinates of the 18-node solid-shell element	39
Fig. 9 The transformation of the natural thickness coordinate to a layer- wise natural coordinate	48
Fig. 10 Solution procedure for the static and dynamic analysis	54
Fig. 11 Cantilevered beam subject to a shear force, $P_{\max}=4\text{kN}$	60
Fig. 12 Deformed configurations of cantilevered beam for various load steps	61

Fig. 13 Cantilevered beam, load-deflection curves predicted at point A	62
Fig. 14 Ring plate under the uniform line load, $P_{\max}=0.45\text{N/m}$	65
Fig. 15 Deformed configuration of ring plate under the uniform line load	66
Fig. 16 Ring plate, load-deflection curves predicted at point B	67
Fig. 17 Semi-cylindrical shell subject to a concentrated load, $P_{\max}=2\text{kN}$	70
Fig. 18 Deformed configuration of semi-cylindrical shell subject to a concentrated tip load	71
Fig. 19 Semi-cylindrical shell, load-deflection curves predicted at point A	72
Fig. 20 Configuration of a rotating shell type blade	79
Fig. 21 Non-dimensional frequencies of the shallow shell model, $R_x=2L$	82
Fig. 22 Vertical defections of the shallow shell model, $R_x=2L$	83
Fig. 23 Non-dimensional frequencies of the deep shell model, $R_x=L$	86
Fig. 24 Vertical defections of the deep shell model, $R_x=L$	87
Fig. 25 Nodal line patterns of the second and third mode, deep shell model, $R_x=L$	88
Fig. 26 Configuration of the beam-type blade with tip sweep and tip anhedral	100

Fig. 27 Natural frequencies versus rotating speed (isotropic, $\Lambda=0^\circ$, AR=37.5).....	101
Fig. 28 Natural frequencies versus rotating speed (isotropic, $\Lambda=15^\circ$, AR=37.5).....	102
Fig. 29 Natural frequencies versus rotating speed (isotropic, $\Lambda=30^\circ$, AR=37.5).....	103
Fig. 30 Natural frequencies versus rotating speed (isotropic, $\Lambda=45^\circ$, AR=37.5).....	104
Fig. 31 Natural frequencies versus rotating speed (isotropic, $\Lambda=0^\circ$, AR=12.5).....	106
Fig. 32 Natural frequencies versus rotating speed (isotropic, $\Lambda=15^\circ$, AR=12.5).....	107
Fig. 33 Natural frequencies versus rotating speed (isotropic, $\Lambda=30^\circ$, AR=12.5).....	108
Fig. 34 Natural frequencies versus rotating speed (isotropic, $\Lambda=45^\circ$, AR=12.5).....	109
Fig. 35 Natural frequencies versus rotating speed (orthotropic, $[0^\circ]_{24}$, $\Lambda=0^\circ$).....	113
Fig. 36 Natural frequencies versus rotating speed (orthotropic, $[0^\circ]_{24}$, $\Lambda=45^\circ$).....	114
Fig. 37 Natural frequencies versus rotating speed (orthotropic, $[15^\circ]_{24}$, $\Lambda=0^\circ$).....	115

Fig. 38 Natural frequencies versus rotating speed (orthotropic, $[15^\circ]_{24}$, $\Lambda=45^\circ$).....	116
Fig. 39 Natural frequencies versus fiber angles ($\Lambda=0^\circ$, 0 rpm)	118
Fig. 40 Natural frequencies versus fiber angles ($\Lambda=0^\circ$, 750 rpm).....	119
Fig. 41 Natural frequencies versus fiber angles ($\Lambda=45^\circ$, 0 rpm).....	120
Fig. 42 Natural frequencies versus fiber angles ($\Lambda=45^\circ$, 750 rpm).....	121
Fig. 43 Influence of the swept tip ratio on the natural frequencies: the first flap bending mode	124
Fig. 44 Influence of the swept tip ratio on the natural frequencies: the second flap bending mode.....	125
Fig. 45 Influence of the swept tip ratio on the natural frequencies: the first lag bending mode	126
Fig. 46 Influence of the swept tip ratio on the natural frequencies: the first torsion mode.....	127
Fig. 47 Influence of the tip anhedral on the natural frequencies: the first flap bending mode	129
Fig. 48 Influence of the tip anhedral on the natural frequencies: the second flap bending mode.....	130
Fig. 49 Influence of the tip anhedral on the natural frequencies: the first lag bending mode.....	131
Fig. 50 Influence of the tip anhedral on the natural frequencies: the first torsion mode.....	132

List of Symbols

Symbols	Meaning
iA	Area at i-th configuration
$\mathbf{a}_1, \mathbf{a}_2, \mathbf{a}_3$	Direction cosines of the local axes with respect to the global axes
$\mathbf{A}_e, \mathbf{A}_\eta$	Linear and nonlinear displacement gradient matrices
\mathbf{B}	Strain-displacement relation matrix
C_i	Reference configuration at i-th configuration
\mathbf{C}	Damping matrix
$\mathbf{e}_i, \mathbf{e}_j, \mathbf{e}_k$	Unit vector of inertial frame
$\mathbf{e}_x, \mathbf{e}_y, \mathbf{e}_z$	Unit vector of global coordinate
\mathbf{F}_{CF}	Centrifugal force vector
\mathbf{g}_i	Covariant base vectors at the centroid of element
\mathbf{H}	Unknown displacement gradient vector
\mathbf{J}	Jacobian matrix
\mathbf{K}_L	Linear stiffness matrix
\mathbf{K}_{NL}	Nonlinear stiffness matrix
\mathbf{K}_{CF}	Stiffness matrix due to the centrifugal force
\mathbf{K}_T	Tangent stiffness matrix
\mathbf{M}	Mass matrix
N_k	Shape functions

P	Shape function derivative matrix
Symbols	Meaning
Q_{ijrs}	Constitutive tensor components
q	Nodal displacement vector
r	Position vector of a point in deformed blade
R_I	Internal force vector due to the force unbalance
R_E	External force vector
R	Unbalance force vector
S_{ij}	2 nd Piola-Kirchhoff stress tensor components
T_L	Transformation matrix between local and material coordinates
T_G	Transformation matrix between global and local coordinates
T_Ω	Transformation matrix between inertial and global coordinates
T_S	Guyan transformation matrix
T_{IRS}	IRS transformation matrix
u	Displacement increment of the point form configuration C_1 to C_2
iV	Volume at i-th configuration
${}^i\mathbf{x}$	Position vectors at i-th configuration
x, y, z	Global coordinate system
x', y', z'	Local coordinate system

ε_{ij}	Green-Lagrangian strain tensor components
Symbols	Meaning
e_{ij}	Linear components of the Green-Lagrangian strain tensors
η_{ij}	Nonlinear components of the Green-Lagrangian strain tensors
${}^i\rho$	Density at i-th configuration
Λ	Tip sweep angle
$\bar{\Omega}$	Nondimensional rotating speed
$\bar{\omega}$	Nondimensional frequency parameter
ϕ	Pre-twist angle
Γ	Tip anhedral angle
σ_{ij}	Cauchy stress tensor components
ξ, η, ζ	Natural coordinate system

Chapter 1. Introduction

1.1 Background

Rotating blades that withstand centrifugal force, as well as flap bending, lead-lag bending, and torsional moments are one of the most important structural elements in the aerospace and mechanical industries. It is well known that the rotating motion of a flexible structure can significantly influence its dynamic characteristics. The natural frequencies of rotating blades, for instance, are known to be higher than those for non-rotating blades. Due to the importance of such a motion-induced stiffness variation effect, dynamic analysis of rotating blades has been widely conducted to examine the influence on resonance or aeroelastic instability. Moreover, in accordance with advances in aerospace technology, composite materials show great potential for the design of rotating blades because of their advantages in strength, durability, and weight. This enforces the blade to be subject to transverse shear deformation, geometric nonlinearities, cross-sectional warping, and various elastic coupling. Thus, it is necessary to predict the structural dynamic characteristics of those structures accurately and efficiently for reliable designs.

As shown in Fig. 1, rotating blades used in turbo-machines, helicopters, wind turbines, and other engineering practice have been modeled by various structural models. Most advances have been made

through the use of the beam formulation. Its modeling spanned from a simple Euler–Bernoulli’s beam to a twisted Timoshenko’s beam subject to centrifugal tension force. While beam formulations may be adequate for a high aspect ratio blade ($AR \gg 10$), these models may be inaccurate for predicting higher frequencies. For higher modes of vibration, the blade will behave more like a plate or shell rather than a one-dimensional beam. Also, as the aspect ratio of a blade decrease, the chord-wise bending modes will become involved in the vibration, and beam approaches will be unable to capture those modes. Rotating plates have been considered as more rigorous models for low aspect ratio blades. A great number of research works have dealt with the free vibration of rotating plates, while investigating the effects of pretwist angle, thickness ratio, aspect ratio, skew angle and precone angle upon natural frequencies. In recent years, most of industries have considered using of advanced configurations of blade to improve the aerodynamic performance and reduce the vibratory loads and noise. In case of turbomachinery blades, those advanced configurations include the large curvatures and twists. Also, three types of advanced tip configurations have been applied to the rotorcraft blades. In the USA, the simple sheared-swept or swept-tapered-anhedral tip represents the state of the art. The parabolic tip has been widely adopted in Europe, except in the UK where the BERP tip remains a unique option. Accurate analysis of such structures requires sophisticated three-dimensional shell model rather than beam or plate models.



(a) Unducted fan blades



(b) Wind turbine blades



(c) Helicopter rotor blades (BERP-IV)

Fig. 1 Various types of rotating blade in engineering practice

1.2 Literature Review

1.2.1 Beam Models

Since it is usually difficult to obtain a closed-form solution for beam equations, various approximate methods have been suggested to investigate the dynamic characteristics of rotating beams. Southwell and Gough [1] investigated the natural frequencies of the rotating beams analytically. They proposed an explicit equation that was capable of evaluating the natural frequencies of rotating beams in terms of their rotating frequency. Development of equations of motion for general pretwisted and rotating turbo-machinery blades was conducted by Carnegie [2] and Dawson [3] based on the beam model using a theoretical expression for potential energy in Rayleigh's method. Putter and Monor [4], Kaza and Kielb [5] and Ansari [6] studied the natural frequencies of tapered blades, the effects of warping and pretwist angle on torsional vibration, and the effects of shear deformation, rotary inertia, and Coriolis effects. Yoo et al. [7, 8] investigated the eigen-value loci veering phenomenon and applied a multibody theory to investigate the complex rotating structure comprising of several beams.

Rotating blades used in rotorcrafts are representative examples of structures that have the shape of thin or thick walled beams. Numerous researchers have investigated the vibrations of thin or thick walled beams. Rehfield [9] studied the design analysis methodology of a thin-walled beam for composite rotor blades. Chandra and Chopra [10]

investigated the vibration characteristics of rotating composite box beams by both experimental and theoretical methods. Smith and Chopra [11] suggested the structural model of the blade spar that includes the effects of transverse shear deformation, two-dimensional in-plane elasticity and torsion-related out of plane warping. In addition, Jung et al. [12] proposed a refined beam formulation based on a mixed variational approach with general section shape and studied the effects of wall thickness and first-order transverse shear deformation on free vibration behavior. Recently, Cesnik [13] and Hodges [14] proposed hybrid beam models that split the problem into a generally linear two-dimensional problem over the cross sectional plane and a nonlinear global one-dimensional analysis. Therefore, an approach commonly used in the structural models for composite rotor blade analysis is to determine the cross section warping functions, shear center location, and cross sectional properties based on a linear theory. The linear two-dimensional analysis for the cross section is decoupled from the nonlinear one-dimensional global analysis for the beam and it needs to be done for each cross section analysis of a nonuniform beam.

Although beam models are adequate for a high aspect ratio blade, Leissa and Ewing [15] investigated the accuracy and limitation of beam formulations. They insisted that beam formulations would generally be inadequate to determine the frequencies and mode shapes for low aspect ratio blades. Recently, new approaches have been suggested to develop a rotorcraft blade structural model based on the two-dimensional shell or

three-dimensional brick elements. Datta and Johnson [16] demonstrated a parallel and scalable solution procedure of a three-dimensional brick finite element for dynamic analysis of helicopter rotor blades. Yeo, et al [17] assessed the validity of one-dimensional beam theories for rotor blade application. They compared the natural frequencies of one dimensional beam model in RCAS and three-dimensional model from MSC/Patran and MSC/Mark. Kang, et al. [18] introduced a geometrically exact shell element and reported an assessment of beam and shell elements for modeling rotorcraft blades. The shell element was formulated based on the shallow shell assumption. Heo and Bauchau [19] adopted the shell elements to develop a structural model of curved blades and suggested domain decomposition techniques to reduce the computational cost of the problem.

1.2.2 Plate and Shell Models

A structural element with one dimension, the thickness, being much smaller than the two others one can be categorized as a thin-walled surface structure or a shell. And then a plate is just a special case of a shell characterized by a flat surface.

(1) Plate Models

In case of low aspect ratio blades, the blade behaves like a plate

rather than a beam. Dokainish and Rawtani [20] adopted a finite element method to determine the dynamic characteristics of rotating cantilevered plates mounted on a rotating rigid hub. Ramamurti and Kielb [21] extended and applied their work to analyze the vibration of a twisted plate. Other researchers [22, 23] have dealt with the free vibration of rotating plates, while investigating the effects of thickness ratio, aspect ratio, skew angle and precone angle upon natural frequencies. Bhumbra et al. [24] studied the natural frequencies and mode shapes of spinning laminated composite plates by using a geometrically nonlinear formulation. Yoo and Pierre [25] used the Kane's method to model a rotating blade while applying the plate theory, and investigated the effects of the dimensionless design parameters on the modal characteristics of rotating cantilevered plates.

(2) Shell Models

In general, four kinds of the shell elements in the previous work were proved to be successful and showed high performance. Those elements are the curved elements, flat elements, degenerated elements, and solid-shell elements as follows.

Flat Shell Elements

A shell is considered as a curved form of a plate and its structural behavior is a combination of stretching and bending. It is possible to

perform a finite element analysis of a shell by using what is called a facet representation. Therefore, the shell surface is replaced by a flat triangular or quadrilateral plate element in which a membrane stiffness is superposed on a bending stiffness.

Greene et al [26] proposed the use of flat element to analyze shell structures. Since then, many flat shell elements which superimpose plate bending and plane stress element without normal rotation were developed. To formulate a shell element with six degrees of freedom (DOF) per node, many researchers contributed to the development of the drilling DOF. Hughes and Brezzi [27], and Ibranhimbegovic et al. [28] employed an independent rotation field to construct the drilling DOF.

Most of the early bending plate elements in the flat shell elements were based on the Kirchhoff thin plate theory and a number of excellent performance elements were developed, such as discrete Kirchhoff quadrilateral element by Batoz et al. [29]. However, these elements are limited to the thin plates due to the assumption of zero shear strain energy. To develop a general plate element, which considers arbitrary thickness, the Reissner-Mindlin plate theory has been widely employed. In the early stage of its development, the shear locking phenomenon is a key issue and attracts attention from many researchers about its solution. A number of researchers, such as Zienkiewicz and Hinton [30], Bathe and Dvorkin [31], Hinton and Huang [32], and Belytschko and Bindeman [33], made great contributions on this development.

The advantages and disadvantages of the flat the type shell elements

against other types of elements were summarized by Yang et al. [34]. Generally, the formulations of this element are relative simple. However, the bending and membrane parts in this type of elements are uncoupled at the element level. Such uncoupling may have significant influence on the curved structures.

Curved Shell Elements

The formulation of the classical curved thin shell elements based on the shell theories is generally quite complicated. Conner and Brebbia [35] first proposed a rectangular thin shell element on the basis of the shallow shell assumptions. Also, Surana [36] proposed a curved shell element for thick and thin shell structures including geometrically nonlinearity. Recently, Li and Vu-Quoc [37] developed a curved triangular shell element based on the co-rotational framework to solve large displacement and rotation problems.

Leissa et al. [38] were the first researchers to investigate the free vibration characteristics of cantilevered rotating shell-type blades. They studied the influence of parameters such as rotating speed, pretwist, and stagger angle. Qatu et al. [39] applied the laminated shell formulation to obtain the mode shapes of laminated composite twisted blades. Hu et al. [40] performed the vibration analysis for the conical rotating panels with a twisted angle, and examined a wide range of design parameters. Although their results showed good predictions on the vibration characteristics, their specific shell formulations were limited to thin and

shallow structures.

Degenerated Shell Elements

There are various shell elements whose formulations were derived from the degeneration concept. The core of this concept is the discretization of a three-dimensional mathematical model with three-dimensional elements and their subsequent reduction into two-dimensional elements. The degenerated shell elements are built from a continuum based approach. In comparison the continuum based approach to shell theory, it is not necessary to develop the complete formulation. The degeneration of this three-dimensional shell element is done by eliminating the nodes into a single node located at the mid-surface of the element, as shown in Fig. 2. The procedure of creating a shell element using the degenerated solid approach is to eliminate nodes by enforcing different constraints on the behavior of the element. First, nodes on the mid-surface are removed corresponding to assuming constant transverse strains. Then, opposite nodes are linked by assuming equal displacements and assigning two rotational DOFs to each pair of nodes. Finally, the motion of each straight line is described by five DOFs in one node.

Ahmad et al. [41] introduced the continuum-based degenerated shell element. They treated the shells of arbitrarily shapes without complicated assumptions for specific shell theories. Due to the simplicity of this concept in the formulation, many results have been obtained and used to

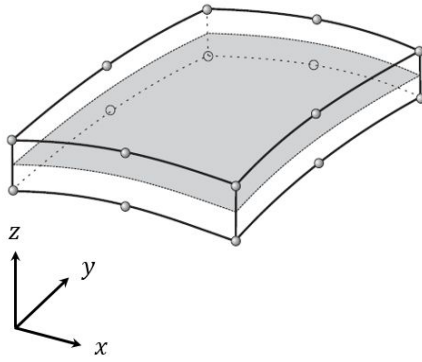
improve performance of the degenerated shell element. The geometric and material non-linear analysis of shells was extended by Ramm [42] and Bathe et al [43]. Lee et al. [44] and Kee et al. [45] performed the vibration analysis of rotating pretwisted plates and shells with small rotation and displacement assumptions. Comprehensive overviews of the degenerated shell approach can be found in Crisfield [46] and Hughes [47].

One important problem associated with the degenerated shell element was that its basic formulation only requires rotational degrees of freedom that would bend the blade. If the target structure has a single smooth surface, three translational and two rotational degrees of freedom, five in total, would be required. However, such smooth geometry is not generally the case and all three rotations should be included. The third rotational degree of freedom would be the in-plane rotation about the normal to the plane, and it is often called the ‘drilling’ rotational degree of freedom. The precise formulation of the fictitious drilling stiffness is not important in the case of linear problems. However, it would become significant for non-linear problems.

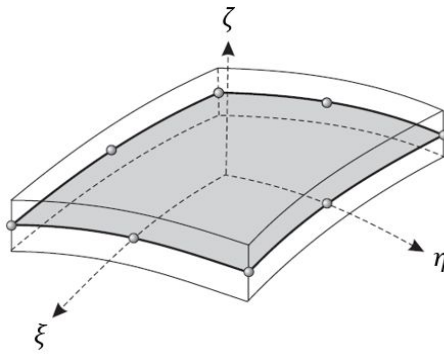
Solid-Shell Elements

Solid-shell elements form a class of finite element models intermediate between thin shell and conventional solid elements. They have the same node and freedom configuration as the solid elements but account for shell-like behavior in the thickness direction. Moreover, the solid-shell

element usually has no difficulties related to drilling degree of freedom, and it is useful for modeling shell-like portions of a three-dimensional structure without the need to connect solid element nodes to shell nodes. Ausserer and Lee [48] developed a three-dimensional solid-shell element for analysis of thin shell structures. They suggested a new mixed formulation for finite element modeling, and proposed a modified stress-strain relation to avoid the transverse shear locking problems. The solid-shell elements are well applicable for both geometrically linear and nonlinear problems. Kim and Lee [49], Hauptmann and Schweizerhof [50], Sze and Zheng [51] and Klinel [52] extended the solid-shell element to model geometrically nonlinear laminated shells. Vu-Quoc and Tan [53] presented a solid-shell element based on the mixed Hu-Washizu variational principle for dynamic analysis of multi-layer composites. Recently, Rah et al. [54] presented a partial hybrid stress solid-shell element that provides accurate interlaminar stress results for laminated composites.



(a) Solid-shell element



(b) Degenerated shell element

Fig. 2 Degeneration process of shell structure to solid-shell and degenerated shell elements

1.3 Objectives and Layout of Thesis

The present thesis has a number of objectives which are listed as follows:

- a) Develop an analysis model capable of simulating the structural dynamic behavior of rotating composite blades. The important features of this analysis model include:
 - A three-dimensional solid-shell element formulation that is applicable to beam, plate and shell type structures with a three-dimensional material law.
 - Computational efficiency so that the analysis may reduce the computational complexity of the problem.
 - Reliable finite element models including elastic couplings and rotational effects.
- b) Investigate the effect of geometric nonlinearity upon the dynamic characteristics of rotating blades with various blade curvatures and initial twists.
- c) Conduct detailed studies on the dynamic characteristics of composite rotor blades with straight and swept tips to determine the combined effect of sweep angle, aspect ratio and composite ply orientation.

- d) Assess the availability of the three-dimensional finite element for structural dynamics modeling of advanced configurations of rotorcraft blades which have the tip sweep and anhedral.

In addition, the overviews of each chapter are as follows.

In Chapter 2, the concept and formulation procedures of geometric nonlinear continuum mechanics are presented. The incremental total-Lagrangian approach is adopted to allow precise estimation on arbitrarily large rotations and displacements. To overcome the shear locking problem, a modified stress-strain relation is adopted.

In Chapter 3, in order to analyze the structures undergoing large displacements and rotations, an eighteen-node solid-shell finite element and the Newton-Raphson method is adopted. The equations of motion for the rotating blades are derived via Hamilton's principle, and the displacement based finite element procedure are employed. To reduce the computational cost, the Guyan and IRS(Improved Reduction System) reduction methods are adopted.

In Chapter 4, numerical results by the present method are compared regarding the several static and dynamic benchmark problems to validate the accuracy and reliability of the present finite element formulations

and solution procedures.

In Chapter 5, the vibration analysis of shell type blades is performed. The blade is modeled as an open cylindrical shell undergoing centrifugal tension force. The influences of geometric nonlinearity and the design parameters, namely blade curvatures and pretwist are investigated.

In Chapter 6, the vibration analysis of beam type blades is performed. The present analysis results using the three-dimensional solid-shell element are compared with the one-dimensional nonlinear beam analysis results to assess the availability of the present element for structural dynamics modeling of advanced configuration of rotorcraft blades. The effect of the tip sweep and anhedral, aspect ratio and composite ply orientation are investigated.

In Chapter 7, a summary, conclusions and future works of the present thesis are included.

Chapter 2. Geometrically Nonlinear Formulation

2.1 Introduction

Based on the assumptions that certain quantities in formulation are relatively small, the problem may be reduced to a linearized one. Linear solutions may be obtained with considerable ease and less computational cost when compared to nonlinear solutions. In many instances, assumptions of linearity lead to reasonable idealization of the behavior of the system. However, in some cases assumption of linearity may result in an unrealistic approximation of the response. The type of analysis, either linear or nonlinear, depends on the goal of the analysis and inaccuracies in the system response that may be tolerated. In some cases, nonlinear analysis is the only option left for the analyst as well as the designer. There are two common sources of nonlinearity: geometric and material nonlinearity. The geometric nonlinearity arises purely from geometric consideration (e.g. nonlinear strain-displacement relations), and the material nonlinearity is due to nonlinear constitutive behavior of the material of the system. In addition, the third type of nonlinearity may arise due to changing initial or boundary conditions. Since the material is assumed to be linear elastic, the scope of the present thesis focuses on the geometrically nonlinear problems.

In the case of large displacements there may be significant changes

in the configuration. Therefore, one should be careful in defining the reference configuration with respect to which different quantities are measured. A practical way of determining the final configuration from a known initial configuration C_0 is to assume that the total load is applied in increments so that the body may occupy several intermediate configurations, C_i ($i = 1, 2, 3, \dots$), prior to occupying the final configuration. In the determination of an intermediate configuration C_i , the Lagrangian description of motion can use any of the previously known configurations C_0, C_1, \dots, C_{i-1} as the reference configuration C_R . If the initial configuration is used as the reference configuration with respect to which all quantities are measured, it is called the total Lagrangian description. Also, if the latest known configuration C_{i-1} is used as the reference configuration, it is called the updated Lagrangian description. In the present thesis, the total Lagrangian approach was adopted, and three equilibrium configurations of the body were considered, namely, C_0, C_1 , and C_2 , which correspond to three different loads. As shown in Fig. 3, the three equilibrium configurations of the body can be regarded as the initial undeformed configuration C_0 , the last known deformed configuration C_1 , and the current deformed configuration C_2 to be determined.

In the formulation of geometric nonlinear continuum mechanics, the following notation is adopted: a left superscript on a quantity denotes the configuration in which the quantity occurs, and a left subscript denotes the configuration with respect to which the quantity is measured. Thus,

${}^i_j Q$ indicates that the quantity Q occurs in the configuration C_i but measured in the configuration C_j . Also, when the quantity under consideration is measured in the same configuration in which it occurs, the left subscript may not be used.

Because of dealing with three different configurations, it is necessary to introduce the following symbols in the three configurations:

Configuration :	C_0	C_1	C_2	
Position vectors :	${}^0\mathbf{x}$	${}^1\mathbf{x}$	${}^2\mathbf{x}$	
Volumes :	0V	1V	2V	
Areas :	0A	1A	2A	(2.1)
Density :	${}^0\rho$	${}^1\rho$	${}^2\rho$	
Total displacement of a point :		${}^1_0\mathbf{u}$	${}^2_0\mathbf{u}$	

The total displacements of the particle P in the two configurations C_1 and C_2 can be written as

$${}^1_0\mathbf{u} = {}^1\mathbf{x} - {}^0\mathbf{x} \quad (2.2)$$

$${}^2_0\mathbf{u} = {}^2\mathbf{x} - {}^0\mathbf{x} \quad (2.3)$$

and the displacement increment of the point from C_1 to C_2 is

$$\mathbf{u} = {}^2_0\mathbf{u} - {}^1_0\mathbf{u} \quad (2.4)$$

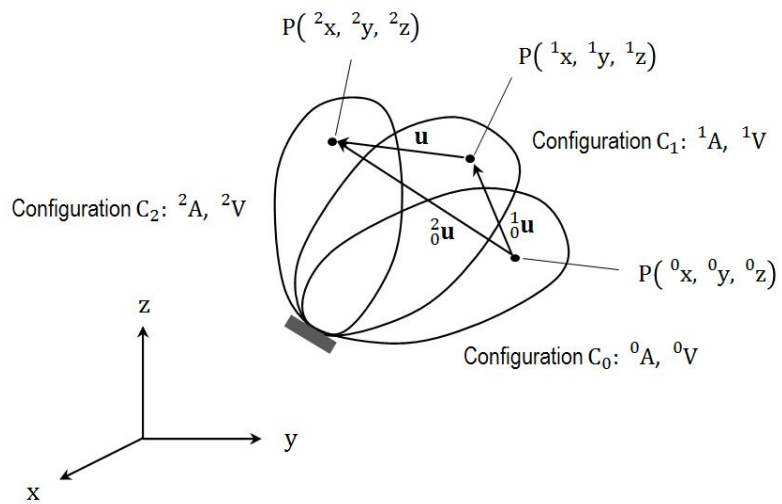


Fig. 3 Initial and deformed configurations of a solid body

2.2 Strain and Stress Tensors

In the present thesis, the total-Lagrangian description of the motion of solid bodies undergoing geometric changes was adopted. Thus, it is necessary to use the Green-Lagrange strains and the 2nd Piola-Kirchhoff (PK2) stresses. The Cartesian components of the Green-Lagrange strain tensors in the two configurations C_1 and C_2 are defined by

$${}^1_0\varepsilon_{ij} = \frac{1}{2} \left({}^1_0u_{i,0x_j} + {}^1_0u_{j,0x_i} + {}^1_0u_{k,0x_i} {}^1_0u_{k,0x_j} \right) \quad (2.5)$$

$${}^2_0\varepsilon_{ij} = \frac{1}{2} \left({}^2_0u_{i,0x_j} + {}^2_0u_{j,0x_i} + {}^2_0u_{k,0x_i} {}^2_0u_{k,0x_j} \right) \quad (2.6)$$

where $({}^0x_i, {}^0x_j, {}^0x_k)$ and (u_i, u_j, u_k) denote the undeformed coordinates and the components of displacement vector respectively.

It is useful to define an incremental strain component ${}_0\varepsilon_{ij}$, and it denotes the strains induced in the movement from the configuration C_1 to the configuration C_2 . The incremental Green-Lagrange strain tensors are defined as follows.

$$\begin{aligned} {}_0\varepsilon_{ij} d^0x_i d^0x_j &= \frac{1}{2} \left[({}^2ds)^2 - ({}^1ds)^2 \right] \\ &= ({}^2_0\varepsilon_{ij} - {}^1_0\varepsilon_{ij}) d^0x_i d^0x_j \\ &= ({}_0e_{ij} + {}_0\eta_{ij}) d^0x_i d^0x_j \end{aligned} \quad (2.7)$$

where ${}^0e_{ij}$ and ${}^0\eta_{ij}$ denote the linear and nonlinear components of the incremental Green-Lagrange strain tensor, respectively as

$${}^0e_{ij} = \frac{1}{2} \left(u_{i, {}^0x_j} + u_{j, {}^0x_i} + \delta u_{k, {}^0x_i} u_{k, {}^0x_j} + u_{k, {}^0x_i} \delta u_{k, {}^0x_j} \right) \quad (2.8)$$

$${}^0\eta_{ij} = \frac{1}{2} u_{k, {}^0x_i} u_{k, {}^0x_j} \quad (2.9)$$

The PK2 stress tensor components in the C_1 and C_2 configurations are defined by ${}^1_0S_{ij}$ and ${}^2_0S_{ij}$, and the relation of stress components in the two configurations can be written as

$${}^2_0S_{ij} = {}^1_0S_{ij} + {}^0S_{ij} \quad (2.10)$$

where ${}^0S_{ij}$ are the components of the Kirchhoff stress increment tensor. Since the PK2 stresses are convenient mathematical quantities, Cauchy stresses are the only true stresses in the current configuration. Thus, the Cauchy stress tensor components ${}^2\sigma_{ij}$ and ${}^1\sigma_{ij}$ with respect to the configuration C_1 and C_2 can be evaluated by the following relations.

$${}^2\sigma_{ij} = \frac{{}^2\rho}{{}^0\rho} \frac{\partial {}^2x_i}{\partial {}^0x_p} \frac{\partial {}^2x_j}{\partial {}^0x_q} {}^2_0S_{pq} \quad (2.11)$$

$${}^1\sigma_{ij} = \frac{{}^1\rho}{{}^0\rho} \frac{\partial {}^1x_i}{\partial {}^0x_p} \frac{\partial {}^1x_j}{\partial {}^0x_q} {}^1_0S_{pq} \quad (2.12)$$

where ${}^0\rho$, ${}^1\rho$ and ${}^2\rho$ denote the mass densities of the material in each configuration. In the present thesis, the identical densities, ${}^0\rho = {}^1\rho = {}^2\rho = \rho$, are employed.

2.3 Strain Energy

The strain energy U for an elastic structure is given by

$$U = \frac{1}{2} \int_{{}^0V} {}^2S_{ij} {}^2\varepsilon_{ij} d {}^0V \quad (2.13)$$

where ${}^2S_{ij}$ denotes the Cartesian components of the PK2 stress tensor corresponding to the configuration C_2 but measured in the configuration C_0 . Also, ${}^2\varepsilon_{ij}$ denotes the Cartesian components of the Green-Lagrange strain tensor in the configuration C_2 but measured in the configuration C_0 . Since the stresses ${}^2S_{ij}$ and strains ${}^2\varepsilon_{ij}$ are unknown, the following incremental decompositions are used.

$${}^2S_{ij} = {}^1S_{ij} + {}_0S_{ij} \quad (2.14)$$

$${}^2\varepsilon_{ij} = {}^1\varepsilon_{ij} + {}_0\varepsilon_{ij} \quad (2.15)$$

where ${}^1S_{ij}$ and ${}^1\varepsilon_{ij}$ are known quantities of the PK2 stresses and Green-Lagrange strains in the configuration C_1 , and ${}_0S_{ij}$ and ${}_0\varepsilon_{ij}$ are unknown increments.

In the derivation of finite element models of incremental nonlinear analysis of solid continua, it is necessary to specify the stress-strain relations in incremental form, and the constitutive equations must describe relationship between compatible pairs of stresses and strains. In the total Lagrangian formulation, the constitutive relations can be expressed in terms of the Kirchhoff stress increment tensor components ${}_0S_{ij}$ and Green-Lagrange strain increment tensor components ${}_0\varepsilon_{ij}$ as

$${}_0S_{ij} = {}_0Q_{ijrs} {}_0\varepsilon_{rs} \quad (2.16)$$

where ${}_0Q_{ijrs}$ denotes the incremental constitutive tensors with respect to the configuration C_0 .

2.4 Kinetic Energy

The kinetic energy T for a rotating blade can be expressed by

$$T = \frac{1}{2} \int_{{}_0V} \rho \mathbf{v} \cdot \mathbf{v} d {}_0V \quad (2.17)$$

where ρ is the mass density of the blade, and \mathbf{v} is the velocity vector of an arbitrary point of the blade with respect to an inertial coordinate system.

As shown in Fig. 4, the position vector \mathbf{r} from the origin of the inertial

coordinate system to a point in the deformed blade can be written as

$$\mathbf{r} = (h_i \quad h_j \quad h_k) \begin{Bmatrix} \mathbf{e}_i \\ \mathbf{e}_j \\ \mathbf{e}_k \end{Bmatrix} + (x + u \quad y + v \quad z + w) \begin{Bmatrix} \mathbf{e}_x \\ \mathbf{e}_y \\ \mathbf{e}_z \end{Bmatrix} \quad (2.18)$$

where (h_i, h_j, h_k) are the translational offsets of the global (or blade) coordinate system (x, y, z) evaluated from the inertial coordinate (i, j, k) . Also, $(\mathbf{e}_i, \mathbf{e}_j, \mathbf{e}_k)$ and $(\mathbf{e}_x, \mathbf{e}_y, \mathbf{e}_z)$ are the base vectors in an inertial and global coordinates, respectively. The position vector is obtained in the global coordinate system using the transformation matrices \mathbf{T}_{β_i} , \mathbf{T}_{β_j} and \mathbf{T}_{β_k} , corresponding to the Euler angles β_i , β_j and β_k about the inertial axes.

$$\mathbf{r} = (h_x + x + u)\mathbf{e}_x + (h_y + y + v)\mathbf{e}_y + (h_z + z + w)\mathbf{e}_z \quad (2.19)$$

$$\begin{Bmatrix} \mathbf{e}_x \\ \mathbf{e}_y \\ \mathbf{e}_z \end{Bmatrix} = \mathbf{T}_{\beta_k} \mathbf{T}_{\beta_j} \mathbf{T}_{\beta_i} \begin{Bmatrix} \mathbf{e}_i \\ \mathbf{e}_j \\ \mathbf{e}_k \end{Bmatrix} = \mathbf{T}_{\Omega} \begin{Bmatrix} \mathbf{e}_i \\ \mathbf{e}_j \\ \mathbf{e}_k \end{Bmatrix} \quad (2.20)$$

$$\begin{Bmatrix} h_x \\ h_y \\ h_z \end{Bmatrix} = \mathbf{T}_{\beta_k} \mathbf{T}_{\beta_j} \mathbf{T}_{\beta_i} \begin{Bmatrix} h_i \\ h_j \\ h_k \end{Bmatrix} = \mathbf{T}_{\Omega} \begin{Bmatrix} h_i \\ h_j \\ h_k \end{Bmatrix}$$

$$\mathbf{T}_{\Omega} = \mathbf{T}_{\beta_k} \mathbf{T}_{\beta_j} \mathbf{T}_{\beta_i}$$

$$= \begin{bmatrix} \cos \beta_k & \sin \beta_k & 0 \\ -\sin \beta_k & \cos \beta_k & 0 \\ 0 & 0 & 1 \end{bmatrix} \begin{bmatrix} \cos \beta_j & 0 & -\sin \beta_j \\ 0 & 1 & 0 \\ \sin \beta_j & 0 & \cos \beta_j \end{bmatrix} \quad (2.21)$$

$$\begin{bmatrix} 1 & 0 & 0 \\ 0 & \cos \beta_i & \sin \beta_i \\ 0 & -\sin \beta_i & \cos \beta_i \end{bmatrix}$$

The velocity vector of an arbitrary point on the blade with respect to the inertial reference coordinate can be written as

$$\mathbf{v} = \frac{d\mathbf{r}}{dt} + \boldsymbol{\Omega} \mathbf{e}_k \times \mathbf{r}$$

$$= \begin{pmatrix} \dot{u} + \Omega_y(h_z + z + w) - \Omega_z(h_y + y + v) \\ \dot{v} + \Omega_z(h_x + x + u) - \Omega_x(h_z + z + w) \\ \dot{w} + \Omega_x(h_y + y + v) - \Omega_y(h_x + x + u) \end{pmatrix}^T \begin{Bmatrix} \mathbf{e}_x \\ \mathbf{e}_y \\ \mathbf{e}_z \end{Bmatrix} \quad (2.22)$$

where the transformed angular velocity (Ω_x , Ω_y , Ω_z) is given by

$$\{\Omega_x \quad \Omega_y \quad \Omega_z\}^T = \mathbf{T}_\Omega \{0 \quad 0 \quad \Omega\}^T \quad (2.23)$$

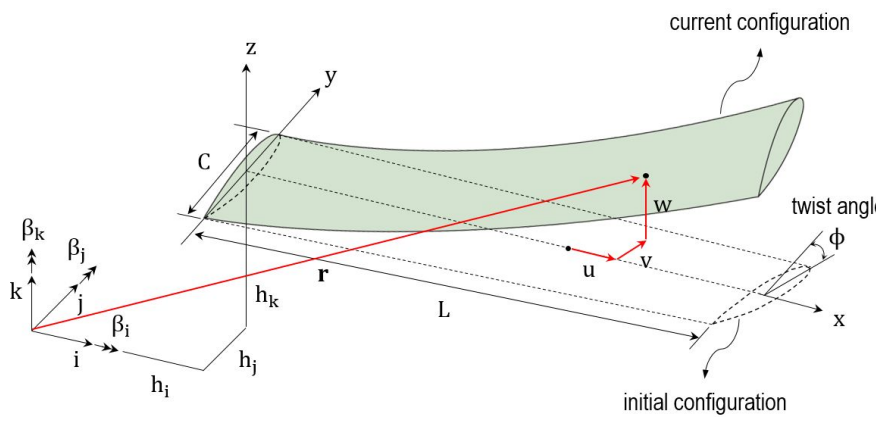


Fig. 4 Configuration of a rotating twisted blade

2.5 Equations of Motion

The equations of motion for the rotating blade were derived via Hamilton's principle where the variation in the time integral of the Lagrangian function is set to be zero. A general form of Hamilton's principle can be written as

$$\delta\Pi = \int_{t_1}^{t_2} (\delta U - \delta T - \delta W_E) dt = 0 \quad (2.24)$$

where T is the kinetic energy while considering the rotating effect; U is the strain energy, which is expressed as in Eq. (2.13); and W_e is the work done by external forces.

From Eqs. (2.14) through (2.16), the variational form of strain energy, δU , can be written as

$$\begin{aligned} \delta U &= \frac{1}{2} \delta \left[\int_{0V} {}^2S_{ij} {}^2\varepsilon_{ij} d^0V \right] \\ &= \frac{1}{2} \delta \left[\int_{0V} ({}^1S_{ij} + Q_{ijrs} {}^0\varepsilon_{rs}) ({}^1\varepsilon_{ij} + {}^0\varepsilon_{ij}) d^0V \right] \\ &= \int_{0V} Q_{ijrs} {}^0\varepsilon_{rs} \delta {}^0\varepsilon_{ij} d^0V + \int_{0V} {}^1S_{ij} \delta {}^0\varepsilon_{ij} d^0V \end{aligned} \quad (2.25)$$

The solution of Eq. (2.25) cannot be obtained directly, since it is nonlinear in terms of the displacement. An approximate solution can be

obtained by assuming that ${}_0\varepsilon_{ij} \cong {}_0e_{ij}$. Thus, in the total Lagrangian formulation the linearized approximate equation can be obtained as

$$\begin{aligned} \delta U = & \int_{{}^0V} Q_{ijrs} {}_0e_{rs} \delta {}_0e_{ij} d {}^0V + \int_{{}^0V} {}^1S_{ij} \delta {}_0e_{ij} d {}^0V \\ & + \int_{{}^0V} {}^1S_{ij} \delta {}_0\eta_{ij} d {}^0V \end{aligned} \quad (2.26)$$

Using Eqs. (2.19) through (2.23), a variational form of the kinetic energy, δT , can be written as

$$\delta T = \frac{1}{2} \int_{{}^0V} \rho [(\dot{u})^2 + (\dot{v})^2 + (\dot{w})^2] d {}^0V \quad (2.27)$$

$$= \int_{{}^0V} \rho (D_u \delta u + D_v \delta v + D_w \delta w) d {}^0V$$

$$\begin{aligned} D_u = & -\ddot{u} + 2\Omega_z \dot{v} - 2\Omega_y \dot{w} + (\Omega_y^2 + \Omega_z^2)(h_x + x + u) \\ & - \Omega_y \Omega_x (h_y + y + v) - \Omega_z \Omega_x (h_z + z + w) \end{aligned}$$

$$\begin{aligned} D_v = & -\ddot{v} + 2\Omega_x \dot{w} - 2\Omega_z \dot{u} - \Omega_x \Omega_y (h_x + x + u) \\ & + (\Omega_z^2 + \Omega_x^2)(h_y + y + v) - \Omega_z \Omega_y (h_z + z + w) \end{aligned} \quad (2.28)$$

$$\begin{aligned} D_w = & -\ddot{w} + 2\Omega_y \dot{u} - 2\Omega_x \dot{v} - \Omega_x \Omega_z (h_x + x + u) \\ & - \Omega_y \Omega_z (h_y + y + v) + (\Omega_x^2 + \Omega_y^2)(h_z + z + w) \end{aligned}$$

The variational form of the work done by the surface, body and external force can be written as

$$\delta W_e = \int_{^0A} {}^2_0t_k \delta u_k d^0A + \int_{^0V} {}^2_0f_k \delta u_k d^0V + {}^2_0R_k \delta u_k \quad (2.29)$$

From Eqs. (2.25) through (2.29), the final form of equations of motion can be written as

$$\begin{aligned} & \int_{^0V} Q_{ijrs} {}_0e_{rs} \delta {}_0e_{ij} d^0V + \int_{^0V} {}^1_0S_{ij} \delta {}_0\eta_{ij} d^0V \\ & \quad - \int_{^0V} \rho (D_u \delta u + D_v \delta v + D_w \delta w) d^0V \\ & = \int_{^0A} {}^2_0t_k \delta u_k d^0A + \int_{^0V} {}^2_0f_k \delta u_k d^0V + {}^2_0R_k \delta u_k \\ & \quad - \int_{^0V} {}^1_0S_{ij} \delta {}_0e_{ij} d^0V \end{aligned} \quad (2.30)$$

2.6 Composite Structures

Composites are made of two or more materials, combined together to obtain a new compound with properties that are superior to those of individual components. Generally among the main constituents of a composite material one can recognize: reinforcement components, matrix and fillers. The reinforcement mostly takes the form of fibers or whiskers that are used to provide the required strength and stiffness. The matrix provides a compliant support for the reinforcement; it contributes to load transfer and also gives environmental protection. Fillers are other

substances that are added to the matrix to reduce the cost but sometimes to improve other mechanical properties of the composite. It is quite obvious that mechanical properties of composites depend mainly on the choice of material components used for the composite but they are also considerably influenced by the applied fabrication technique. The most suitable for structural applications among all composite materials there are fiber reinforced composites, with the reinforcement taking the form of either continuous (long) fibers or whiskers (short fibers). Composites reinforced with continuous fibers frequently appear as fiber reinforced composite laminates. As shown in Fig. 5, a typical fiber reinforced composite laminate is made of a number of unidirectional fiber reinforced composite layers. A composite layer with a parallel system of reinforcement fibers represents an orthotropic medium with three mutually orthogonal plane of symmetry. Usually a composite layer consists of high modulus fibers (typically those are glass, boron or graphite fibers) embedded in a matrix (epoxy or polyamide). A resulting fiber-reinforced material combines a high strength with a light weight.

The principal material directions are used in connection with the orthotropic materials since the constitutive properties of the composite materials are conveniently described with this coordinate. As shown in Fig. 6, the principal material directions are denoted by 1 and 2. Direction 1 is aligned with the fibers, direction 2 is perpendicular to 1 direction, and direction 3 is coincident with the z' axis in the local coordinate system. In order to avoid the locking problem, the stress-strain relation

can be modified to incorporate a thin plate and shell behavior by neglecting the effect of σ_{zz} on ε_{xx} and ε_{yy} [49] such that

$$\begin{Bmatrix} \bar{\varepsilon}_1 \\ \bar{\varepsilon}_2 \\ \bar{\varepsilon}_3 \\ \bar{\varepsilon}_4 \\ \bar{\varepsilon}_5 \\ \bar{\varepsilon}_6 \end{Bmatrix} = \begin{bmatrix} \bar{P}_{11} & \bar{P}_{12} & 0 & 0 & 0 & 0 \\ \bar{P}_{12} & \bar{P}_{22} & 0 & 0 & 0 & 0 \\ 0 & 0 & \bar{P}_{33} & 0 & 0 & 0 \\ 0 & 0 & 0 & \bar{P}_{44} & 0 & 0 \\ 0 & 0 & 0 & 0 & \bar{P}_{55} & 0 \\ 0 & 0 & 0 & 0 & 0 & \bar{P}_{66} \end{bmatrix} \begin{Bmatrix} \bar{\sigma}_1 \\ \bar{\sigma}_2 \\ \bar{\sigma}_3 \\ \bar{\sigma}_4 \\ \bar{\sigma}_5 \\ \bar{\sigma}_6 \end{Bmatrix} \quad (2.31)$$

where \bar{P}_{ij} denotes the compliance coefficients in the principal material directions. The modified elastic material properties matrix $\bar{\mathbf{Q}}$ can be determined by inverting the relationship in Eq. (2.31).

It is necessary to note that, under the off-axis situation, the transformation from (1, 2, 3) to (x', y', z') is performed by a rotation of angle θ . Then the stiffness matrix can be rewritten as $\mathbf{Q}' = \mathbf{T}_L^T \bar{\mathbf{Q}} \mathbf{T}_L$, and \mathbf{T}_L is the transformation matrix between local and material axes. The relation in the stiffness matrices between Q_{ij} in the global coordinate system (x, y, z) and Q'_{ij} in the local coordinate system can be written in a matrix form as $\mathbf{Q} = \mathbf{T}_G^T \mathbf{Q}' \mathbf{T}_G$. Here, \mathbf{T}_G is the transformation matrix between the global and local axes. The transformations between the different coordinate systems are provided through transformation matrices as shown in Fig. 7. Details of the compliance matrix $\bar{\mathbf{P}}$ and transformation matrices \mathbf{T}_L and \mathbf{T}_G are given in Appendix A.

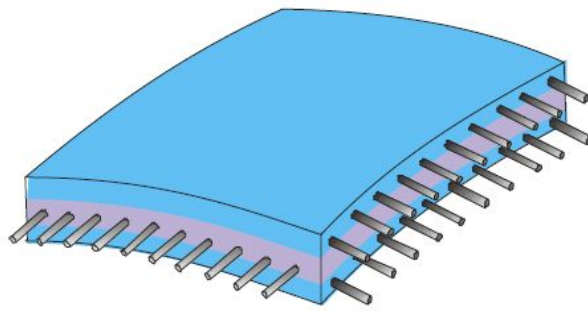


Fig. 5 An example of fiber reinforced composites

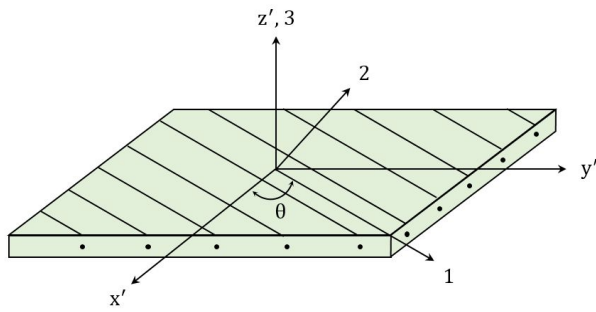
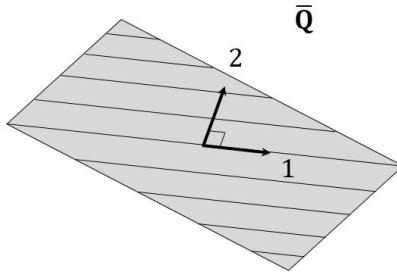
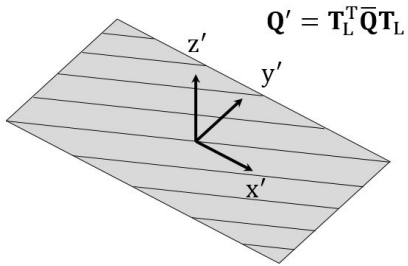


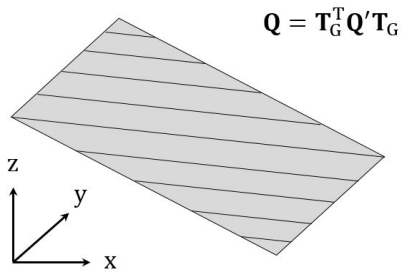
Fig. 6 Material directions of a laminated layer and the local coordinate system



(a) Principal material coordinate



(b) Local coordinate



(c) Global coordinate

Fig. 7 Transformation of material properties between global, local and principal material coordinate system

Chapter 3. Finite Element Formulation

The present solid-shell elements can be categorized as one of the finite element models, which are applicable to shell analyses. They are different from the degenerated shell elements in the sense that the degenerated elements are equipped with both translational and rotational DOFs. There are several advantages of the solid-shell elements compared to the degenerated shell elements as follows:

- The solid-shell elements are simpler in their kinematic and geometric descriptions.
- No special effort is required for matching the translational and rotational DOFs when a structure consists of both solid and thin-walled regions. The laborious task of defining algebraic constraints or introducing solid-to-shell transition elements can be exempted.
- The complication on handling finite rotational increments can be avoided.

In the present thesis, the solid-shell element has nine nodes on the top surface, nine on the bottom and no mid-thickness nodes, giving an 18-node element. Each node has only translational degrees of freedom; thus, no rotational freedoms can be explicitly defined, and there is no difficulties related to drilling rotational degree of freedom.

3.1 Coordinate Systems

The geometry and kinematics of the present solid-shell element can be described by using different coordinate systems. In general, standard solid elements use only natural coordinate system and global coordinate system. In the present thesis, a set of local orthogonal coordinate systems are added and set up at the center of each element. Thus, the present solid-shell element shown in Fig. 8 can be described by the relation between global, local and natural coordinates using the geometry of structure.

3.1.1 Global Coordinate System

The global coordinate system, denoted by (x,y,z) , can be freely chosen in relation to the geometry of the structure defined in the three-dimensional space. The nodal coordinates, displacements as well as the global mass matrix, damping matrix, stiffness matrices, and the applied external forcing vectors are expressed in terms of this coordinate system.

3.1.2 Local Coordinate System

The direction cosines of the local axes (x',y',z') with respect to the global axes (x,y,z) can be defined using the base vectors $(\mathbf{a}_1, \mathbf{a}_2, \mathbf{a}_3)$, which are parallel to the axes of the local coordinate as follows:

$$\begin{aligned}
\mathbf{a}_3 &= \mathbf{g}_1 \times \mathbf{g}_2 / \|\mathbf{g}_1 \times \mathbf{g}_2\| \\
\mathbf{a}_2 &= \mathbf{a}_3 \times \mathbf{g}_1 / \|\mathbf{a}_3 \times \mathbf{g}_1\| \\
\mathbf{a}_1 &= \mathbf{a}_2 \times \mathbf{a}_3 / \|\mathbf{a}_2 \times \mathbf{a}_3\|
\end{aligned} \tag{3.1}$$

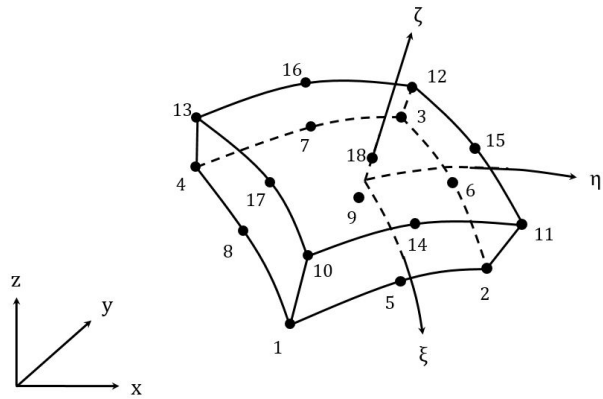
where \mathbf{g}_1 and \mathbf{g}_2 are the covariant base vectors at the centroid of element ($\xi=\eta=\zeta=0$) which define the tangential directions along the ξ and η axes, respectively.

$$\begin{aligned}
\mathbf{g}_1 &= \{\partial x / \partial \xi \quad \partial y / \partial \xi \quad \partial z / \partial \xi\}^T \\
\mathbf{g}_2 &= \{\partial x / \partial \eta \quad \partial y / \partial \eta \quad \partial z / \partial \eta\}^T
\end{aligned} \tag{3.2}$$

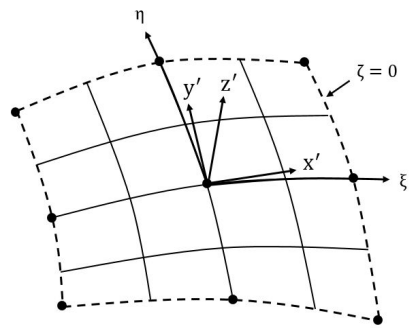
For the transformation laws of Cartesian coordinate systems, the position vector \mathbf{x} and the displacement vector \mathbf{u} in global coordinate system can be transformed into the position \mathbf{x}' and displacement \mathbf{u}' vectors in the local coordinate system by the following relation:

$$\begin{aligned}
\mathbf{x}' &= \mathbf{T}^T \mathbf{x} \\
\mathbf{u}' &= \mathbf{T}^T \mathbf{u} \\
\mathbf{T} &= [\mathbf{a}_1 \quad \mathbf{a}_2 \quad \mathbf{a}_3]
\end{aligned} \tag{3.3}$$

where \mathbf{T} is the transformation matrix between the local and the global coordinates.



(a) Global and natural coordinate systems



(b) Local and natural coordinate systems

Fig. 8 Configurations and coordinates of the 18-node solid-shell element

3.1.3 Natural Coordinate System

The shape functions, N_k , are expressed in terms of the curvilinear coordinate system called the natural coordinate. This coordinate system is denoted by ξ , η and ζ . The ζ direction is approximately normal to the top and bottom surfaces, and it varies from -1 to +1 in the thickness direction. The origin of the natural coordinate system is set to the center of each element. In general, this coordinate system is not always orthogonal for arbitrary element shapes.

3.2 Element Geometry and Displacement Field

The global coordinates and displacements of an arbitrary point in the element at configuration C_1 can be interpolated by the element shape functions, and those are written as

$${}^1\mathbf{x}(\xi, \eta, \zeta) = \sum_{k=1}^9 N_k(\xi, \eta) (\zeta^- {}^1\mathbf{x}_k + \zeta^+ {}^1\mathbf{x}_{9+k}) \quad (3.4)$$

$${}^1\mathbf{u}(\xi, \eta, \zeta) = \sum_{k=1}^9 N_k(\xi, \eta) (\zeta^- {}^1\mathbf{u}_k + \zeta^+ {}^1\mathbf{u}_{9+k}) \quad (3.5)$$

where ${}^1\mathbf{x}_k$ and ${}^1\mathbf{u}_k$ denote the nodal coordinates and displacements, and $\zeta^- = (1 - \zeta)/2$ and $\zeta^+ = (1 + \zeta)/2$. Moreover, the expressions for the shape functions N_k with natural coordinates ξ and η are given as

$$\begin{aligned}
N_1 &= \frac{1}{4}(\xi^2 - \xi)(\eta^2 - \eta) \\
N_2 &= \frac{1}{4}(\xi^2 + \xi)(\eta^2 - \eta) \\
N_3 &= \frac{1}{4}(\xi^2 + \xi)(\eta^2 + \eta) \\
N_4 &= \frac{1}{4}(\xi^2 - \xi)(\eta^2 + \eta) \\
N_5 &= \frac{1}{2}(1 - \xi^2)(\eta^2 - \eta) \\
N_6 &= \frac{1}{2}(\xi^2 + \xi)(1 - \eta^2) \\
N_7 &= \frac{1}{2}(1 - \xi^2)(\eta^2 + \eta) \\
N_8 &= \frac{1}{2}(\xi^2 - \xi)(1 - \eta^2) \\
N_9 &= (1 - \xi^2)(1 - \eta^2)
\end{aligned} \tag{3.6}$$

3.3 Strain-Displacement Relation

Using Eqs. (2.8) and (2.9), the variational form of incremental Green-Lagrange strain components can be written as

$$\begin{aligned}
\delta {}_0\varepsilon_{ij} &= \delta {}_0e_{ij} + \delta {}_0\eta_{ij} \\
&= \frac{1}{2} \left(\delta u_{i, {}_0x_j} + \delta u_{j, {}_0x_i} + {}^1u_{k, {}_0x_i} \delta u_{k, {}_0x_j} + \delta u_{k, {}_0x_i} {}^1u_{k, {}_0x_j} \right) \\
&\quad + \frac{1}{2} \left(u_{k, {}_0x_i} \delta u_{k, {}_0x_j} + \delta u_{k, {}_0x_i} u_{k, {}_0x_j} \right)
\end{aligned} \tag{3.7}$$

The linear and nonlinear incremental Green-Lagrange strain components given in Eq. (3.7) are interpolated by the shape functions, and they can be written in a vector and matrix form as follows.

$$\delta {}_0\mathbf{e} = [\mathbf{L} + \mathbf{A}_e]\delta\mathbf{H} \quad (3.8)$$

$$\delta {}_0\boldsymbol{\eta} = \mathbf{A}_\eta\delta\mathbf{H} \quad (3.9)$$

Details of the constant matrix \mathbf{L} , and the displacement gradient matrices \mathbf{A}_e and \mathbf{A}_η for the linear and nonlinear Green-Lagrange strain tensors are given in Appendix B. Here, \mathbf{H} denotes unknown displacement gradient vector, and it can be expressed as

$$\mathbf{H} = \begin{Bmatrix} u, {}_0x \\ u, {}_0y \\ u, {}_0z \\ v, {}_0x \\ v, {}_0y \\ v, {}_0z \\ w, {}_0x \\ w, {}_0y \\ w, {}_0z \end{Bmatrix} = \begin{bmatrix} {}_0\mathbf{J}^{-1} & \mathbf{0} & \mathbf{0} \\ \mathbf{0} & {}_0\mathbf{J}^{-1} & \mathbf{0} \\ \mathbf{0} & \mathbf{0} & {}_0\mathbf{J}^{-1} \end{bmatrix} \begin{Bmatrix} u, \xi \\ u, \eta \\ u, \zeta \\ v, \xi \\ v, \eta \\ v, \zeta \\ w, \xi \\ w, \eta \\ w, \zeta \end{Bmatrix} = {}_0\hat{\mathbf{J}}^{-1}\mathbf{P}\mathbf{q} = \mathbf{G}\mathbf{q} \quad (3.10)$$

where the matrix \mathbf{P} contains the derivatives of the shape functions with respect to the natural coordinates, and \mathbf{q} is the nodal vector of each element. Also, details of the matrix \mathbf{P} and the nodal vector \mathbf{q} are given in Appendix B.

The global coordinate derivatives of the displacement can be written as the natural coordinate derivatives using the Jacobian matrix as follows.

$$\begin{bmatrix} u, x & v, x & w, x \\ u, y & v, y & w, y \\ u, z & v, z & w, z \end{bmatrix} = {}_0\mathbf{J}^{-1} \begin{bmatrix} u, \xi & v, \xi & w, \xi \\ u, \eta & v, \eta & w, \eta \\ u, \zeta & v, \zeta & w, \zeta \end{bmatrix} \quad (3.11)$$

where the Jacobian matrix is given by

$${}^0\mathbf{J} = \begin{bmatrix} {}^0x_{,\xi} & {}^0y_{,\xi} & {}^0z_{,\xi} \\ {}^0x_{,\eta} & {}^0y_{,\eta} & {}^0z_{,\eta} \\ {}^0x_{,\zeta} & {}^0y_{,\zeta} & {}^0z_{,\zeta} \end{bmatrix} \quad (3.12)$$

Using Eqs. (3.8) and (3.9), the strain-displacement relation matrix \mathbf{B} now takes the following form.

$$\begin{aligned} \mathbf{B} &= \mathbf{B}_L + \mathbf{B}_{NL} \\ \mathbf{B}_L &= [\mathbf{L} + \mathbf{A}_e]\mathbf{G} \\ \mathbf{B}_{NL} &= \mathbf{A}_\eta\mathbf{G} \end{aligned} \quad (3.13)$$

3.4 Derivation of Matrices and Vectors

Using Eqs. (3.8) through (3.13), the first term in the variational form of the strain energy in Eq. (2.26) becomes

$$\begin{aligned} \int_{{}^0V} Q_{ijrs} {}^0e_{rs} \delta {}^0e_{ij} d {}^0V &= \int_{{}^0V} \delta {}^0e^T \mathbf{Q} {}^0e d {}^0V \\ &= \delta \mathbf{q}^T \int_{{}^0V} \mathbf{B}_L^T \mathbf{Q} \mathbf{B}_L d {}^0V \mathbf{q} \end{aligned} \quad (3.14)$$

$$\mathbf{K}_L = \int_{{}^0V} \mathbf{B}_L^T \mathbf{Q} \mathbf{B}_L d {}^0V \quad (3.15)$$

where \mathbf{K}_L denotes the linear stiffness matrix. In the same manner, the second term in Eq. (2.26) becomes

$$\begin{aligned} \int_{^0V} {}^1S_{ij} \delta {}_0e_{ij} d^0V &= \int_{^0V} \delta {}_0\mathbf{e}^T {}^1\bar{\mathbf{S}} d^0V \\ &= \delta \mathbf{q}^T \int_{^0V} \mathbf{B}_{L0}^T {}^1\bar{\mathbf{S}} d^0V \end{aligned} \quad (3.16)$$

$$\mathbf{R}_I = \int_{^0V} \mathbf{B}_{L0}^T {}^1\bar{\mathbf{S}} d^0V \quad (3.17)$$

where \mathbf{R}_I denotes the internal force vector due to the force unbalance, and the PK2 stress vector ${}^1\bar{\mathbf{S}}$ can be written as

$${}^1\bar{\mathbf{S}} = \{ {}^1S_{xx} \quad {}^1S_{yy} \quad {}^1S_{zz} \quad {}^1S_{xy} \quad {}^1S_{yz} \quad {}^1S_{xz} \}^T \quad (3.18)$$

The third term in the final form of equations of motion in Eq. (2.30) takes the following form.

$$\begin{aligned} \int_{^0V} {}^1S_{ij} \delta {}_0\eta_{ij} d^0V &= \int_{^0V} \delta {}_0\boldsymbol{\eta}^T {}^1\bar{\mathbf{S}} d^0V \\ &= \delta \mathbf{q}^T \int_{^0V} \mathbf{B}_{NL0}^T {}^1\bar{\mathbf{S}} d^0V \\ &= \delta \mathbf{q}^T \int_{^0V} \mathbf{G}^T {}^1\mathbf{S} \mathbf{G} d^0V \mathbf{q} \end{aligned} \quad (3.19)$$

$$\mathbf{K}_{\text{NL}} = \int_{^0V} \mathbf{G}^T {}^1\mathbf{S} \mathbf{G} d^0V \quad (3.20)$$

where \mathbf{K}_{NL} denotes the nonlinear stiffness matrix, and the PK2 stress matrix can be written as

$${}^1\mathbf{S} = \begin{bmatrix} {}^1\hat{\mathbf{S}} & \mathbf{0} & \mathbf{0} \\ \mathbf{0} & {}^1\hat{\mathbf{S}} & \mathbf{0} \\ \mathbf{0} & \mathbf{0} & {}^1\hat{\mathbf{S}} \end{bmatrix}, \quad {}^1\hat{\mathbf{S}} = \begin{bmatrix} {}^1S_{xx} & {}^1S_{xy} & {}^1S_{xz} \\ & {}^1S_{yy} & {}^1S_{yz} \\ \text{sym} & & {}^1S_{zz} \end{bmatrix} \quad (3.21)$$

Using Eqs. (2.18) through (2.23), the variational form of kinetic energy in Eq. (2.27) becomes

$$\begin{aligned} \delta T &= - \int_{^0V} \rho \delta \mathbf{q}^T \mathbf{N}^T \mathbf{N} \ddot{\mathbf{q}} \, ^0V - \int_{^0V} \rho \delta \mathbf{q}^T \mathbf{N}^T \boldsymbol{\Omega}_1 \mathbf{N} \dot{\mathbf{q}} \, ^0V \\ &\quad + \int_{^0V} \rho \delta \mathbf{q}^T \mathbf{N}^T \boldsymbol{\Omega}_2 \mathbf{N} \mathbf{q} \, ^0V + \int_{^0V} \rho \delta \mathbf{q}^T \mathbf{N}^T \boldsymbol{\Omega}_3 \, ^0V \\ &= \delta \mathbf{q}^T [-\mathbf{M} \ddot{\mathbf{q}} - \mathbf{C} \dot{\mathbf{q}} + \mathbf{K}_{\text{CF}} \mathbf{q} + \mathbf{F}_{\text{CF}}] \end{aligned} \quad (3.22)$$

where \mathbf{M} , \mathbf{C} , \mathbf{K}_{CF} and \mathbf{F}_{CF} are the element mass matrix, damping matrix due to Coriolis effect, centrifugal stiffness matrix, and the force vector due to the blade rotation as follows.

$$\mathbf{M} = \int_{^0V} \rho \mathbf{N}^T \mathbf{N} d^0V \quad (3.23)$$

$$\mathbf{C} = \int_{^0V} \rho \mathbf{N}^T \boldsymbol{\Omega}_1 \mathbf{N} d^0V \quad (3.24)$$

$$\mathbf{K}_{CF} = \int_{^0V} \rho \mathbf{N}^T \boldsymbol{\Omega}_2 \mathbf{N} d^0V \quad (3.25)$$

$$\mathbf{F}_{CF} = \int_{^0V} \rho \mathbf{N}^T \boldsymbol{\Omega}_3 d^0V \quad (3.26)$$

Details of the shape function matrix \mathbf{N} , and the angular velocity matrix $\boldsymbol{\Omega}_1$ and $\boldsymbol{\Omega}_2$, and the angular velocity vector $\boldsymbol{\Omega}_3$ are presented in Appendix C.

3.5 Layer-wise Thickness Integration

In order to evaluate element matrices and vectors, Gaussian quadrature was adopted to perform the integration. If the structure is built up from a series of layers of different materials, such that the material properties are expressed as discontinuous function of ζ , an appropriate integration through the thickness has to be carried out. In the present thesis, two point rule integration scheme is adopted for each layer. In this section, an efficient way of performing this integration is introduced namely the ‘explicit layering scheme’.

For layered solid-shell elements, the layer-wise thickness integration was performed by dividing the element into a number of sub-elements. Each sub-element represents a layer, and subsequently layer-wise

numerical integration is enabled by transforming the natural thickness coordinate into natural layer coordinates. In order to employ layer-wise numerical integration through the thickness the natural thickness coordinate ζ needs to be transformed into a layer-wise natural coordinate, ζ_l , as shown in Fig. 9. This is achieved by suitably modifying the variable ζ to ζ_l in any l -th layer such that ζ_l varies from -1 to 1 in that layer. The correlation between the natural layer-wise thickness coordinate and the natural thickness coordinate for the element can be written as

$$\zeta = -1 + \left[t_l(\zeta_l - 1) + 2 \sum_{j=1}^{N_L} t_j \right] / t \quad (3.27)$$

where t_j , t_l are the summed thickness of the preceding layers and the thickness of the l -th layer, and t denotes the total thickness.

Before integration of the element matrices and vectors is done, the natural layer-wise thickness coordinate is substituted into the equation to replace the natural thickness coordinate. Eq. (3.27) yields:

$$d\zeta = \frac{t_l}{t} d\zeta_l \quad (3.28)$$

which substituted into the matrices and vectors.

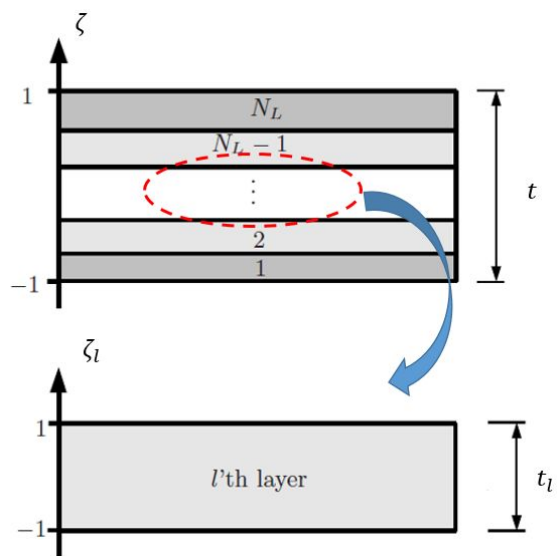


Fig. 9 The transformation of the natural thickness coordinate to a layer-wise natural coordinate

3.6 Nonlinear Solution Techniques

By substituting Eqs. (3.14) through (3.28) into Eq. (2.30), the resulting nonlinear equations of motion are obtained as

$$\mathbf{M}\ddot{\mathbf{q}} + \mathbf{C}\dot{\mathbf{q}} + [\mathbf{K}_L + \mathbf{K}_{CF} + \mathbf{K}_{NL}(\mathbf{q})]\mathbf{q} = \mathbf{R} \quad (3.29)$$

where, \mathbf{K}_L , \mathbf{K}_{CF} and \mathbf{M} are symmetric matrices, while \mathbf{C} is a skew symmetric matrix. The unbalance force vector \mathbf{R} , due to the external load and internal unbalanced force, is defined as

$$\mathbf{R} = \mathbf{R}_E + \mathbf{F}_{CF} + \mathbf{F}_B - \mathbf{R}_I \quad (3.30)$$

where \mathbf{R}_E and \mathbf{F}_B denote the force vectors induced by the external forces and the body forces.

The equations of motion can be solved by assuming that the motion of the blade is composed of the following two components: a static converged deflection \mathbf{q}_s due to the centrifugal and external loads and a small linear time-dependent perturbation \mathbf{q}_d about the static displaced position. Therefore, the nodal displacement vector \mathbf{q} can be expressed as the sum of the static and dynamic terms as

$$\mathbf{q} = \mathbf{q}_s + \mathbf{q}_d \quad (3.31)$$

The static geometrically nonlinear equations of motion are solved by neglecting the time dependent motion of Eq. (3.31), such that

$$\begin{aligned} \mathbf{K}_T \mathbf{q}_s &= \mathbf{R} \\ (\mathbf{K}_T &= \mathbf{K}_L + \mathbf{K}_{CF} + \mathbf{K}_{NL}) \end{aligned} \quad (3.32)$$

where \mathbf{K}_T is the usual tangent stiffness matrix evaluated at the nonlinear static equilibrium position. The tangent stiffness matrix in Newton-Raphson method needs to be updated for each iteration step. To circumvent this computational difficulty, especially for large scale structural problem, the stiffness matrix may be held constant for several iterations and then updated only when necessary. This approach is usually called the modified Newton-Raphson method. In the modified Newton-Raphson method, the tangent stiffness matrix is constant over a few iterations. The convergence of the modified Newton-Raphson approach is slower than that of the Newton-Raphson method and thus more iteration is required to achieve convergence to the same accuracy. As shown in Fig. 10, the Newton-Raphson method is used to solve the nonlinear form of the equations of motion.

On substituting Eq. (3.31) into Eq. (3.29), the equations of motion can be written in terms of the static and dynamic terms as

$$\mathbf{M}\ddot{\mathbf{q}}_d + \mathbf{C}\dot{\mathbf{q}}_d + [\mathbf{K}_L + \mathbf{K}_{CF} + \mathbf{K}_{NL}(\mathbf{q})](\mathbf{q}_s + \mathbf{q}_d) = \mathbf{R} \quad (3.33)$$

For the dynamic analysis, one takes only the first order term in the Taylor series expansion of $\mathbf{K}_{NL}(\mathbf{q})$ about \mathbf{q}_s . Thus, the tangent stiffness can be written as

$$\mathbf{K}_T = \mathbf{K}_L + \mathbf{K}_{CF} + \frac{\partial}{\partial \mathbf{q}} \{[\mathbf{K}_{NL}(\mathbf{q})]\mathbf{q}\}_{\mathbf{q}=\mathbf{q}_s} \quad (3.34)$$

Substituting Eq. (3.34) into Eq. (3.33), and neglecting products of the perturbation quantities, the dynamic equations of motion are obtained as

$$\mathbf{M}\ddot{\mathbf{q}}_d + \mathbf{C}\dot{\mathbf{q}}_d + \mathbf{K}_T\mathbf{q}_d = 0 \quad (3.35)$$

The second order governing equation, as shown in Eq. (3.35), can be rearranged into the first order derivative equation to extract the eigenfrequencies and mode shapes as

$$\mathbf{A}\mathbf{s} - \mathbf{E}\dot{\mathbf{s}} = 0 \quad (3.36)$$

$$\mathbf{A} = \begin{bmatrix} \mathbf{M} & \mathbf{0} \\ \mathbf{0} & \mathbf{K}_T \end{bmatrix}, \quad \mathbf{E} = \begin{bmatrix} \mathbf{0} & \mathbf{M} \\ -\mathbf{M} & -\mathbf{C} \end{bmatrix}, \quad \mathbf{s} = \begin{Bmatrix} \dot{\mathbf{q}}_d \\ \mathbf{q}_d \end{Bmatrix} \quad (3.37)$$

By assuming that the solution is of the form $\mathbf{s} = e^{\lambda t}$, Eq. (3.36) can be rewritten as

$$\mathbf{E}^{-1}\mathbf{A} - \lambda\mathbf{I} = 0 \quad (3.38)$$

Since Eq. (3.29) is a nonlinear equation, the solution procedure, which consists of obtaining an initial deformation from Eq. (3.32) and evaluating the eigenvalues and eigenvectors of the oscillatory motion in Eq. (3.35), has an iterative procedure. Therefore, a termination criterion would be required for such iterative procedure control. In the present thesis, the nodal displacement vectors \mathbf{q} and unbalance force vector \mathbf{R} were considered as controlled quantities which were needed to satisfy the following equations, simultaneously.

$$\delta_1 = \frac{\|\Delta\mathbf{q}^{i+1}\|}{1 + \|\mathbf{q}^i\|} \leq 0.1\% \quad (3.39)$$

$$\delta_2 = \frac{\|\Delta\mathbf{R}^{i+1}\|}{1 + \|\mathbf{R}_E + \mathbf{F}_{CF} + \mathbf{F}_B\|} \leq 0.1\% \quad (3.40)$$

where $\| \ \|$ denotes the Euclidean norm and the superscript i denotes the i -th iteration. $\Delta\mathbf{q}^{i+1}$ denotes the solution increments, and is obtained as

$$\Delta\mathbf{q}^{i+1} = \mathbf{q}^{i+1} - \mathbf{q}^i \quad (3.41)$$

In general, the solution \mathbf{q}^{i+1} will not satisfy the original nonlinear system of equations and there will be some residual, defined as

$$\Delta\mathbf{R}^{i+1} = \mathbf{R}_E + \mathbf{F}_{CF} + \mathbf{F}_B - \mathbf{R}_I^{i+1} \quad (3.42)$$

If the residual $\Delta \mathbf{R}^{i+1}$ is small, the solution \mathbf{q}^{i+1} can be accepted as the correct solution. Otherwise, the process is repeated until this residual becomes lower than the termination criterion. Details of the solution procedure are given in Fig. 10.

Step-1: Initial values

- $i = 0$; $\Delta \mathbf{u}^{(i)} = 0$; $\mathbf{u}^{(i)}$ from the last known configuration

Step-2: Updated at element level for iteration: $(i + 1)$

- Nodal displacement: $\mathbf{q}^{(i+1)} = \mathbf{q}^{(i)} + \Delta \mathbf{q}^{(i)}$
- Nodal coordinate: $\mathbf{x}^{(i+1)} = \mathbf{x}^{(i)} + \Delta \mathbf{x}^{(i)}$

Step-3: Element stiffness matrix and unbalance force vector

- $\mathbf{k}_T^{(i+1)} = \mathbf{k}_L + \mathbf{k}_{CF} + \mathbf{k}_{NL}^{(i+1)}$
- $\mathbf{r}^{(i+1)} = \mathbf{r}_E + \mathbf{f}_{CF} + \mathbf{f}_B - \mathbf{r}_I^{(i+1)}$

Step-4: Assemble global matrices and vectors

- $\mathbf{K}_T^{(i+1)}$, $\mathbf{R}^{(i+1)}$

Step-5: Solve the incremental displacement and check for convergence

- $\Delta \mathbf{q}^{(i+1)} = [\mathbf{K}_T^{(i+1)}]^{-1} \mathbf{R}^{(i+1)}$
if $\delta_1 < Tol$ and $\delta_2 < Tol$
go to next step
else
k = k + 1; return Step-2
end

Step-6: Element mass matrix and damping matrix

- \mathbf{m} , \mathbf{c}

Step-7: Assemble global matrices and vectors

- \mathbf{M} , \mathbf{C}

Step 6: Solve the dynamic equation of motion

- $\mathbf{q} = \mathbf{q}_s + \mathbf{q}_d$; sum of the static and dynamic terms
- $\mathbf{M}\ddot{\mathbf{q}}_d + \mathbf{C}\dot{\mathbf{q}}_d + \mathbf{K}_T\mathbf{q}_d = 0$; second order form
- $\mathbf{E}^{-1}\mathbf{A} - \lambda\mathbf{I}\mathbf{s} = 0$; rearranged into first order form to evaluate the eigenvalues and eigen-vectors

Fig. 10 Solution procedure for the static and dynamic analysis

3.7 Model Reduction Method

Reduction methods were used to reduce the number of DOFs in a finite-element model. The reduced solution's fidelity depends on the reduction method implemented. Most of the reduction methods were developed to efficiently determine the natural frequencies and mode shapes of large finite element models.

For all model reduction techniques, the original nodal displacement vector, \mathbf{q} , is partitioned into the master “m” DOF and the slave “s” DOF. Thus, \mathbf{q} can be written as

$$\mathbf{q} = \begin{Bmatrix} \mathbf{q}_m \\ \mathbf{q}_s \end{Bmatrix} = \mathbf{T}\mathbf{q}_m \quad (3.43)$$

The transformation matrix \mathbf{T} takes on various forms depending on the reduction technique utilized. The reduced mass, damping and stiffness matrices are denoted as \mathbf{M}_r , \mathbf{C}_r and \mathbf{K}_r , and the relation between the full-size matrices and their reduced counterparts can be written as

$$\begin{aligned} \mathbf{M}_r &= \mathbf{T}^T\mathbf{M}\mathbf{T} \\ \mathbf{C}_r &= \mathbf{T}^T\mathbf{C}\mathbf{T} \\ \mathbf{K}_r &= \mathbf{T}^T\mathbf{K}\mathbf{T} \end{aligned} \quad (3.44)$$

3.7.1 Static Reduction

Static reduction, sometimes referred to as Guyan reduction [55], is the most popular reduction method. The nodal deflection and force vectors, \mathbf{q} and \mathbf{F} , and the mass and stiffness matrices, \mathbf{M} and \mathbf{K} , are re-ordered and partitioned into separate quantities relating to master and slave DOFs. Assuming that no force is applied to the slave DOF and the damping is negligible, the equation of motion of the structure becomes

$$\begin{bmatrix} \mathbf{M}_{mm} & \mathbf{M}_{ms} \\ \mathbf{M}_{sm} & \mathbf{M}_{ss} \end{bmatrix} \begin{Bmatrix} \ddot{\mathbf{q}}_m \\ \ddot{\mathbf{q}}_s \end{Bmatrix} + \begin{bmatrix} \mathbf{K}_{mm} & \mathbf{K}_{ms} \\ \mathbf{K}_{sm} & \mathbf{K}_{ss} \end{bmatrix} \begin{Bmatrix} \mathbf{q}_m \\ \mathbf{q}_s \end{Bmatrix} = \begin{Bmatrix} \mathbf{F}_m \\ \mathbf{0} \end{Bmatrix} \quad (3.45)$$

The slave DOF should be chosen where the inertia is low and the stiffness is high so that the mass is well connected to the structure. Conversely the master DOFs are chosen where the inertia is high and the stiffness is low. By neglecting the inertia terms in the second set of Eq. (3.45), the slave DOF may be eliminated so that

$$\begin{Bmatrix} \mathbf{q}_m \\ \mathbf{q}_s \end{Bmatrix} = \begin{bmatrix} \mathbf{I} \\ -\mathbf{K}_{ss}^{-1}\mathbf{K}_{sm} \end{bmatrix} \mathbf{q}_m = \mathbf{T}_S \mathbf{q}_m \quad (3.46)$$

where \mathbf{T}_S denotes the static transformation between the full displacement vector and the master coordinates.

Generally, the static reduction is a good approximation for the lower mode eigen-frequencies and eigenvectors, respectively. The inherent

drawback of the static reduction process is that the mass of the reduced system is not effectively preserved and therefore will generally produce reduced model frequencies that are higher than those of the original full order model. Also, the quality of the eigenvalue approximation decreases as the mode number increases.

3.7.2 *IRS(Improved Reduction System) Reduction*

O'Callahan [56] improved the static reduction method by introducing a technique known as the Improved Reduced System (IRS) method. As an extension of the Guyan reduction process, the IRS was developed in an attempt to account for some of the effects of the slave DOFs that cause in the Guyan reduction process. The IRS transformation, \mathbf{T}_{IRS} , can be written as

$$\mathbf{T}_{IRS} = \mathbf{T}_S + \mathbf{SMT}_S\mathbf{M}_r^{-1}\mathbf{K}_r \quad (3.47)$$

$$\mathbf{S} = \begin{bmatrix} \mathbf{0} & \mathbf{0} \\ \mathbf{0} & \mathbf{K}_{ss}^{-1} \end{bmatrix}$$

where \mathbf{M}_r and \mathbf{K}_r are the reduced mass and stiffness matrices obtained from Guyan reduction or any other static condensation. Adjustment terms to the Guyan reduction process allow for the better representation of the mass associated with the slave DOF. IRS method improves on the accuracy of the reduced model when compared to Guyan reduction especially for the higher modes of the system.

Chapter 4. Verification Problems

The present finite element formulations and solution procedures were applied for the static and dynamic analysis of beam, plate and shell structures with the geometric nonlinearities and composite construction. In order to validate the accuracy and reliability of the present finite element formulations, the present numerical results were compared to the several benchmark problems.

4.1 Static Behavior

4.1.1 Cantilevered Beam under Shear Force

The cantilevered beam is presented in Fig. 11, and it has length $L=10\text{m}$, width $C=1\text{m}$, and thickness $h=0.1\text{m}$, respectively. Regarding the force boundary condition, it is subject to an upward shear force at the free end and the shear force is assumed to maintain the same direction during the deformation. The Young's modulus of elasticity of the beam is $E=1.2\text{ GPa}$ and the Poisson's ratio is $\nu=0.3$. This problem has been examined by many researchers to evaluate their own geometrically nonlinear finite element formulations. For the numerical analysis, the cantilevered beam was discretized by $1 \times 15 \times 1$ meshes (DOFs: 810), and the total load was applied in twenty equal load steps.

Fig. 12 shows the undeformed and deformed configuration of the cantilever beam for various load steps. From this figure, the cantilevered beam experience bending about the y-axis. Both horizontal and vertical deflections at point A with respect to each load step are shown in Fig. 13. Since the present solid-shell element provides no nodes in the middle surface of the shell, the associated displacements were calculated by averaging the displacements of the lower and upper surfaces. The response with the present solid-shell element were compared with the finite element results those given by Sze et al. [57] who used the commercial code ABAQUS. It can be seen that the results calculated by the present solid-shell element show excellent agreement with the results obtained by Sze et al.

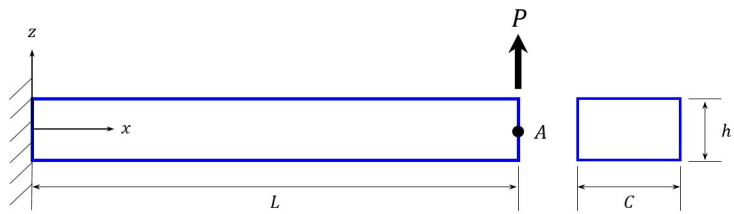


Fig. 11 Cantilevered beam subject to a shear force, $P_{\max}=4\text{kN}$

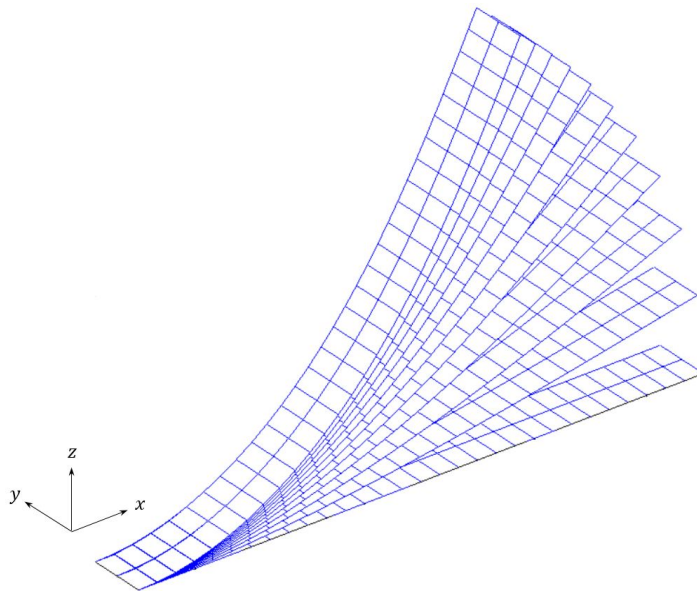


Fig. 12 Deformed configurations of cantilevered beam for various load steps

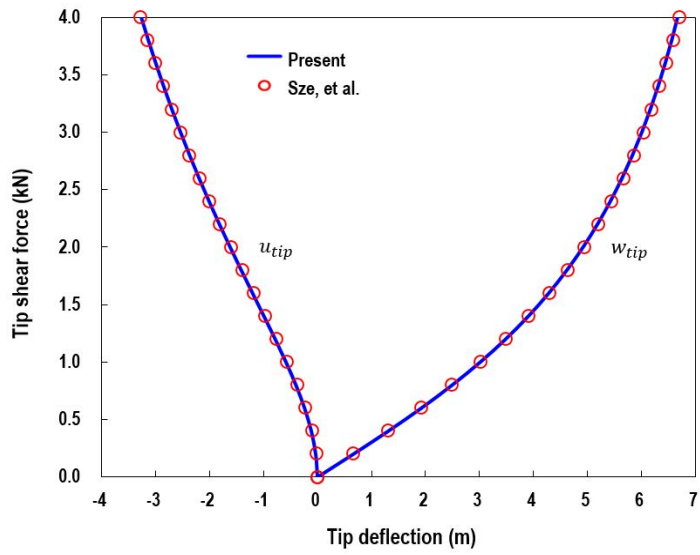


Fig. 13 Cantilevered beam, load-deflection curves predicted at point A

4.1.2 Ring Plate under the Uniform Line Load

As shown in Fig. 14, the clamped ring plate has inner radius $R_i=6\text{m}$, outer radius $R_o=10\text{m}$, and thickness $h=0.03\text{m}$, respectively. This problem consists of a circular plate with radial cut, which is pulled with transverse direction through the application of uniformly distributed line load ($P_{\max}=0.45\text{N/m}$). In the present thesis the ring plate is modeled by standard Cartesian coordinates. A mesh of $5\times 30\times 1$ (DOFs: 8,100) elements were used to discretize the ring plate, and the total external load was applied in twenty equal load steps. The material properties of the isotropic and orthotropic cases are given Table 1.

In case of layered laminates, the stacking sequences $[0^\circ/90^\circ/0^\circ]$ and $[-45^\circ/45^\circ/-45^\circ/45^\circ]$ were considered. Fig. 15 shows the deformed configuration of the ring plate for various load steps, and it shows that the plate experiences large displacements. Since this structure was similar to a thin-walled structure, the transverse shear locking phenomenon may would probably appear. Fig. 16 shows the load-displacement paths obtained at node B, and fairly reliable results were obtained with no sign of the locking phenomenon. The present converged predictions are well comparable to the results by Arciniega et al. [58].

Table 1. Material properties of the ring plate

(a) Isotropic case

Properties	Dimensions
E	21.0 MPa
ν	0.0

(b) Orthotropic case

Properties	Dimensions
E_{11}	20.0 MPa
E_{22}, E_{33}	6.0 MPa
G_{12}, G_{13}	3.0 MPa
G_{13}	2.4 MPa
ν_{12}, ν_{13}	0.3
ν_{23}	0.25

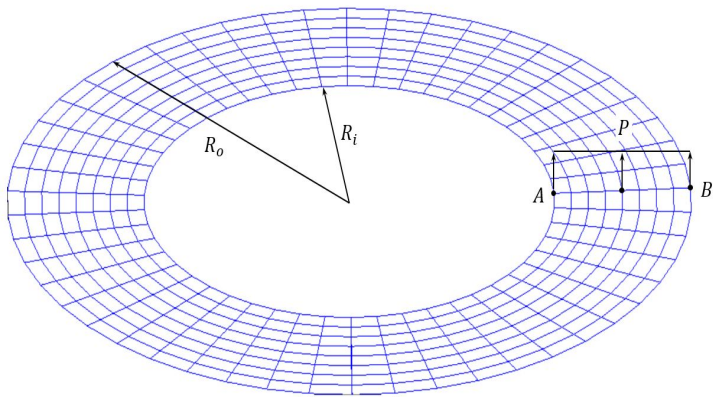


Fig. 14 Ring plate under the uniform line load, $P_{\max}=0.45\text{N/m}$

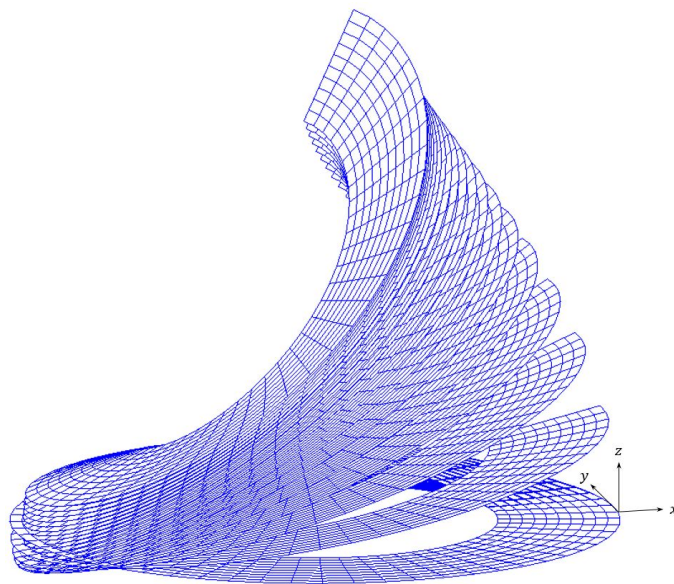


Fig. 15 Deformed configuration of ring plate under the uniform line load

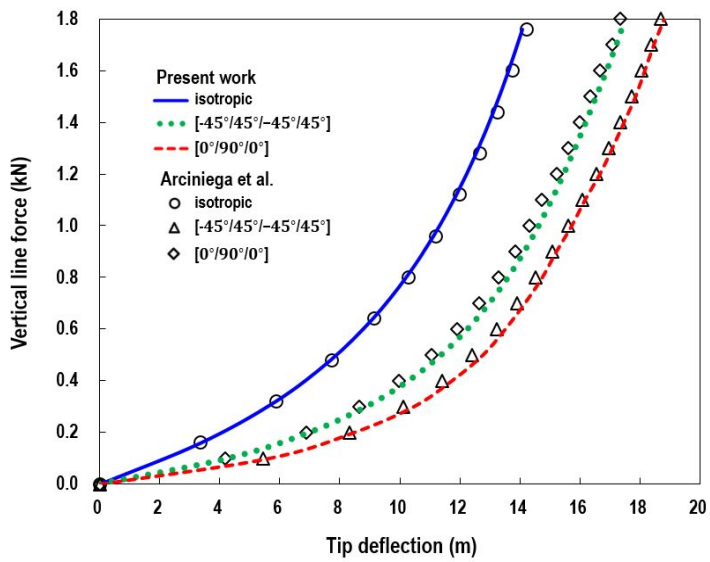


Fig. 16 Ring plate, load-deflection curves predicted at point B

4.1.3 Pinched Semi-Cylindrical Shell

The well-known benchmark for cylindrical shells is the pinched semi-cylinder. It is clamped at one end and subject to a concentrated downward force at the middle of the free end, as shown in Fig. 17. This is rigorous examination for the present solid-shell element regarding both inextensional bending and complex membrane states. The shell model has the length $L=304.8\text{mm}$, radius $R=101.6\text{mm}$, and thickness $h=3\text{mm}$, respectively. The material properties of the isotropic and orthotropic cases are given Table 2. Due to the symmetry of geometry, as well as loading and boundary conditions, only one half of the shell was discretized by $15 \times 15 \times 1$ (DOFs: 12,150) meshes.

For an orthotropic material, two stacking sequences, $[0^\circ/90^\circ/0^\circ]$ and $[90^\circ/0^\circ/90^\circ]$, were analyzed that had the same geometry and boundary conditions as those in the isotropic case. The total load was applied in twenty five equal load steps. Fig. 18 shows deformed configuration of the semi-cylindrical shell model. Load-displacement paths obtained at node point A with isotropic and two different ply layups are depicted in Fig. 17. The solutions of the present thesis and the results by Arciniega et al. [58] are quite close to each other.

Table 2. Material properties of the semi-cylindrical shell

(a) Isotropic case

Properties	Dimensions
E	2.068 GPa
ν	0.3

(b) Orthotropic case

Properties	Dimensions
E_{11}	2.068 GPa
E_{22}, E_{33}	517.1 MPa
G_{12}, G_{13}	795.6 MPa
G_{23}	198.9 MPa
$\nu_{12}, \nu_{13}, \nu_{23}$	0.3

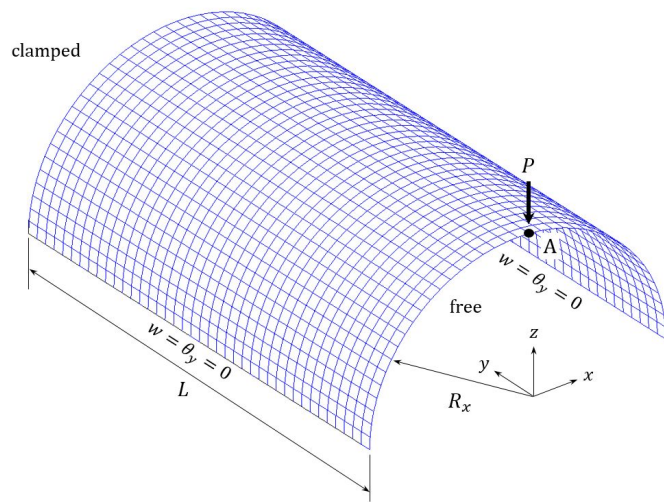
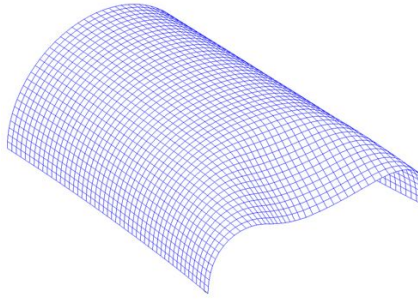
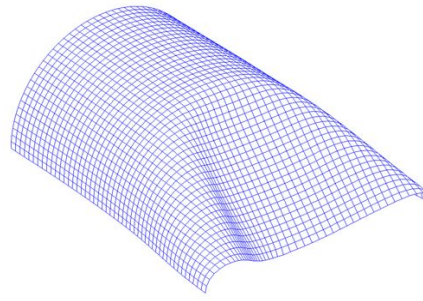


Fig. 17 Semi-cylindrical shell subject to a concentrated load,

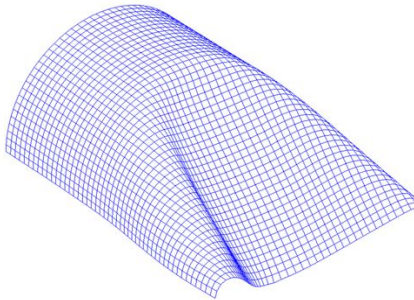
$$P_{\max} = 2\text{kN}$$



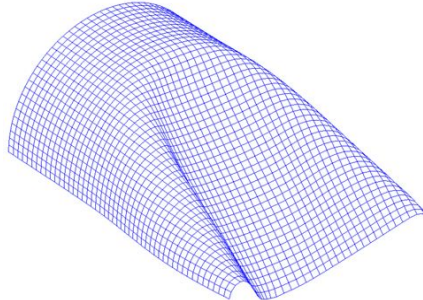
(a) $P=500\text{N}$



(b) $P=1,000\text{N}$



(c) $P=1,500\text{N}$



(d) $P=2,000\text{N}$

Fig. 18 Deformed configuration of semi-cylindrical shell subject to a concentrated tip load

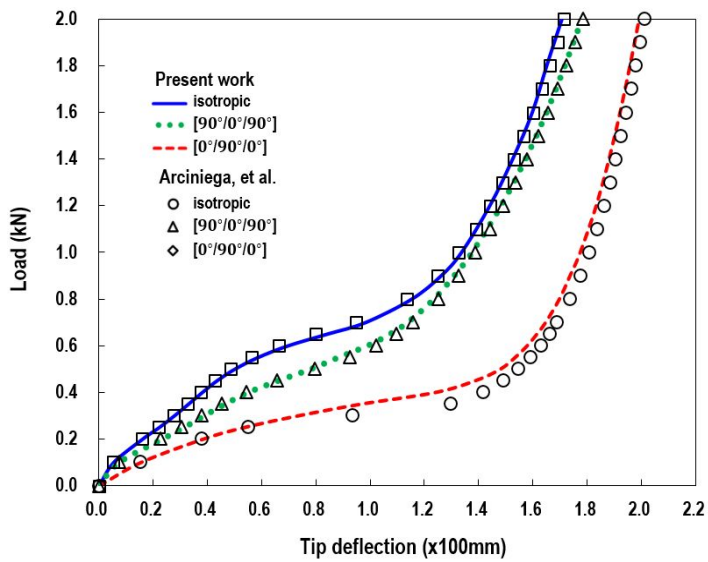


Fig. 19 Semi-cylindrical shell, load-deflection curves predicted at point A

4.2 Dynamic Behavior

4.2.1 Plate-Type Blade Model

The present finite element formulations were used for the study of free vibration of twisted plates with the assumption of uniform pre-twist, having a twist angle of ϕ at the free edge. In this section, the symbols “FB” denotes the flap bending modes, “T” the torsional modes, “EB” and “CB” the edgewise and chordwise bending modes. The frequencies are classified with respect to their predominant mode of vibration. Also, the resulting frequencies are presented in the non-dimensional form as follows:

$$\bar{\omega} = \omega_1 \sqrt{\rho h L^4 / D} \quad (4.1)$$

where $D = Eh^3/12(1 - \nu^2)$ is the flexural rigidity of the plate in which E is the elastic modulus and ν is Poisson’s ratio. In this section, the plate model has length $L=305\text{mm}$, and the material properties are $E=200\text{GPa}$ and $\nu=0.3$. The full plate model was discretized by $8 \times 8 \times 1$ (DOFs: 3,456) meshes.

Firstly, the plate with aspect ratio $L/C=1.0$ was considered, and five twist angles $\phi=0^\circ, 15^\circ, 30^\circ, 45^\circ$ and 60° , and a thickness ratio $C/h=20$ were selected. The present analysis results were compared with those given by Sinha and Turner [59] who used the thin shell theory and the

commercial code ANSYS. For the case of the pre-twist angle $\phi=0^\circ$ and 15° , three results agree well except for the first and second torsion frequencies. When the pre-twist angle ϕ is higher than 30° , there are differences in the first edgewise bending, the second flap bending and torsion modes. The present results are much closer to the ANSYS analysis results than those obtained by the thin shell theory. However, they have the same tendency to decrease the frequency parameters with respect to the pre-twist angle.

Secondly, the plate with a thickness ratio $C/h=5$ was selected. The variations of the flap and torsion frequencies with respect to the twist angle are given in Table 4. Three results predict similar trends in the variation of natural frequencies with increase in twist angle. However, the present flap bending and torsion frequencies are lower than those results obtained by the shell theory [59]. In general, the stiffness of plates increases when transverse shear deformation is excluded. Thus, it is possible that the thin shell results are slightly stiffer than the present and ANSYS analysis results. Also, it can be observed that the first five frequency parameters are decreased as the plate thickness increases.

Table 3. Nondimensional frequencies of pre-twisted plates: $L/C=1$,
 $C/h=20$

Mode	Analysis results	Total twist (ϕ)				
		0°	15°	30°	45°	60°
	Present	3.471	3.459	3.423	3.372	3.314
1FB	ANSYS [59]	3.463	3.446	3.396	3.319	3.223
	Sinha et al. [59]	3.516	3.575	3.643	3.555	3.260
	Present	8.430	10.394	14.415	18.518	21.940
1T	ANSYS [59]	8.344	10.320	14.340	18.399	21.747
	Sinha et al. [59]	8.054	8.958	11.533	15.550	20.901
	Present	21.333	20.698	18.981	16.836	14.801
2FB	ANSYS [59]	20.982	20.308	18.506	16.264	14.108
	Sinha et al. [59]	22.005	21.806	21.252	20.446	19.493
	Present	26.982	26.896	34.802	38.397	47.186
1EB	ANSYS [59]	26.668	26.590	34.124	37.504	44.767
	Sinha et al. [59]	25.704	27.334	32.137	39.779	49.913
	Present	30.667	31.843	46.454	56.630	67.052
2T	ANSYS [59]	30.072	31.239	46.065	54.356	66.446
	Sinha et al. [59]	31.491	33.730	40.749	52.495	68.083

Table 4. Nondimensional frequencies of pre-twisted plates: $L/C=1$,
 $C/h=5$

Mode	Analysis results	Total twist (ϕ)				
		0°	15°	30°	45°	60°
	Present	3.343	3.343	3.306	3.253	3.191
1FB	ANSYS [59]	3.368	3.352	3.304	3.232	3.140
	Sinha et al. [59]	3.521	3.579	3.644	3.553	3.257
	Present	7.471	7.559	7.792	8.091	8.313
1T	ANSYS [59]	7.430	7.518	7.753	8.071	8.401
	Sinha et al. [59]	7.937	8.071	8.458	9.098	10.039
	Present	17.964	17.993	18.047	18.058	17.972
2FB	ANSYS [59]	17.909	17.961	18.059	18.084	17.943
	Sinha et al. [59]	21.561	21.373	20.849	20.084	19.176
	Present	22.843	22.758	22.511	22.128	21.638
1EB	ANSYS [59]	22.745	22.661	22.427	22.088	21.680
	Sinha et al. [59]	21.166	20.605	19.790	19.750	20.719
	Present	24.543	24.506	24.395	24.212	23.957
2T	ANSYS [59]	24.345	24.253	23.986	23.562	23.012
	Sinha et al. [59]	30.408	30.579	31.174	32.346	34.179

4.2.2 Shell-Type Blade Model

The free vibration characteristics of a rotating steel fan blade were investigated next, and Fig. 20 shows a simplified open cylindrical shell type structure. The fan blade model is clamped at one end, and the rotating axis is taken to be at the center of the clamped edge. Also, it has aspect ratio $L/C=1.0$, length $L=305\text{mm}$, radius $R_x=2C$, and the thickness $h=L/100$, respectively. The aspect ratio is defined as the ratio of length to width of a blade as $AR=L/C$. Its isotropic material properties are $E=200\text{GPa}$, $\nu=0.3$, $\rho=7,860\text{Kg/m}^3$. This problem has been studied by several researchers [38, 40]. They presented analytical solutions regarding the natural frequencies and mode shapes. However, those research works are limited to linear analyses. In this section, the shell structure was discretized by $8\times 8\times 1$ meshes (DOFs: 3,456), and the geometric nonlinear terms were purposely excluded for the valuable comparison. The natural frequencies of the rotating blade were calculated and compared to both experimental and analytical prediction results of previous studies. The present prediction results show a good agreement with those of Leissa et al. [38] and Xu [40]. The comparison results are given in Table 5.

Table 5. Natural frequencies (Hz) of an open cylindrical shell blade

Mode Number	Non-rotating blade			Rotating blade ($\Omega = \omega_1$)		
	Measured [38]	Present	Diff. (%)	Analytic [40]	Present	Diff. (%)
1	85.6	85.7	0.1	150.7	151.8	0.7
2	134.5	138.4	2.9	173.0	171.8	-0.7
3	259.0	249.9	-3.5	296.6	299.0	0.8
4	351.0	346.4	-1.3	419.0	418.1	-0.2
5	395.0	389.5	-1.4	459.8	458.8	-0.2
6	531.0	541.0	1.9	572.6	582.5	1.7
7	743.0	742.9	0.1	800.4	787.4	-1.6
8	751.0	748.7	-0.3	817.2	822.4	0.6

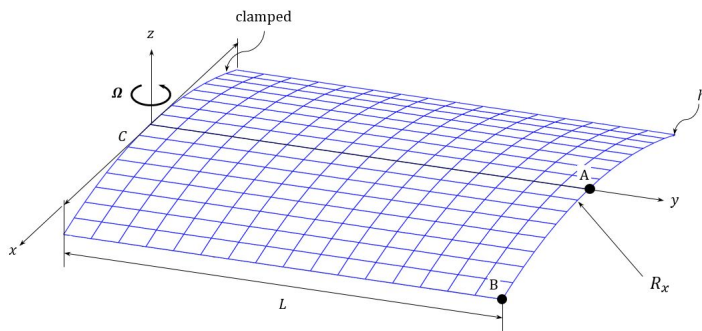


Fig. 20 Configuration of a rotating shell type blade

Chapter 5. Vibration Analysis of Shell Type

Blades

5.1 Effect of Geometric Nonlinearity

Shells are common structural elements in many engineering structures, including exteriors of rockets, wings and fuselages of airplanes, ship hulls, containers of liquids, oil tanks etc. It can be made from a single layer or multilayer of isotropic or anisotropic materials. Shells can be classified according to their curvatures, such as shallow or deep shells. In this section, the effect of geometric nonlinearity upon the vibration characteristics of shell type rotating blades was investigated. The blade model has the same material properties and dimensions as the steel fan blade in Section 4.2.2. Also, the nondimensional rotating speed is defined as $\bar{\Omega}=\Omega/\omega_1$ in which ω_1 represents the fundamental natural frequency of the non-rotating blade.

5.1.1 Shallow Shell Model

Fig. 21 shows the variations of the first five natural frequencies of the shallow shell type blade, $R_x=2C$, with respect to the nondimensional rotating speed $\bar{\Omega}$ which varies from 0.0 to 1.0. In this section, the symbols “FB”, “CB”, and “T” denote the flap bending, chordwise

bending and torsion modes. In case of the linear analysis, the effect of rotation was to increase frequencies of all the modes. However, when including the geometric nonlinear terms, the rotational effect was found to be different in specific mode. In case of the third mode (first chordwise bending mode), the difference between the nonlinear and linear analysis results was approximately 7 % at the rotating speed of $\bar{\Omega}=1.0$. To find out why this frequency drop happens, the static vertical deflections were investigated. The nonlinear and linear vertical deflections of point A and B with respect to the rotating speeds are shown in Fig. 22. The nonlinear deflections of point A at the center of the free edge are higher than the linear analysis results, and the maximum difference is 23 %. Moreover, the nonlinear deflections of point B at the end of the free edge are close to the linear case, but the nonlinear analysis results are 4% lower than the linear analysis results. The reason for this is that the chordwise bending stiffness is decreased because the centrifugal force attempts to flatten the blade in chordwise direction. This decrease in the chordwise bending stiffness enforces the third-mode natural frequencies to become smaller than the corresponding linear frequencies.

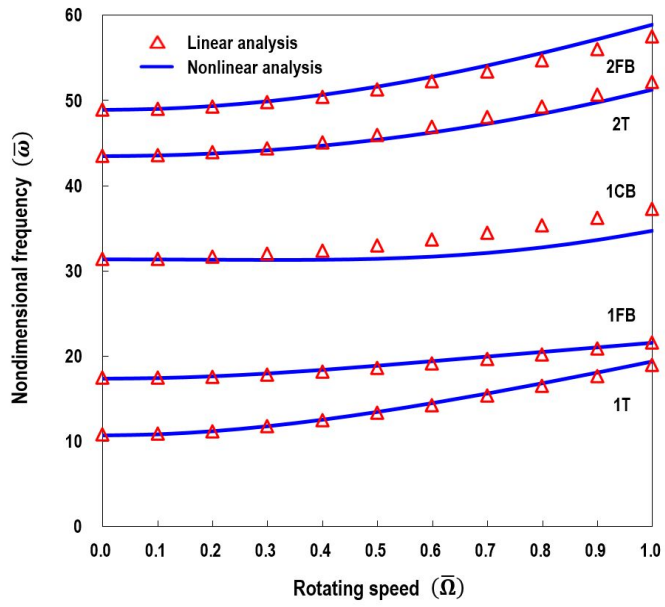


Fig. 21 Non-dimensional frequencies of the shallow shell model,

$$R_x=2L$$

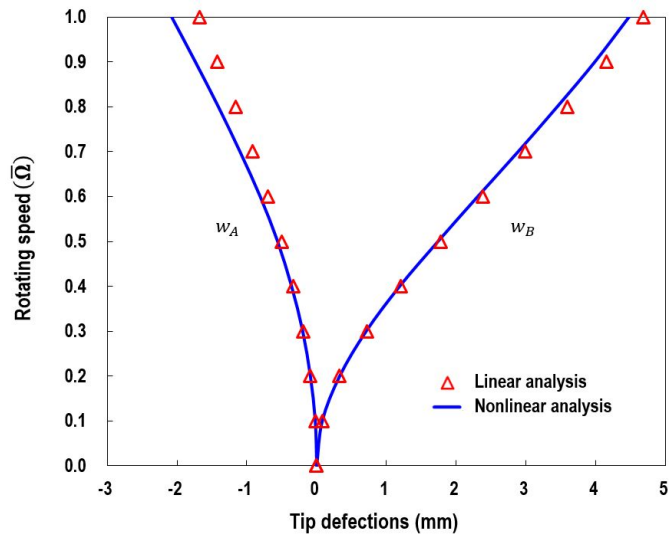


Fig. 22 Vertical deflections of the shallow shell model, $R_x=2L$

5.1.2 Deep Shell Model

The effect of the blade curvatures was investigated next. Fig. 23 shows the variations of the first five natural frequencies of the deep shell type blade, $R_x=C$, with respect to the nondimensional rotating speed. It is seen that the nonlinear torsional and flap bending frequencies are higher than the corresponding linear analysis results. On the contrary, the first chordwise bending frequency is decreased first in terms of the rotating speed, and then it shows an upward trend. The maximum difference between the nonlinear and linear analysis result is about 26 % at the rotating speed of $\bar{\Omega}=0.9$. Further, the second and third frequencies approach each other quite closely as the rotating speed increases. However, frequency crossing does not occur. The frequency loci diverge in a manner referred to as “curve veering”. The curve veerings, also known as avoided crossings, or eigenvalue avoidance, are observed in plots of eigenvalues versus a system parameter. In particular, a veering refers to a region in which two eigenvalue loci approach each other and almost cross as the system parameter is changed, but instead of crossing they appear to veer away from each other, with each locus then following the previous path of the other. Although this phenomenon was initially regarded as an aberration caused by approximation methods applied to the original infinite-dimensional eigenvalue problems, it was shown that the phenomenon can be observed for continuous systems. This behavior was investigated by Leissa [60], and similar phenomena can be found in

references [7, 61].

As shown in Fig. 24, for the case of the deep shell blade, the maximum discrepancies between the nonlinear and linear deflection analysis results are increased by 53% at point A, and increased by 5% at point B at the rotating speed of $\bar{\Omega}=1.0$. Similar to the shallow shell blade, these induce the decrease in the chordwise bending frequencies and increase in flapwise bending frequencies. In addition, to find out the reason of frequency veering phenomena, the modal line patterns of the second and third modes with respect to rotating speeds in the range of $\bar{\Omega}=0.8\sim 1.0$ were investigated, and those results are shown in Fig. 25. It is noted that the modal line patterns of the second and third modes are changed as the rotating speed leaves the curve veering region. For the second mode, it shows primary vertical nodal lines. However, more horizontal nodal lines are involved in the mode as the rotating speed increases. In addition, for the third mode, there exist more vertical modal lines as the rotating speed increases. This affects the flap bending and chordwise bending stiffness of the blade. These results show that the blade curvatures and geometric nonlinearity may significantly influence dynamic characteristics of the shell type blades. Indeed, the linear analysis results did not capture these significant drops in frequency and abrupt frequency loci veering phenomena.

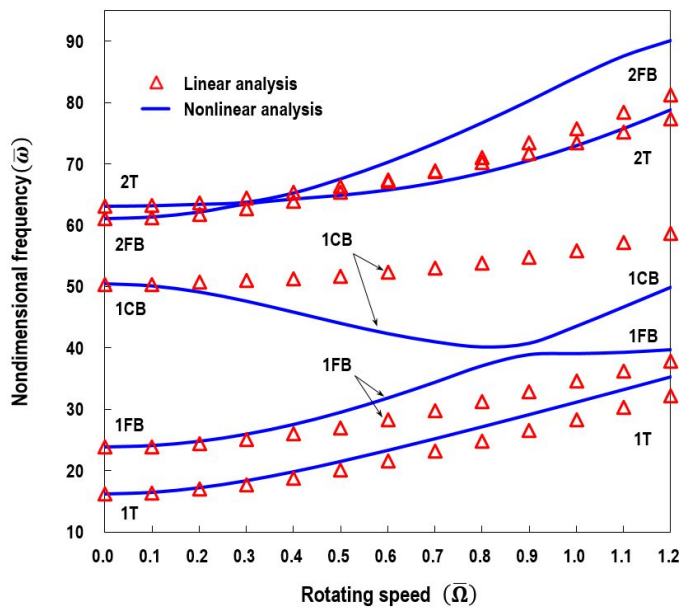


Fig. 23 Non-dimensional frequencies of the deep shell model, $R_x=L$

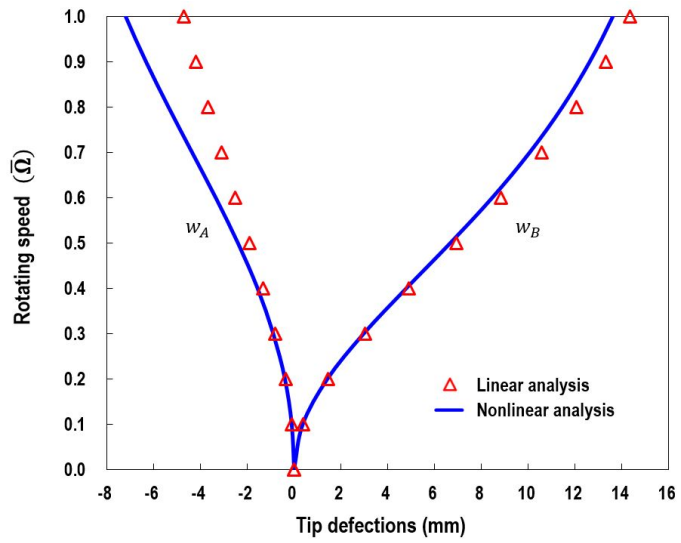


Fig. 24 Vertical deflections of the deep shell model, $R_x=L$

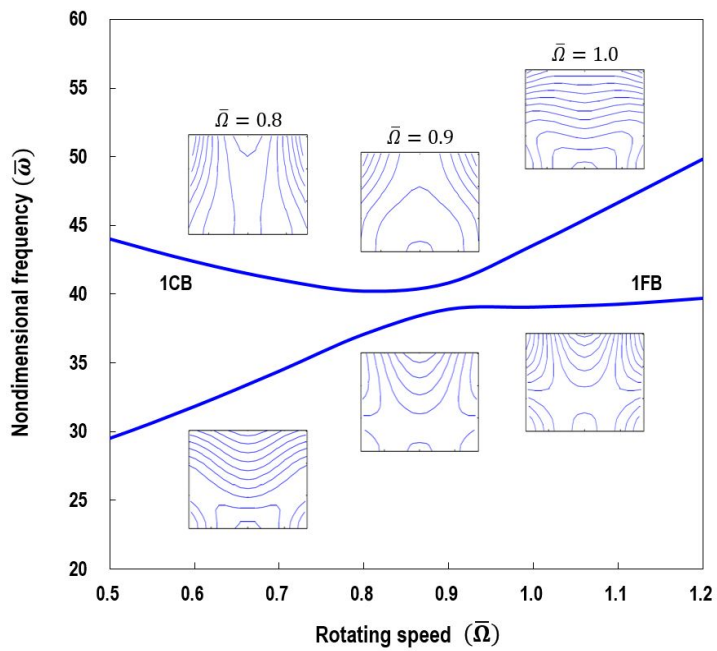


Fig. 25 Nodal line patterns of the second and third mode, deep shell model, $R_x=L$

5.2 Effect of Pre-twist

In this section, the effects of pre-twist on the natural frequencies and mode shapes are investigated. The geometries are the same as shell models in Section 5.1. Also, the material properties of E-glass/Epoxy are given in Table 6. Cantilevered twisted shell-type blades, which have a fixed edge and three free others, are considered as example of the present numerical analysis. The twisting angle is defined as shown in Fig. 4, and assumed to vary linearly on reference of the center of the half width ($C/2$) in the x -direction. Also, the twisting angle ϕ varies from 0° to 45° , and the twisted blade was discretized by $8 \times 8 \times 1$ meshes (DOFs: 3,456).

Firstly, the shallow shell model ($R=2C$) with stacking sequences $[0^\circ/45^\circ/-45^\circ/90^\circ]_S$ is considered. Table 7 shows the effect of twisting angles on natural frequencies of the shallow shell model. The non-dimensional rotating speed varies from 0 to 1. Also, the first five mode shapes of vibration corresponding to three twist angles $\phi=0^\circ$, 30° and 45° are given by Table 8. It is apparent that the change in mode shapes for the un-twisted shells is different from that for the twisted shells. For the case of $\phi=0^\circ$, there are flap bending (the second mode) and chordwise bending (the third mode) mode in the first five modes. As the twist angle increase, there are severe bending-torsion couplings. Since no simple variations found for the mode shapes, it is difficult to distinguish a flap

bending and chordwise bending modes. From the investigation of the shallow shell, it is observed that the fundamental frequency shows monotonic decrease as the twist angle increases. The first vibration modes are the first torsion mode. Therefore, this phenomenon implies that an increase in the twist angle leads to a reduction in the torsional stiffness. Also, the effect of centrifugal stiffening is clearly evident from the monotonic increase of fundamental frequency with increasing rotating speed. However, the nondimensional frequencies of other modes show a downward or upward trend as the rotating speed increases. A possible reason for this behavior is that the coupled bending-torsion frequency can increase or decrease with variation in rotating speed of the blade depending on the relative increments in the blade stiffness.

Secondly, the deep shell model ($R=C$) with stacking sequences $[0^\circ/45^\circ/-45^\circ/90^\circ]_S$ is considered. The effect of twisting angles on natural frequencies of deep shell model is shown in Table 9. Also, the first five mode shapes of vibration corresponding to three twist angles are given by Table 10. From the investigation of the deep shell, it is known that all frequency parameters are higher than the shallow shell model. This is because the curvature influences stiffness of blade. Similar to the shallow shell model, the fundamental frequency shows monotonic decrease as the twist angle increases.

Table 6. Material properties of E-glass/Epoxy

Properties	Dimensions
E_{11}	60.7 GPa
E_{22}, E_{33}	24.8 MPa
G_{12}, G_{13}, G_{23}	12 GPa
$\nu_{12}, \nu_{13}, \nu_{23}$	0.25
ρ	2,000 Kg/m ³

Table 7. Nondimensional frequencies of the twisted cantilevered shells
with $L/C=1$, $C=305\text{mm}$, $C/t=100$, $R_x=2C$

Blade Twist (ϕ)	Rotating speed ($\bar{\Omega}$)	Mode number				
		1	2	3	4	5
0°	0.0	8.74	13.62	23.66	35.83	39.35
	0.5	11.01	15.13	23.55	37.38	41.76
	1.0	15.83	17.46	26.57	42.11	48.02
15°	0.0	5.89	20.35	25.74	37.80	50.30
	0.5	8.19	18.61	26.05	38.80	49.61
	1.0	12.13	17.05	28.21	37.99	43.43
30°	0.0	4.41	20.11	38.94	44.95	52.53
	0.5	6.61	20.82	32.45	49.29	53.95
	1.0	8.91	12.71	29.54	42.33	55.11
45°	0.0	3.84	18.05	46.73	50.80	54.83
	0.5	6.05	19.54	42.28	51.05	56.11
	1.0	8.82	13.63	30.94	54.31	57.49

Table 8. Mode shapes of the twisted cantilevered shells with $L/C=1$,

$C=305\text{mm}$, $C/t=100$, $R_x=2C$, $\bar{\Omega}=1.0$

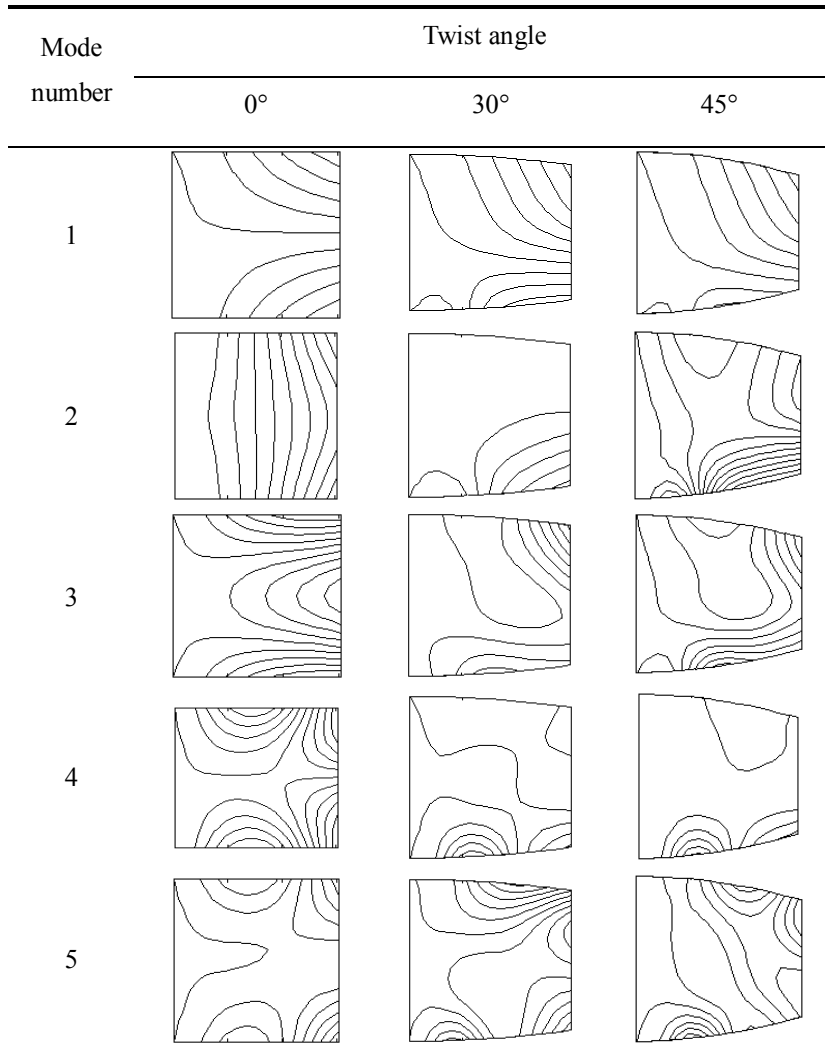
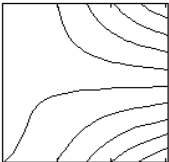
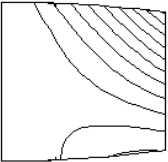
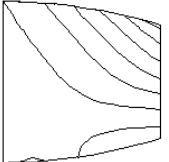
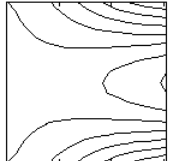
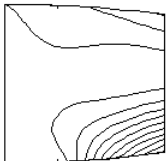
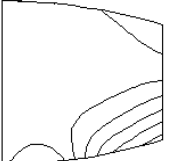
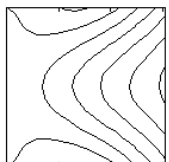
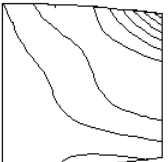
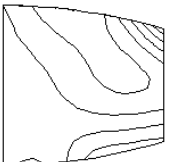
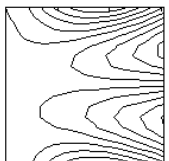
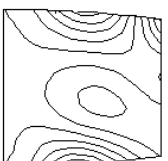
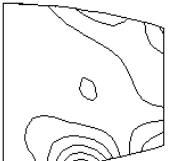
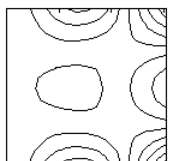
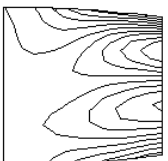
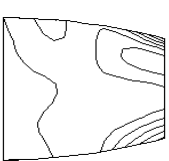


Table 9. Nondimensional frequencies of the twisted cantilevered shells
with $L/C=1$, $C=305\text{mm}$, $C/t=100$, $R_x=C$

Blade Twist (ϕ)	Rotating speed ($\bar{\Omega}$)	Mode number				
		1	2	3	4	5
0°	0.0	12.65	17.17	39.08	45.94	46.66
	0.5	14.85	19.44	36.52	46.18	49.46
	1.0	19.54	25.72	32.30	48.35	56.93
15°	0.0	9.25	24.46	33.54	44.79	48.69
	0.5	11.94	24.36	34.53	45.77	48.10
	1.0	17.28	26.53	32.35	49.28	51.13
30°	0.0	6.66	24.61	38.21	48.15	54.56
	0.5	9.00	27.60	32.17	52.21	54.99
	1.0	13.35	25.37	32.61	51.80	58.14
45°	0.0	5.25	20.34	47.01	50.41	61.80
	0.5	7.38	22.68	38.43	57.97	59.88
	1.0	10.86	20.87	29.38	56.69	64.98

Table 10. Mode shapes of the twisted cantilevered shells with $L/C=1$,
 $C=305\text{mm}$, $C/t=100$, $R_x=C$, $\bar{\Omega}=1.0$

Mode number	Twist angle		
	0°	30°	45°
1			
2			
3			
4			
5			

Chapter 6. Vibration Analysis of Beam Type

Blades

It is well known that the configuration of the rotor blade tip has a significant influence on the overall performance, vibration and noise level of a helicopter. Therefore, most of helicopter industries have considered the application of advanced blade configuration using unique tip shapes such as swept tip and anhedral. The swept tip suppresses shock development on the advancing blade, and has low drag in hover. Anhedral has been used to be good effect on main rotor designs and appears to be effective on the BERP-type tip at high rotor loadings and offers an improved hover figure of merit. For the case of forward flight, anhedral can be useful to balance the effects of sweep and notch offset. Also, it has been used on propellers and tilt-rotor blades. Loading distributions are shown where the peak loading is reduced due to the trailing vortices being further away from the following blade. The review results of helicopter blade tip design technology and corresponding computations to evaluate the performance were summarized by Brocklehurst and Barakos [62].

Epps and Chandra [63] performed an experimental-theoretical investigation of the influence of tip sweep on the natural frequencies of rotating beams. In the present thesis, the material properties and dimensions of solid beam tested by Epps and Chandra were used. The

beam consists of a straight portion and a tip with sweep and anhedral angles relative to the straight portion as shown in Fig. 26. The blade model has the total length of $L=1,016\text{mm}$ that includes the hub radius from the rotating center and tip sweep and anhedral length. Two hub lengths, $h_1=63.5\text{mm}$ and 698.5mm , were considered to investigate the effect of aspect ratios. In addition, the length of the swept tip and anhedral segment are $m=n=152.5\text{mm}$, width $C=25.4\text{mm}$ and thickness $h=1.6\text{mm}$, respectively. In the present work, the beam type blade model was discretized by $1 \times 18 \times 1$ meshes (DOFs: 972). Fifteen finite elements were used at the straight portion of the blade, and the swept and anhedral tip, representing 15% of the blade, were modeled using three finite elements.

6.1 Effect of Tip Sweep Angle

In this section, the influence of sweep angles on the natural frequencies of the isotropic and composite blades were investigated, and those results were compared with the experimental data and one-dimensional nonlinear beam analysis results to assess the availability of the present solid-shell element for analyzing dynamic characteristics of rotorcraft blades. Since the modes are coupled at non-zero tip sweep angles, the frequencies are classified with respect to their predominant mode of vibration. In this section, the symbols “F”, “L”, and “T” denote the flap bending, lag bending and torsion modes.

6.1.1 Isotropic Blade Models

The material properties of isotropic blade models are $E=6.89$ GPa, $\nu=0.3$ and $\rho=2,700$ Kg/m³, and the tip sweep angle Λ varies from 0° to 45° . As a first step, the natural frequencies of a blade with varying sweep angles of 0° , 15° , 30° and 45° , and a hub length of 63.5mm were calculated. The numerical results obtained by the present work were compared with the experimental data and the one-dimensional beam analysis results as shown in Figs. 27 through 30. The present results are shown as continuous lines, and the experimental data and one-dimensional nonlinear beam analysis results are shown as triangle and circle symbols respectively. Figs. 27 through 30 show the effects of rotating speed and sweep angle upon the blade natural frequencies. It is clear that the frequencies of all modes (four flap, and one torsion) are increased constantly as the rotational speed increases due to the centrifugal stiffening effect. It can be seen that the natural frequencies obtained with the present analysis model compare well with the experimental data [63]. The maximum difference is within 5% for all flap and torsion modes. Also, the results show that the present predictions using three-dimensional solid-shell elements show good correlation with the one-dimensional beam analysis results those given by Kang et al. [18] who used the comprehensive rotorcraft analysis code RCAS [64]. They used 15 beam elements in the analysis model with 3

elements for the swept tip section, and each beam element has 15 degrees of freedom. Although the experimental data and analysis results upon the first lag mode were not given in references [18, 63], the second mode of the current analysis at 750rpm, which is observed to be a lag mode, has been included. A point to note is that the tip sweep can influence the natural frequencies of rotating blade. The flap bending frequencies show a slight decrease with increasing sweep angle. However, only the first torsion frequency is increased with respect to the sweep angle significantly. A possible reason for this behavior could be the extension-torsion coupling effect. Since the centrifugal force attempts to increase the torsional stiffness due to the trapeze effect, the frequency of the torsional mode increases. The trapeze effect is named because of the tendency of a trapeze, which, when twisted slightly, tends to restore itself to zero twist with a restoring moment.

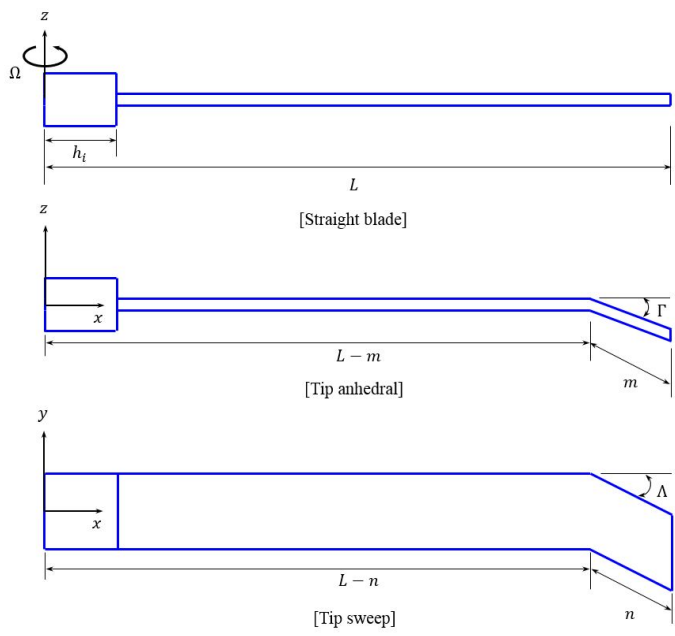


Fig. 26 Configuration of the beam-type blade with tip sweep and tip anhedral

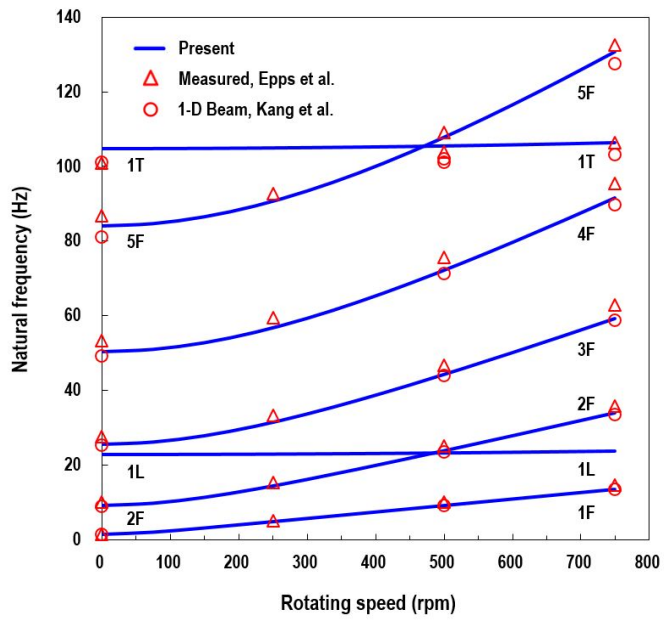


Fig. 27 Natural frequencies versus rotating speed (isotropic, $\Lambda=0^\circ$, AR=37.5)

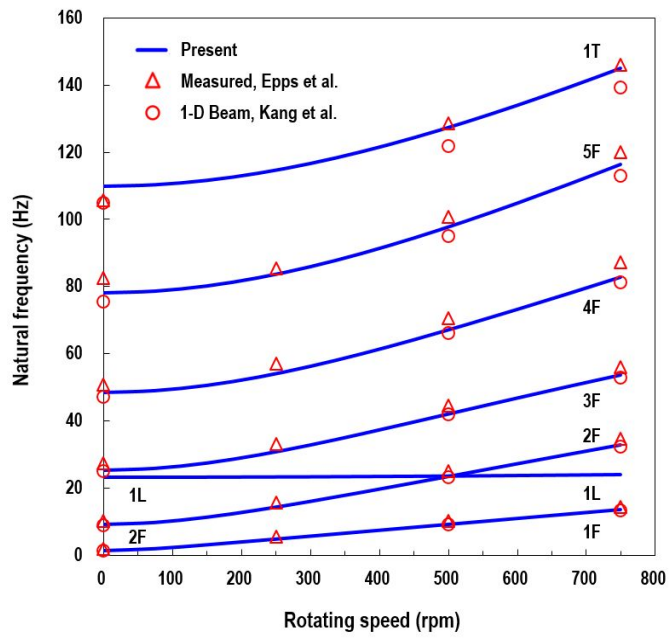


Fig. 28 Natural frequencies versus rotating speed (isotropic, $\Lambda=15^\circ$, AR=37.5)

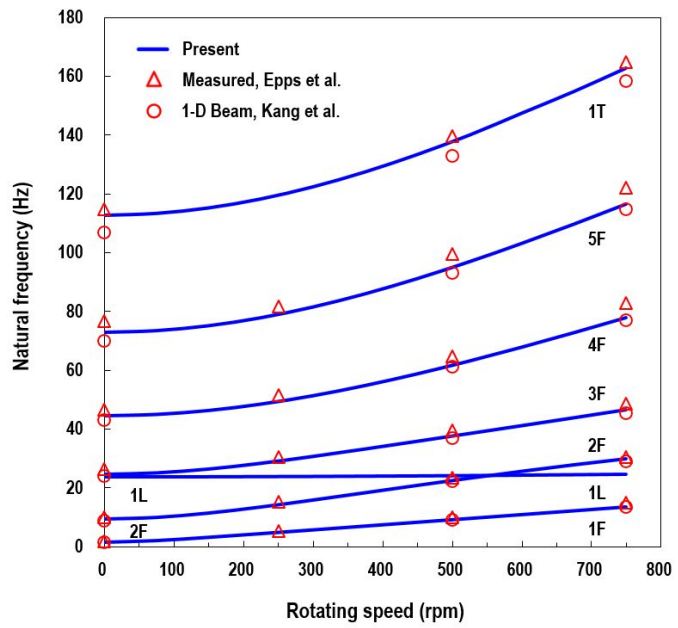


Fig. 29 Natural frequencies versus rotating speed (isotropic, $\Lambda=30^\circ$, AR=37.5)

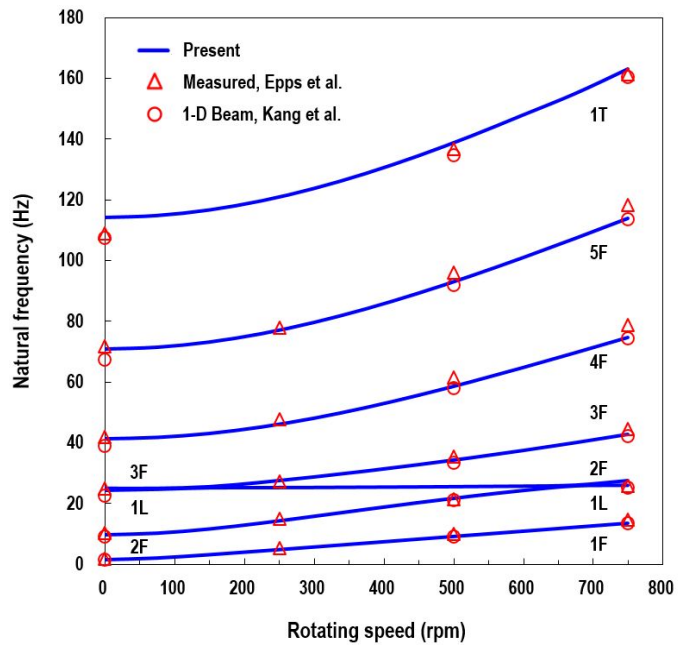


Fig. 30 Natural frequencies versus rotating speed (isotropic, $\Lambda=45^\circ$, AR=37.5)

In the second step, the total blade length of 317.5mm (AR=12.5, including the swept tip) and the hub length of 698.5mm were considered to investigate the effect of aspect ratio. Natural frequencies with respect to the rotating speeds and various tip sweep angles were calculated, and those results are presented Figs. 31 through 34.

Fig. 31 shows the natural frequencies of straight blade with respect to the rotating speed. For the straight blade, the present converged predictions are well comparable to the beam analysis results, and differences appear only first torsion and fourth flap bending modes. The maximum difference of the fourth flap bending mode is about 6% at the rotating speed of 750rpm. However, for the blade with a sweep angle of 45° as shown in Fig. 34, considerable differences was found in the third through sixth modes (third and fourth flap, first lag and first torsion). The maximum difference of 29% appears in the fourth flap bending mode. The results show that the one-dimensional nonlinear beam and three-dimensional solid-shell model are comparable for the only straight and large aspect ratio blade. Thus, it is possible that there is a limit of one-dimensional beam model to evaluate the elastic coupling effects corresponding to the large swept tips.

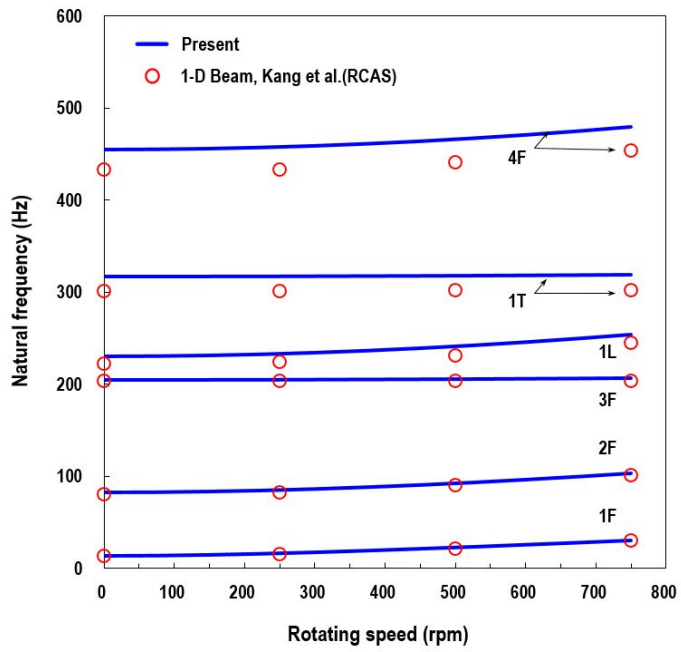


Fig. 31 Natural frequencies versus rotating speed (isotropic, $\Lambda=0^\circ$, AR=12.5)

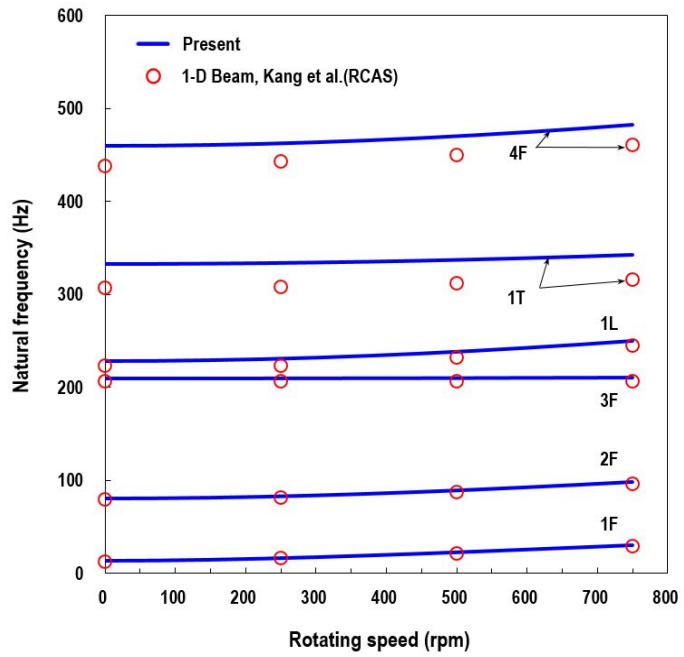


Fig. 32 Natural frequencies versus rotating speed (isotropic, $\Lambda=15^\circ$, AR=12.5)

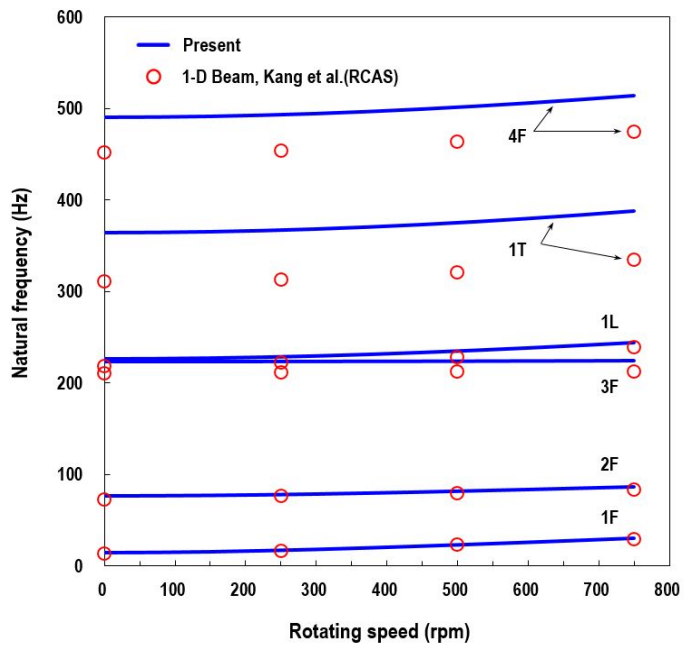


Fig. 33 Natural frequencies versus rotating speed (isotropic, $\Lambda=30^\circ$, AR=12.5)

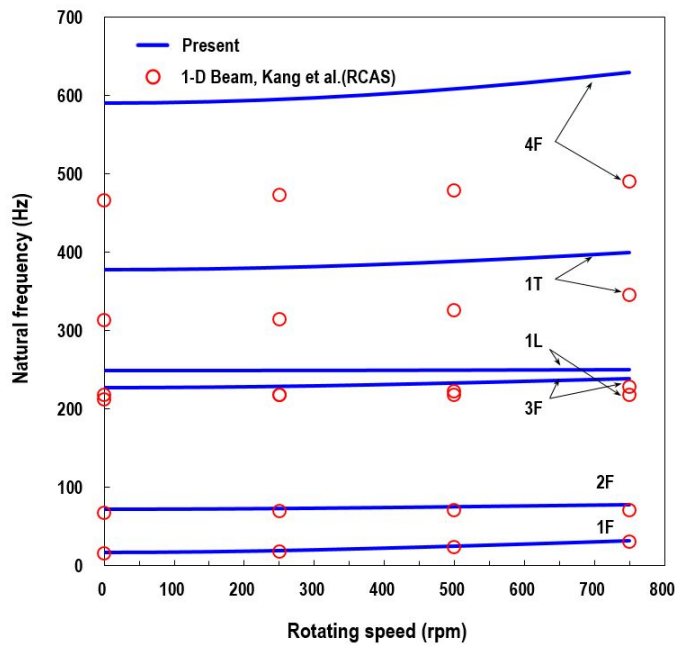


Fig. 34 Natural frequencies versus rotating speed (isotropic, $\Lambda=45^\circ$, AR=12.5)

6.1.2 Composite Blade Models

A composite beam model has the same dimensions of the isotropic beam model (AR=37.5), and the material properties used are listed in Table 6. Stacking angles, from $[0^\circ]_{24}$ through $[90^\circ]_{24}$, were considered. The resulting frequencies were compared with those by Epps and Chandra [63] and Hodges et al. [65]. The effect of the swept tip angles and rotating speed on the first five natural frequencies are presented in Figs. 35 through 38.

Figs. 35 and 36 show the comparison results of the $[0^\circ]_{24}$ lay-up beams with sweep angles of 0° and 45° , respectively. Although the experimental data and analysis results upon the first lag mode were not given in references [63, 65], the second mode of the current analysis at 750rpm, which is observed to be a lag mode, has been included. The natural frequencies of the current three-dimensional solid-shell model can capture the frequency-trend for all the first five modes. Similar to the isotropic cases, the sweep angle attempts to decrease the flap bending frequencies, but the torsion frequency increases with sweep angle.

Figs. 37 and 38 show the natural frequencies for the $[15^\circ]_{24}$ lay-up beams. The present prediction results show good agreement with the measured data. In fact, for the case of natural frequencies upon the second and third modes with swept tip angle of 45° , the present results are much closer to the experimental data than those obtained by the one-dimensional beam model. The maximum difference between the present

results and measured data is within 5% for all the flap and torsion modes.

Table 11. Material properties of the composite beam type blade

Property	Dimensions
E_{11}	$2.059 \times 10^7 \text{ lb/in}^2$
E_{22}, E_{33}	$1.42 \times 10^6 \text{ lb/in}^2$
G_{12}, G_{13}, G_{23}	$8.9 \times 10^5 \text{ lb/in}^2$
ν_{12}, ν_{13}	0.42
ν_{23}	0.54
ρ	$1.44 \times 10^{-4} \text{ lb-sec}^2/\text{in}^4$

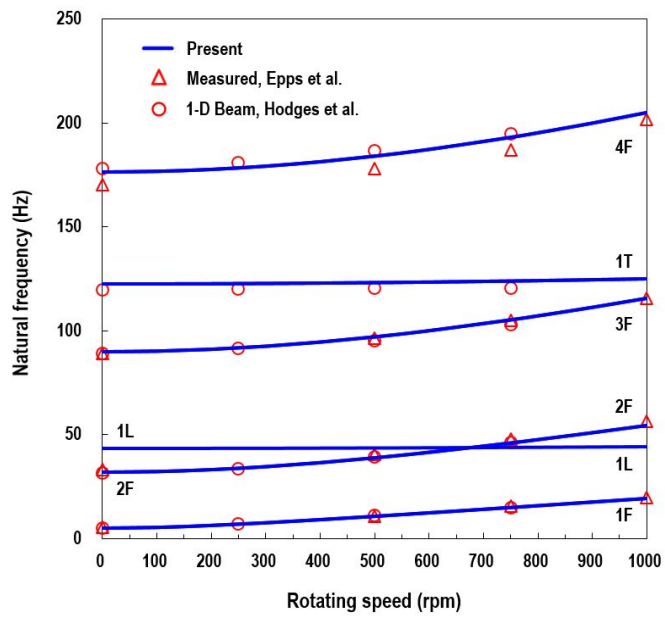


Fig. 35 Natural frequencies versus rotating speed (orthotropic, $[0^\circ]_{24}$,

$$\Lambda=0^\circ)$$

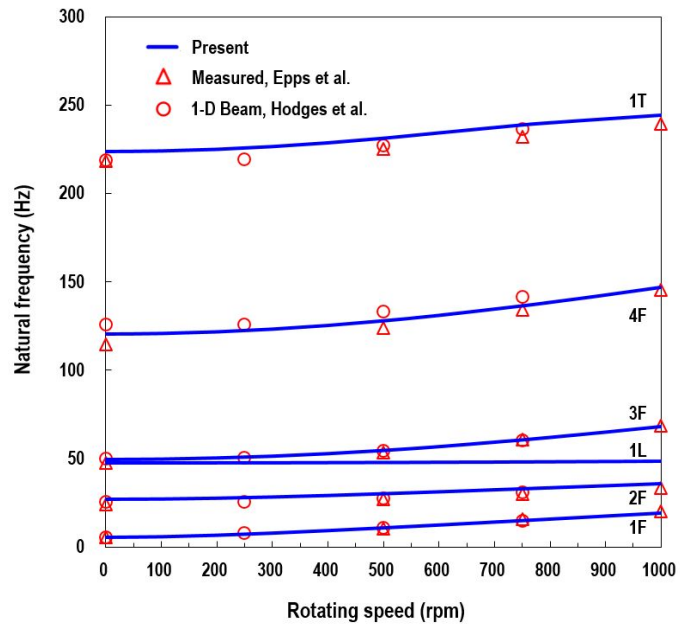


Fig. 36 Natural frequencies versus rotating speed (orthotropic, $[0^\circ]_{24}$, $\Lambda=45^\circ$)

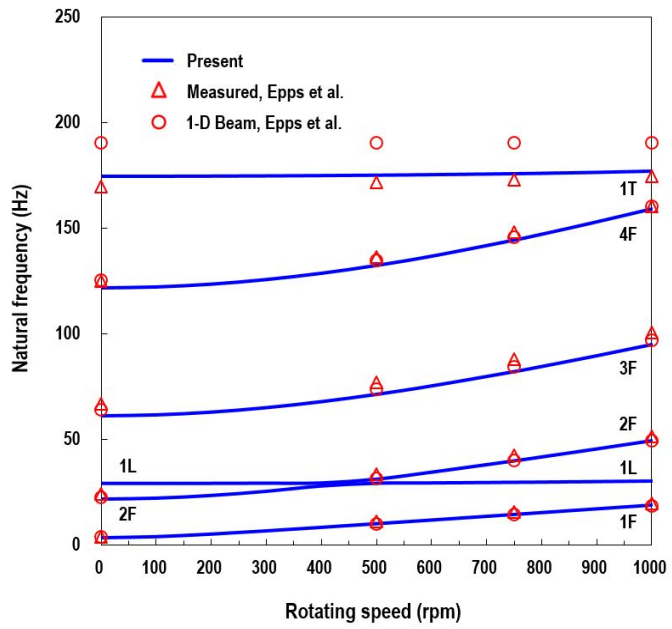


Fig. 37 Natural frequencies versus rotating speed (orthotropic, $[15^\circ]_{24}$, $\Lambda=0^\circ$)

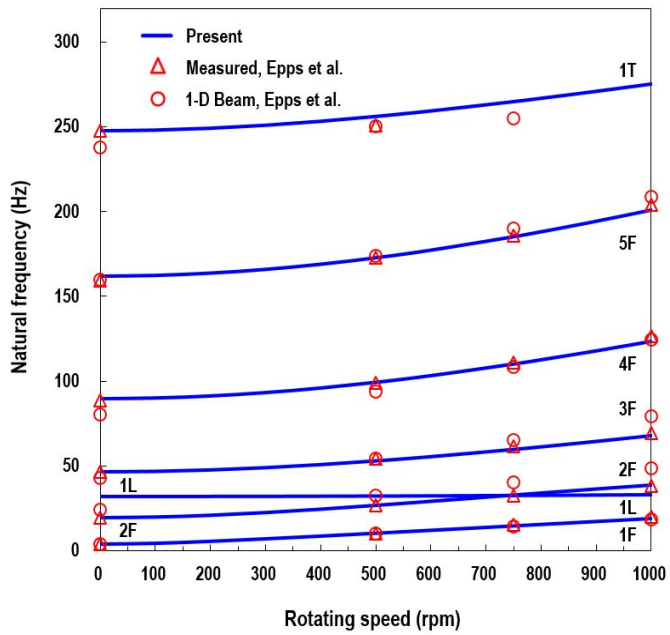


Fig. 38 Natural frequencies versus rotating speed (orthotropic, $[15^\circ]_{24}$, $\Lambda=45^\circ$)

The influence of fiber angle is investigated next by modeling

laminated blades of different lay-up construction. The evaluation of the dynamic behavior was performed on the composite beam type blades with the same length, width, and thickness.

As shown in Figs. 39 through 42, the natural frequencies of the first five modes (three flap, and one lag and torsion) as a function of ply angle, rotating speed and sweep angle are investigated. From the results, it is shown that all the flap and lag natural frequencies decrease, in general, as the fiber angle increases and reach asymptotic values around 60° stacking angle. On the contrary, the torsional frequency increases initially up to around 30° stacking angle, and then decreases gradually up to 90° . It is found that the maximum flap bending natural frequencies occur at 0° stacking angle. Also, the results indicate that the flap and lag frequencies are not very sensitive to the variations in the sweep angle. On the contrary, the first torsion frequency is increased significantly with respect to the sweep angle.

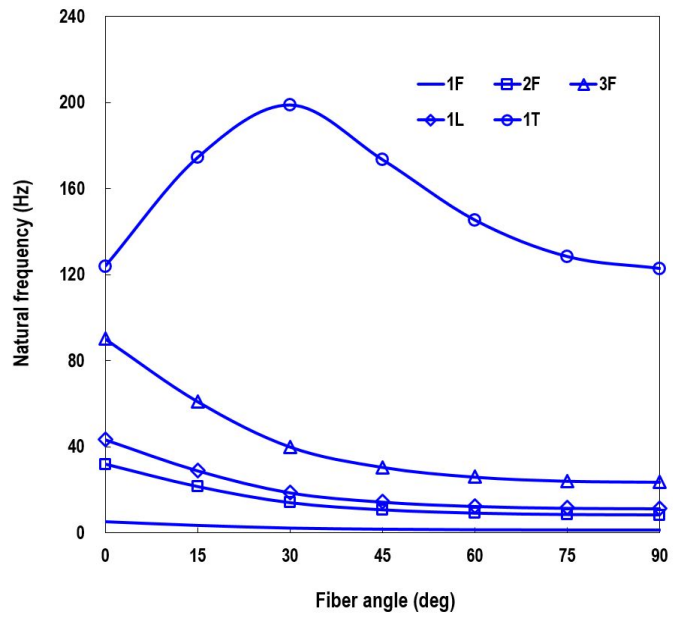


Fig. 39 Natural frequencies versus fiber angles ($\Lambda=0^\circ$, 0 rpm)

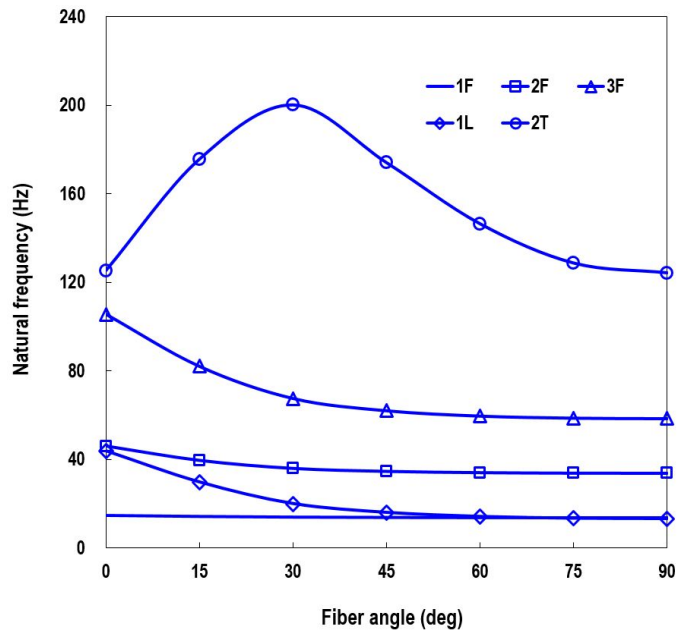


Fig. 40 Natural frequencies versus fiber angles ($\Lambda=0^\circ$, 750 rpm)

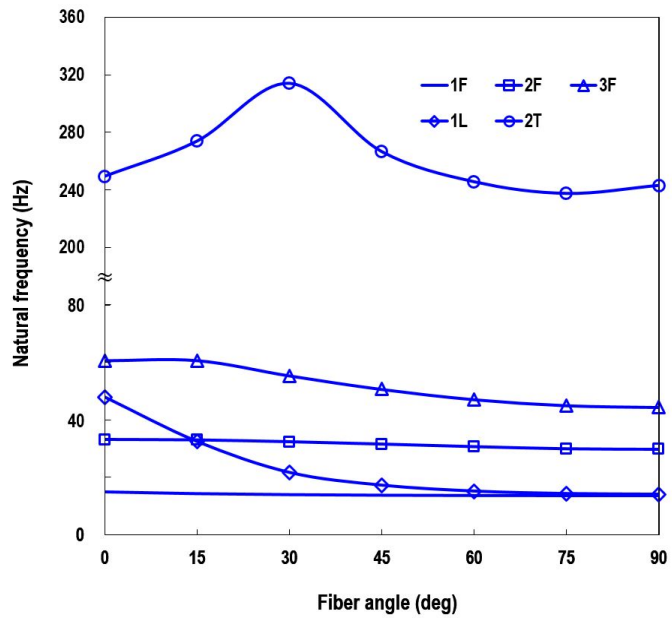


Fig. 41 Natural frequencies versus fiber angles ($\Lambda=45^\circ$, 0 rpm)

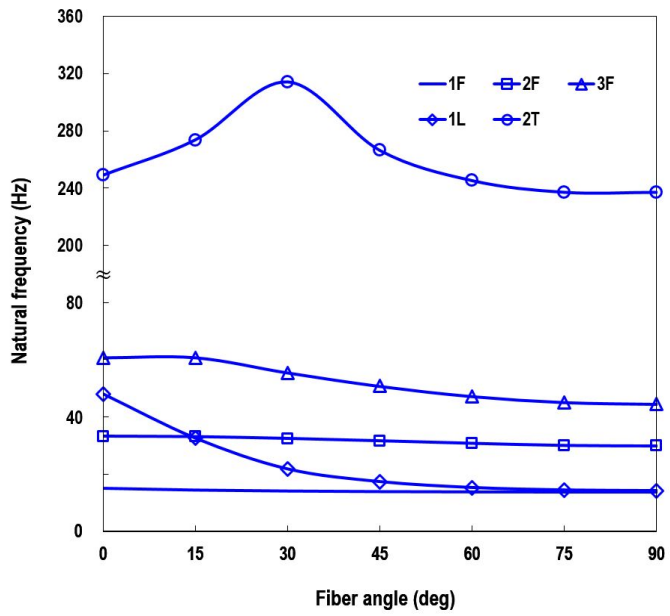


Fig. 42 Natural frequencies versus fiber angles ($\Lambda=45^\circ$, 750 rpm)

6.2 Effect of Tip Sweep Ratio

The influence of swept tip length on the natural frequencies is investigated. The blade model has the total length $L=1,016\text{mm}$ that includes hub lengths with $h_1=698.5\text{mm}$. The tip sweep ratio $\bar{n}=n/L$ varies up to 0.48 representing 48% of the blade. Also, the tip sweep angle Λ maintains 45° .

As shown in Fig. 43, the first flap bending frequency increases gradually with increase in the tip sweep ratio. For the second flap bending mode as shown in Fig. 44, an interesting phenomenon is observed that the frequency is increased first up to $\bar{n}=0.1$ or 0.2 , and then it shows a downward trend as the tip sweep ratio increases.

Fig. 45 shows the effect of the tip sweep ratio on the first lead-lag mode natural frequencies. As the tip sweep ratio increases, the frequency of the first lead-lag mode increases monotonically. However, the rotating speed does not have a significant impact on the first lead-lag bending mode frequencies. The difference between the natural frequencies of the nonrotating and rotating blades is less than 1%.

Fig. 46 shows the influence of the tip sweep ratio and rotating speed on the first torsional mode. It is similar to the second flap bending mode in that its frequency is increased up to $\bar{n}=0.2$, and then it shows a downward trend as the tip sweep ratio increases. Moreover, the difference between the frequencies of the nonrotating and rotating blades is increased in terms of the rotating speed due to the centrifugal

stiffening effect.

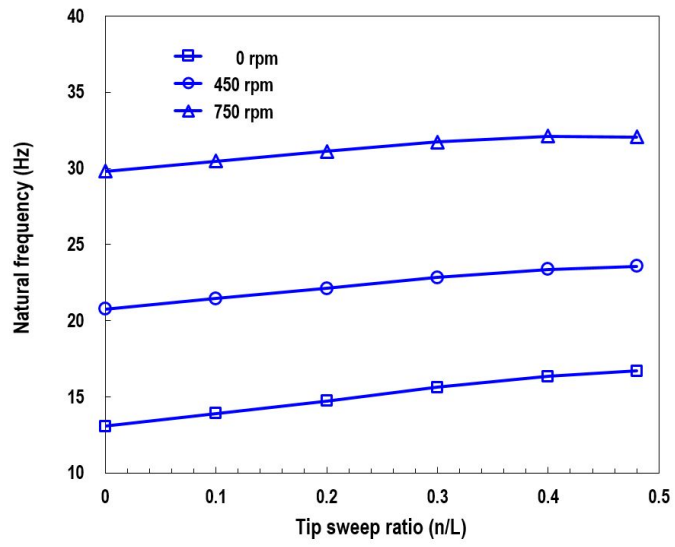


Fig. 43 Influence of the swept tip ratio on the natural frequencies: the first flap bending mode

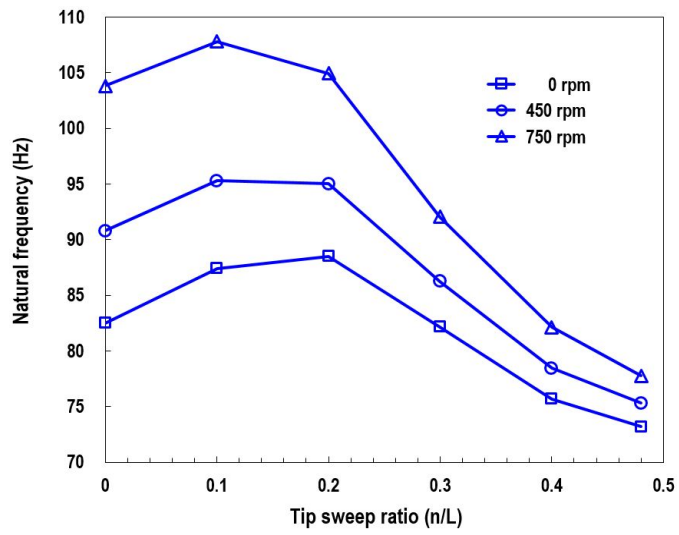


Fig. 44 Influence of the swept tip ratio on the natural frequencies: the second flap bending mode

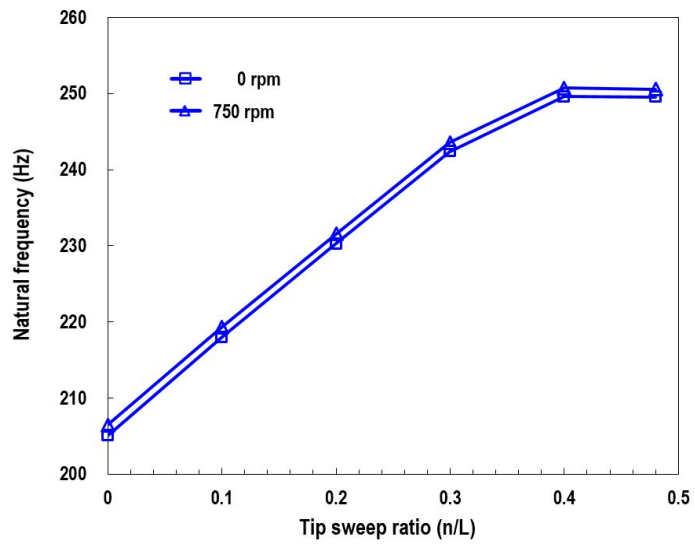


Fig. 45 Influence of the swept tip ratio on the natural frequencies: the first lag bending mode

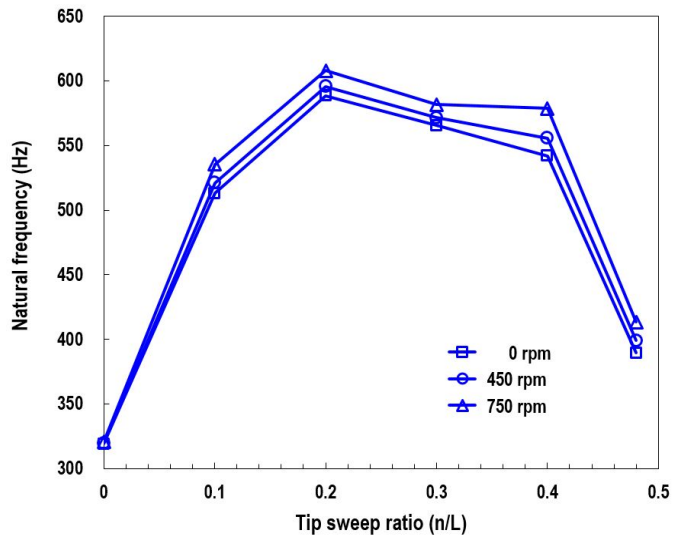


Fig. 46 Influence of the swept tip ratio on the natural frequencies: the first torsion mode

6.3 Effect of Tip Anhedral

The geometry and boundary conditions for this problem are the same as for the previous Section 6.1.1. The blade model has the anhedral length $m=152.5\text{mm}$, representing 15% of the blade. Using the same mesh configuration as for the isotropic beam model as before, the influence of tip anhedral which varies from 0° to 45° on the natural frequencies was investigated. Figs. 47 through 50 show the influence of tip anhedral on the flap, lag and torsion frequencies, respectively. It is clear that the frequencies of all the modes (two flap, and one lag and torsion) are increased constantly as the rotational speed increases due to the centrifugal stiffening effect. As shown in Figs. 47 and 48, the first and second flap bending frequencies are maintained at the almost same level with respect to the tip anhedral. Therefore, the tip anhedral does not significantly influence the flap bending frequencies of the blade. From Fig. 49, the first lag frequencies increase slightly with tip anhedral. On the contrary, the non-rotating lag frequency shows a decrease with increasing anhedral angle. A possible reason for this behavior is that the lag bending and extension coupling leads to an increase in the lag stiffness. From the investigation of Fig. 50, the first torsional frequency decreases with variation in tip anhedral. Similar to the swept tip blade, the torsion frequencies are sensitive to the tip anhedral.

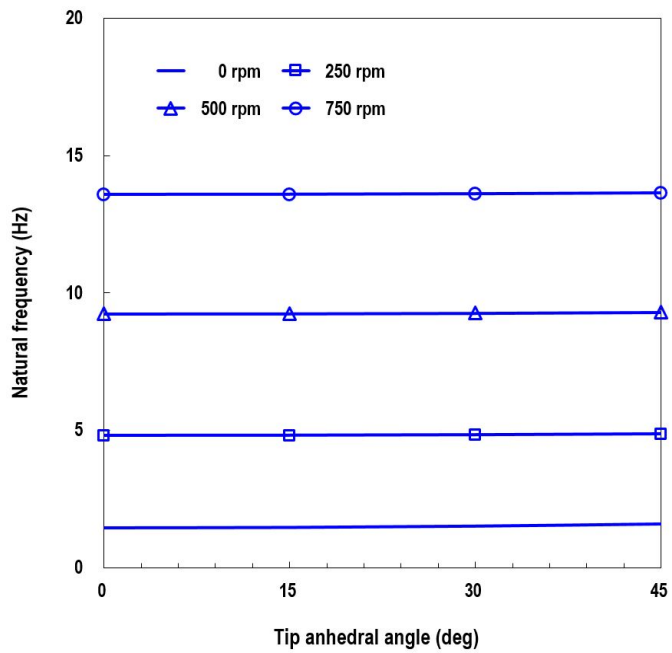


Fig. 47 Influence of the tip anhedral on the natural frequencies: the first flap bending mode

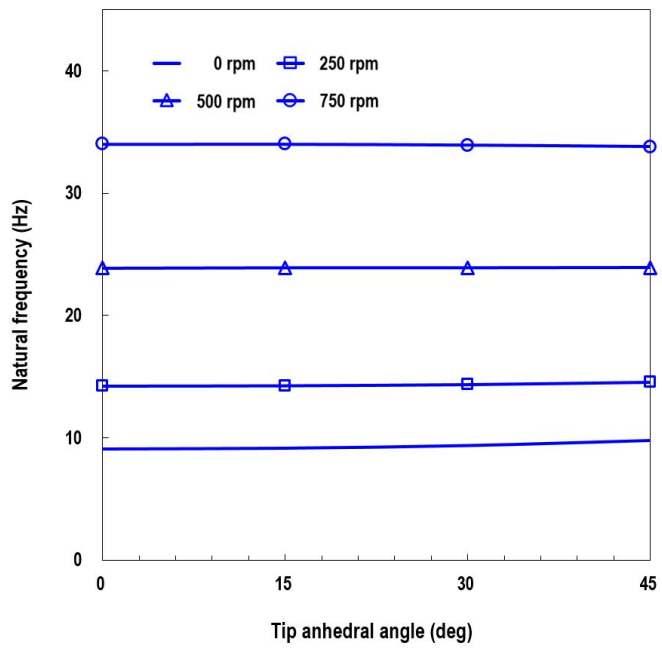


Fig. 48 Influence of the tip anhedral on the natural frequencies: the second flap bending mode

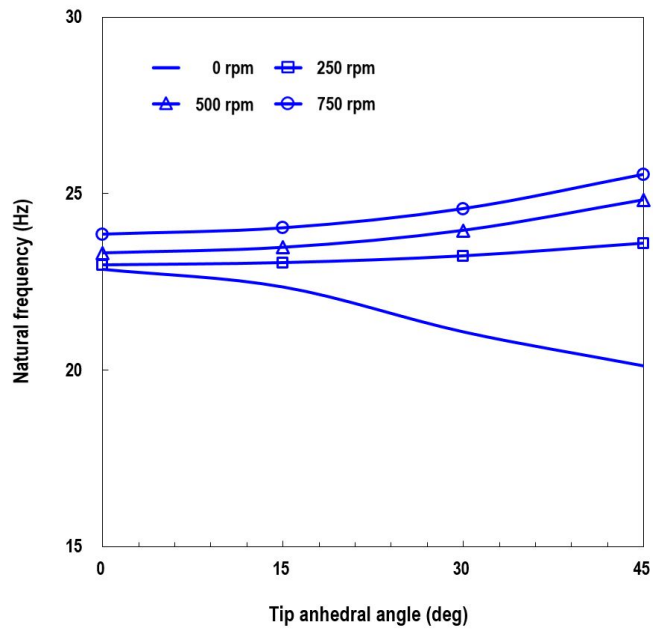


Fig. 49 Influence of the tip anhedral on the natural frequencies: the first lag bending mode

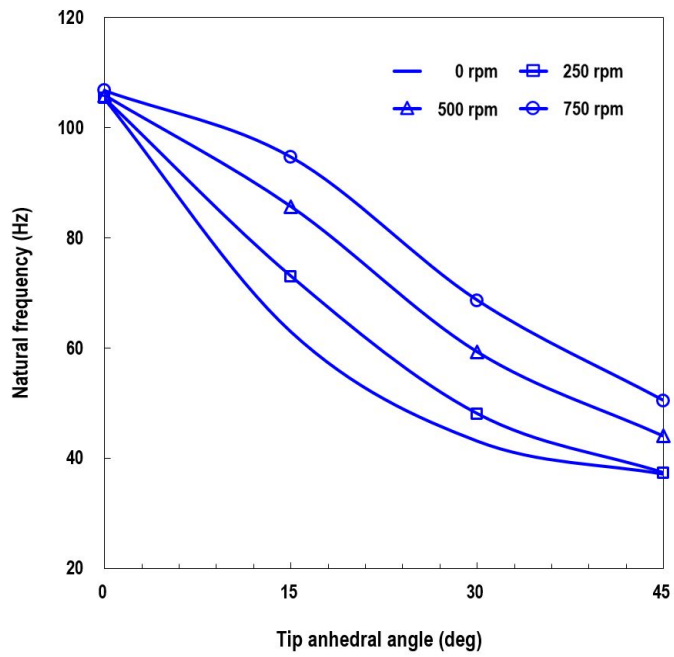


Fig. 50 Influence of the tip anhedral on the natural frequencies: the first torsion mode

Chapter 7. Conclusions

7.1 Summary

The rotating composite blades were modeled by eighteen-node solid-shell finite element. The present analytical model includes the effects of transverse shear deformation, Coriolis effect and elastic couplings due to the anisotropic material behavior. Since the present solid-shell element was formulated based on the three-dimensional continuum mechanics, the out of plane warping was included in the analysis model without complicated assumptions for specific beam, plate or shell theories. The incremental total Lagrangian approach was adopted to allow estimation on arbitrarily large rotations and displacements. The nonlinear equations of motion for the finite element model were derived using Hamilton's principle, and the resulting nonlinear equilibrium equations were solved by Newton-Raphson method combined with the load control. A modified stress-strain relation was used to avoid the transverse shear locking problem, and fairly reliable results were obtained with no sign of the locking phenomenon. In order to reduce the computational complexity of the problem, the static (or Guyan) reduction and IRS reduction method were adopted. Those model reduction methods gave not only reliable solutions, but also less computational effort for any geometric configurations and boundary conditions.

The present finite element formulations and solution procedures were applied for the static and dynamic analysis of beam, plate and shell structures. To validate the accuracy and reliability, numerical results obtained by the present thesis were compared to several benchmark problems. The present prediction results show a good correlation with the experimental data and other finite element analysis results.

In this thesis, the vibration characteristics of shell and beam type blades were investigated. For the case of shell type blades, the influences of geometric nonlinearity and the design parameters, namely blade curvatures and pretwist are investigated. Also, the effects of design parameters, such as tip sweep, anhedral, aspect ratio and composite ply orientation on the natural frequencies of beam type blades were investigated.

The shell type blades were modeled as an open cylindrical shell with the square planform and initial twist. From the present study of vibration characteristics of the shell type blades, the main conclusions are summarized below:

- a) The blade curvatures and geometric nonlinearity may significantly influence dynamic characteristics of the shell type blades.
- b) For the case of the shallow shell type blade model, the effect of rotation was to increase frequencies of all the modes due to the centrifugal stiffening effect. Compared with the linear analysis results, the rotational effect was found to be different in the certain modes when including the geometric nonlinear terms. The

maximum difference of the chordwise bending frequency between the nonlinear and linear analysis result is about 7 %. The reason for this is that the chordwise bending stiffness is decreased because the centrifugal force attempts to flatten the blade in chordwise direction. Such decrease in the chordwise bending stiffness enforces the natural frequencies to become smaller than the corresponding linear frequencies.

- c) For the deep shell type blade model, the maximum difference of the chordwise bending frequency between the nonlinear and linear analysis result is approximately 26%. Since the centrifugal force affects the flap bending and chordwise bending stiffness of the blade, the second and third frequency approach each other quite closely as the rotating speed increases. However, frequency crossing does not occur, and the second and third mode frequency loci are changed abruptly. The linear analysis results did not capture these frequency deep drops and abrupt frequency loci veering phenomena.
- d) The fundamental frequency shows monotonic decrease as the twist angle increases. The first vibration mode is the first torsion mode. Therefore, this phenomenon implies that an increase in the twist angle leads to a reduction in the torsional stiffness. However, the non-dimensional frequencies of the other modes show a downward or upward trend as the rotating speed increases. A possible reason for this behavior is that the coupled bending-

torsion frequency can increase or decrease with variation in rotating speed of the blade depending on the relative increments in the blade stiffness.

The influence of tip sweep and anhedral on the natural frequencies of beam type blades was investigated. From the study of vibration characteristics of the beam type blades, the main conclusions are summarized below:

- a) The one-dimensional beam and three-dimensional solid model are comparable for the straight and large aspect ratio of 37.5. As decreasing in the blade aspect ratio of 12.5, considerable differences appear in the flap bending and torsion modes. The maximum difference of 29% appears in the fourth flap mode with 45° tip sweep.
- b) Since the rotor blades with the swept tip experience bending-torsion couplings, the sweep angle attempts to decrease the flap bending frequencies, but the torsion frequency increases with the sweep angle. The present results are much closer to the experimental data than those obtained by the one-dimensional beam model.
- c) In general, all the flap and lag natural frequencies decrease as the fiber angle increases and reach asymptotic values around 60° stacking angle. On the contrary, the torsional frequency increases initially up to around 30° stacking angle, and then decreases

gradually up to 90° .

- d) The flap bending frequencies are maintained at the almost same level with respect to the tip anhedral. However, the first lag frequency increases slightly with the tip anhedral. The torsional frequency decreases with variation in the tip anhedral of the blade. Similar to the swept tip blade, the torsion frequencies are sensitive to the tip anhedral.

7.2 Future Works

The present thesis has demonstrated that the proposed finite element formulation and solution procedures can be considered as a valuable tool for a structural dynamic analysis of laminated rotating composite blades undergoing large rotations and displacements. However, there is still much work that need to be pursued in this area. The following is future works that may be identified as interesting and profitable.

- a) Development of the procedures for predicting composite damage like matrix cracking, fiber failure and delamination.
- b) Consideration of the aerodynamics forces to investigate the aeroelastic stability.
- c) Extension of the analysis to account for the internal structural layout of rotorcraft blades such as skin, spar and foam cores.
- d) Application of the assumed natural strain approach to avoid the locking problems and improve the convergence behavior.

References

- [1] R. Southwell, F. Gough, “The Free Transverse Vibration of Airscrew Blade”, British A.R.C. Reports and Memoranda, Vol.766, 1921
- [2] W. Carnegie, “Vibration of Pretwisted Cantilever Blading Allowing for Rotary Inertia and Shear Deflection”, Journal of Mechanical Engineering Science, Vol.6 (2), 1964, 105–109
- [3] B. Dawson, “The Orthogonality Condition of Natural Modes of Pretwisted Cantilever Blading”, Bulletin of Mechanical Engineering Education, Vol.6, 1967, 345–355
- [4] S. Putter, H. Monor, “Natural Frequencies of Radial Rotating Beams”, Journal of Sound and Vibration, Vol.56 (2), 1978, 175–185
- [5] K. R.V. Kaza, R. E. Kielb, “Effects of Warping and Pretwist on Torsional Vibration of Rotating Beams”, ASME Journal of Applied Mechanics, Vol.51 (4), 1984, 913-920
- [6] K. A. Ansari, “On the Importance of Shear Deformation, Rotatory Inertia, and Coriolis forces in Turbine Blade Vibration”, Journal of Engineering for Gas Turbine and Power, Vol.108 (2), 1986, 319-324
- [7] H. H. Yoo, J. Chung, “Vibration Analysis of Rotating Pretwisted Blades”, Computers and Structures, Vol.79, 2001, 1811-1819

- [8] H. H. Yoo, J. M. Kim, J. Chung, "Equilibrium and Modal Analyses of Rotating Multibeam Structures Employing Multiple Reference Frames", *Journal of Sound and Vibration*, Vol.302, 2007, 789-805
- [9] L.W. Rehfield, "Design Analysis Methodology for Composite Rotor Blades", *Proceedings of the Seventh DOD/NASA Conference on Fibrous Composites in Structural Design*, AFWAL-TR-85-3094, 1985, 1-15
- [10] R. Chandra, I. Chopra, "Experimental-Theoretical Investigation of the Vibration Characteristics of Rotating Composite Box Beams, *Journal of Aircraft*, Vol.29 (4), 1992, 657-664
- [11] E. C. Smith, I. Chopra, "Aeroelastic Response, Loads, and Stability of a Composite Rotor in Forward Flight", *AIAA Journal*, Vol.31 (7), 1993, 1265-1273
- [12] S. N. Jung, V. T. Nagaraj, I. Chopra, "Refined Structural Dynamics Model for Composite Rotor Blades", *AIAA Journal*, Vol.39 (2), 2001, 339-348
- [13] C. E. S. Cesnik, D. H. Hodges, "VABS: A New Concept for Composite Rotor Blade Cross-sectional Modeling", *Journal of the American Helicopter Society*, Vol. 42 (1), 1997, 27-38
- [14] D. H. Hodges, *Nonlinear Composite Beam Theory*, AIAA, Reston, Virgiana, 2006
- [15] A.W. Leissa, M.S. Ewing, "Comparison of Beam and Shell Theories for the Vibrations of Thin Turbomachinery Blades", *Journal of Engineering for Power*, Vol.105 (2), 1983, 383-392

- [16] Anubhav Datta, Wayne Johnson, "Three-dimensional Finite Element Formulation and Scalable Domain Decomposition for High Fidelity Rotor Dynamic Analysis", Proceedings of the 65th AHS Forum, 2009
- [17] H. Yeo, K. V. Truong, R. A. Ormiston, "Assessment of 1-D Versus 3-D Methods for Modeling Rotor Blade Structural Dynamics", Proceedings of the 18th AIAA/ASME/ASCE/AHS/ASC Structures, Structural Dynamics, and Material Conference, 2010
- [18] H. Kang, C. Chang, H. Saberi, R. A. Ormiston, "Assessment of Beam and Shell Elements for Modeling Rotorcraft Blades", American Helicopter Society 68th Annual Forum, 2012
- [19] S. Heo, O. A. Bauchau, "A Novel Parallel Algorithm for Rotor Dynamics Simulation", 70th AHS Forum, Montreal, Canada, 2014
- [20] M. Dokainish, S. Rawtani, "Vibration Analysis of Rotating Cantilever Plates", Journal for Numerical Methods in Engineering, Vol.3 (2), 1971, 233-248
- [21] V. Ramamurti, R. Kielb, "Natural Frequencies of Twisted Rotating Plates", Journal of Sound and Vibration, Vol.97 (3), 1984, 429-449
- [22] J. T. S. Wang, D. Shaw, O. Mahrenholtz, "Vibration of Rotating Rectangular Plates," Journal of Sound and Vibration", Vol.112 (3), 1987, 455-468
- [23] D. Shaw, K. Y. Shen, J. T. Wang, "Flexural Vibration of Rotating Rectangular Plates of Variable Thickness", Journal of Sound and Vibration, Vol.126 (3), 1988, 373-385.

- [24] R. Bhumbra, J.B. Kosmatka, “Behavior of Spinning Pretwisted Composite Plates Using a Nonlinear Finite Element Approach”, *AIAA Journal*, Vol.34 (8), 1996, 1686-1695
- [25] H. H. Yoo, C. Pierre, “Modal Characteristics of a Rotating Rectangular Cantilever Plate”, *Journal of Sound and Vibration*, Vol.259 (1), 2003, 81–96
- [26] B.E. Greene, D. R. Strome, R.C. Weikel, “Application of the Stiffness Method to the Analysis of Shell Structures”, *Proceedings of Aviation Conference of ASME*, 1961
- [27] T. J. R. Hughes, F. Frezzi, “On Drilling Degrees of Freedom”, *Computer Methods in Applied Mechanics and Engineering*, Vol.72 (1), 1989, 105-121
- [28] A. Ibranhimbegovic, R. L. Taylor, E. L. Wilson, “A Robust Quadrilateral Membrane Finite-Element with Drilling Degrees of Freedom”, *International Journal for Numerical Methods in Engineering*, Vol.30 (3), 1990, 445-457
- [29] J. L. Batoz, M. Benthahar, “Evaluation of a New Quadrilateral Thin Plate Bending Element” *International Journal for Numerical Methods in Engineering*, Vol.18 (11), 1982, 1655-1677
- [30] O. C. Zienkiewicz, E. Hinton, “Reduced Integration, Function Smoothing and Non-Conformity in Finite-Element Analysis (with Special Reference to Thick Plates)”, *Journal of the Franklin Institute-Engineering and Applied Mathematics*, Vol.302 (5), 1976, 443-461

- [31] K. J. Bathe, E. N. Dvorkin, "A 4-Node Plate Bending Element Based on Mindlin Reissner Plate-Theory and a Mixed Interpolation", *International Journal for Numerical Methods in Engineering*, Vol.21 (2), 1985, 367-383
- [32] E. Hinton, H. C. Huang, "A Family of Quadrilateral Mindlin Plate Elements with Substitute Shear Stain Fields", *Computers & Structures*, Vol.23 (3), 1986, 409-431
- [33] T. Belytschko, L. P. Bindeman, "Assumed Strain Stabilization of the 8 Node Hexahedral Element", *Computer Methods in Applied Mechanics and Engineering*, Vol.105 (2), 1993, 225-260
- [34] H. T. Y. Yang, S. Saigal, D. G. Liaw, "Advances of Thin Shell Finite-Elements and Some Applications", *Computers & Structures*, Vol. 35 (4), 1990, 481-504
- [35] J. J. Conner, C. A. Brebbia, "A Stiffness Matrix for a Shallow Rectangular Shell Element", *Journal of Engineering Mechanics Division, ASCE*, Vol.93, 1976, 43-65
- [36] K. S. Surana, "Geometrically Non-Linear Formulation for the Curved Shell Elements", *International Journal for Numerical Methods in Engineering*, Vol.19 (4), 1983, 581-615
- [37] Z. X. Li, L. Vu-Quoc, "An Efficient Co-rotational Formulation for Curved Triangular Shell Element", *International Journal for Numerical Methods in Engineering*, Vol.72 (9), 2007, 1029-1062

- [38] A. W. Leissa, J. K. Lee, A. J. Wang, “Rotating Blade Vibration Analysis Using Shells”, *Journal of Engineering for Power*, Vol.104, 1982, 296-302
- [39] M. S. Qatu, A. W. Leissa, “Vibration Studies for Laminated Composite Twisted Cantilever Plates”, *International Journal of Mechanical Science*, Vol.33 (11), 1991, 927-940
- [40] X. X. Hu, T. Sakiyama, H. Matsuda, C. Morita, “Fundamental Vibration of Rotating Cantilever Blades with Pre-twist”, *Journal of Sound and Vibration*, Vol.271 (1), 2004, 47–66
- [41] S. Ahmad, I. B. M. Irons, O. C. Zienkiewicz, “Analysis of Thick and Thin Shell Structures by Curved Finite Elements”, *International Journal of Numerical Method in Engineering*, Vol.2 (3), 1970, 419-451
- [42] E. Ramm, A plate/shell element for large deflections and rotations, In: Bathe et al.(ed), *Formulations and computational algorithms in finite element analysis*, 1977, MIT Press, Cambridge
- [43] K. J. Bathe, S. Bolourchi, “A Geometric and Material Nonlinear Plate and Shell Element”, *Computers and Structures*, Vol.11, 1980, 23–48
- [44] S. J. Lee, S. E. Han, “Free Vibration Analysis of Plates and Shells with a Nine-node Assumed natural Degenerated Shell Element”, *Journal of Sound and Vibration*, Vol.241 (4), 2001, 605-633
- [45] Y. J. Kee, J. H. Kim, “Vibration Characteristics of Initially Twisted Rotating Shell Type Composite Blades”, *Composite Structures*,

Vol.64 (2), 2004, 151-159

- [46] M. A. Crisfield, Finite Elements and Solution Procedures for Structural Analysis, Pineridge Press: Swansea, UK, 1986
- [47] T. J. R. Hughes, The Finite Element Method, Prentice-Hall: Englewood Cliffs, NJ, 1987
- [48] M. F. Ausserer, S. W. Lee, "An Eighteen-Node Solid Element for Thin Shell Analysis", International Journal for Numerical Methods in Engineering, Vol.26, 1988, 1345-1364
- [49] Y. H. Kim, S. W. Lee, "A Solid Element Formulation for Large Deflection Analysis of Composite Shell Structures", Computers & Structures, Vol.30 (1/2), 1988, 269-274
- [50] R. Hauptmann, K. Schweizerhof, "A Systematic Development of 'Solid-Shell' Element Formulations for Linear and Non-linear Analyses Employing only Displacement Degrees of Freedom", International Journal for Numerical Methods in Engineering, Vol.42, 1998, 49-69
- [51] K. Y. Sze, S. J. Zheng, "A Stabilized Hybrid-Stress Solid Element for Geometrically Nonlinear Homogeneous and Laminated Shell Analyses, Computational Methods in Applied Mechanical Engineering, Vol.191, 2002, 1945-1966
- [52] S. Klinkel, F. Gruttmann, W. Wagner, "A Robust Non-linear Solid-shell Element Based on a Mixed Variational Formulation", Computer Methods in Applied Mechanics and Engineering, Vol.195, 2006,

- [53] L. Vu-Quoc, X. G. Tan, "Optimal solid shells for nonlinear analyses of multilayer composites, II. Dynamic", *Computer Methods in Applied Mechanics and Engineering*, Vol.192 (9), 2003, 1017-1059
- [54] K. Rah, W. V. Paepegem, A. M. Habraken, J. Degrieck, "A Partial Hybrid Stress Solid-shell Element for the analysis of laminated composites", *Comput. Methods. Appl. Mech. Engrg.*, Vol.200, 2011, 3526-3539
- [55] R. J. Guyan, "Reduction of Stiffness and Mass Matrices", *AIAA Journal*, Vol.3 (2), 1965, 380
- [56] J. O'callahan, "A Procedure for an Improved Reduced System (IRS) Model", *Proceedings of the 7th International Modal analysis Conference*, January 1989, 17-21
- [57] K. Y. Sze, X. H. Liu, S. H. Lo, "Popular Benchmark Problems for Geometric Nonlinear Analysis of Shells", *Finite Elements in Analysis and Design*, Vol.40, 2004, 1551-1569
- [58] R. A. Arciniega, J. N. Reddy, "Tensor-based Finite Element Formulation for Geometrically Nonlinear Analysis of Shell Structures", *Computer methods in applied mechanics and engineering*, Vol.196, 2007, 1048-1073
- [59] S. K. Sinha, K. E. Turner, "Natural Frequencies of a Pre-twisted blade in a Centrifugal Force Field", *Journal of Sound and Vibration*,

Vol.330, 2011, 2655-2681

- [60] A. W. Leissa, "On a Curve Veering Aberration", Journal of Applied Mathematics and Physics, Vol.25, 1974, 99-111
- [61] N. Perkins, C. Mote, Comment on Curve Veering in Eigenvalue Problems, Journal of Sound and Vibration, Vol.106(3), 1986, 451-463
- [62] A. Brocklehurst, G. N. Barakos, "A Review of Helicopter Rotor Blade Tip Shapes", Progress in Aerospace Sciences, Vol. 56(1), 2013, 35-74
- [63] J. J. Epps, R. Chandra, Experimental-theoretical study of the effects of tip sweep on the natural frequencies of rotating composite blades, Proceedings of the 35th AIAA Structures, Structural Dynamics and Materials Conference, 1994
- [64] A. S. Hopkins, R. A. Ormiston, "An examination of Selected Problems in Rotor Blade Structural Mechanics and Dynamics", Proceedings of the 59th AHS Forum, 2003
- [65] D. H. Hodges, X. Shang, C. E. S. Cesnik, Finite element solution of nonlinear intrinsic equations for curved composite beams, Journal of American Helicopter Society, Vol.41(4), 1996, 313-321

Appendix A

This section is devoted to a description of the constitutive relations and transformations with focus on the orthotropic materials. A composite structure, in this case a laminate, is made up of orthotropic layers in certain stacking sequence. To determine the mechanical response of a composite, the behavior of a single orthotropic ply should be identified.

For an orthotropic ply it is assumed that the fibers are uniformly distributed whereby the constitutive relations may be simplified. Thus it is assumed that the properties of each ply may be regarded as homogeneous at the macroscopic level despite the inherently inhomogeneous nature of a composite. When performing analysis by displacement based finite elements a way to relate stresses to the determined displacement and thus strains is needed. By applying the assumption of linear elastic material behavior the constitutive law, known as Hooke's generalized law provides the following relation.

$$\boldsymbol{\varepsilon} = \bar{\mathbf{P}}\boldsymbol{\sigma} \quad (\text{A1})$$

Here the strains $\boldsymbol{\varepsilon}$ are related to stresses $\boldsymbol{\sigma}$ in a linear manner through the compliance matrix $\bar{\mathbf{P}}$. The compliance matrix $\bar{\mathbf{P}}$ is given by

$$\bar{\mathbf{P}} = \begin{bmatrix} 1/E_1 & -\nu_{12}/E_1 & 0 & 0 & 0 & 0 \\ & 1/E_2 & 0 & 0 & 0 & 0 \\ & & 1/E_3 & 0 & 0 & 0 \\ & & & 1/G_{12} & 0 & 0 \\ & & & & 1/G_{23} & 0 \\ \text{sym} & & & & & 1/G_{13} \end{bmatrix} \quad (\text{A2})$$

In Section 3.1, three Cartesian coordinate systems were defined, namely the global, local and principal material coordinate system. These coordinate systems were introduced to simplify the constitutive description. The transformations between the different coordinate systems are provided through transformation matrices. The transformation of constitutive properties from the local coordinate system to the global Cartesian coordinate system is achieved by the transformation matrix \mathbf{T}_G as follows.

$$\mathbf{T}_G = \begin{bmatrix} \mathbf{T}_{G1} & \mathbf{T}_{G2} \\ \mathbf{T}_{G3} & \mathbf{T}_{G4} \end{bmatrix}$$

$$\mathbf{T}_{G1} = \begin{bmatrix} a_{11}^2 & a_{21}^2 & a_{31}^2 \\ a_{12}^2 & a_{22}^2 & a_{32}^2 \\ a_{13}^2 & a_{23}^2 & a_{33}^2 \end{bmatrix}, \quad \mathbf{T}_{G2} = \begin{bmatrix} a_{11}a_{21} & a_{21}a_{31} & a_{31}a_{11} \\ a_{12}a_{22} & a_{22}a_{32} & a_{32}a_{12} \\ a_{13}a_{23} & a_{23}a_{33} & a_{33}a_{13} \end{bmatrix} \quad (\text{A3})$$

$$\mathbf{T}_{G3} = \begin{bmatrix} 2a_{11}a_{12} & 2a_{21}a_{22} & 2a_{31}a_{32} \\ 2a_{12}a_{13} & 2a_{22}a_{23} & 2a_{32}a_{33} \\ 2a_{13}a_{11} & 2a_{23}a_{21} & 2a_{33}a_{31} \end{bmatrix}$$

$$\mathbf{T}_{G4} = \begin{bmatrix} a_{11}a_{22} + a_{12}a_{21} & a_{21}a_{32} + a_{22}a_{31} & a_{31}a_{12} + a_{32}a_{11} \\ a_{12}a_{23} + a_{13}a_{22} & a_{22}a_{33} + a_{23}a_{32} & a_{32}a_{13} + a_{33}a_{12} \\ a_{13}a_{21} + a_{11}a_{23} & a_{23}a_{31} + a_{21}a_{33} & a_{33}a_{11} + a_{31}a_{13} \end{bmatrix}$$

Here the entries a_{ij} of the transformation matrix are given by direction cosines between the global coordinate system and the local coordinate system as shown in Section 3.1.2.

If the analysis is to be applied to an orthotropic material the constitutive properties are most naturally given in principal material directions that are not necessarily oriented in the same direction as the local coordinate system. The principal material directions are rotated with respect to the local coordinate system by an angle θ around the normal, z' , which constitutes a plane rotation. The transformation matrix between the local coordinate system and the principal material coordinate system is given by

$$\mathbf{T}_L = \begin{bmatrix} m^2 & n^2 & 0 & mn & 0 & 0 \\ n^2 & m^2 & 0 & -mn & 0 & 0 \\ 0 & 0 & 1 & 0 & 0 & 0 \\ -2mn & 2mn & 0 & m^2 - n^2 & 0 & 0 \\ 0 & 0 & 0 & 0 & m & -n \\ 0 & 0 & 0 & 0 & n & m \end{bmatrix} \quad (\text{A4})$$

Where the direction cosines for a plane rotation by use of trigonometric identities reduce to

$$m = \cos(\theta), \quad n = \sin(\theta) \quad (\text{A5})$$

Appendix B

The constant matrix \mathbf{L} , and the displacement gradient matrices \mathbf{A}_e and \mathbf{A}_η for the Green-Lagrange strain tensor are given by

$$\mathbf{L} = \begin{bmatrix} 1 & 0 & 0 & 0 & 0 & 0 & 0 & 0 & 0 \\ 0 & 0 & 0 & 0 & 1 & 0 & 0 & 0 & 0 \\ 0 & 0 & 0 & 0 & 0 & 0 & 0 & 0 & 1 \\ 0 & 1 & 0 & 1 & 0 & 0 & 0 & 0 & 0 \\ 0 & 0 & 0 & 0 & 0 & 1 & 0 & 1 & 0 \\ 0 & 0 & 1 & 0 & 0 & 0 & 1 & 0 & 0 \end{bmatrix} \quad (\text{B1})$$

\mathbf{A}_e

$$= \begin{bmatrix} \frac{1}{0}u_{,0x} & 0 & 0 & \frac{1}{0}v_{,0x} & 0 & 0 & \frac{1}{0}w_{,0x} & 0 & 0 \\ 0 & \frac{1}{0}u_{,0y} & 0 & 0 & \frac{1}{0}v_{,0y} & 0 & 0 & \frac{1}{0}w_{,0y} & 0 \\ 0 & 0 & \frac{1}{0}u_{,0z} & 0 & 0 & \frac{1}{0}v_{,0z} & 0 & 0 & \frac{1}{0}w_{,0z} \\ \frac{1}{0}u_{,0y} & \frac{1}{0}u_{,0x} & 0 & \frac{1}{0}v_{,0y} & \frac{1}{0}v_{,0x} & 0 & \frac{1}{0}w_{,0y} & \frac{1}{0}w_{,0x} & 0 \\ 0 & \frac{1}{0}u_{,0z} & \frac{1}{0}u_{,0y} & 0 & \frac{1}{0}v_{,0z} & \frac{1}{0}v_{,0y} & 0 & \frac{1}{0}w_{,0z} & \frac{1}{0}w_{,0y} \\ \frac{1}{0}u_{,0z} & 0 & \frac{1}{0}u_{,0x} & \frac{1}{0}v_{,0z} & 0 & \frac{1}{0}v_{,0x} & \frac{1}{0}w_{,0z} & 0 & \frac{1}{0}w_{,0x} \end{bmatrix} \quad (\text{B2})$$

\mathbf{A}_η

$$= \begin{bmatrix} \Delta u_{,0x} & 0 & 0 & \Delta v_{,0x} & 0 & 0 & \Delta w_{,0x} & 0 & 0 \\ 0 & \Delta u_{,0y} & 0 & 0 & \Delta v_{,0y} & 0 & 0 & \Delta w_{,0y} & 0 \\ 0 & 0 & \Delta u_{,0z} & 0 & 0 & \Delta v_{,0z} & 0 & 0 & \Delta w_{,0z} \\ \Delta u_{,0y} & \Delta u_{,0x} & 0 & \Delta v_{,0y} & \Delta v_{,0x} & 0 & \Delta w_{,0y} & \Delta w_{,0x} & 0 \\ 0 & \Delta u_{,0z} & \Delta u_{,0y} & 0 & \Delta v_{,0z} & \Delta v_{,0y} & 0 & \Delta w_{,0z} & \Delta w_{,0y} \\ \Delta u_{,0z} & 0 & \Delta u_{,0x} & \Delta v_{,0z} & 0 & \Delta v_{,0x} & \Delta w_{,0z} & 0 & \Delta w_{,0x} \end{bmatrix} \quad (\text{B3})$$

The displacement derivatives with respect to the natural coordinates are given by

$$\begin{Bmatrix} u_{,\xi} \\ u_{,\eta} \\ u_{,\zeta} \\ v_{,\xi} \\ v_{,\eta} \\ v_{,\zeta} \\ w_{,\xi} \\ w_{,\eta} \\ w_{,\zeta} \end{Bmatrix} = \begin{bmatrix} N_{1,\xi} & \cdots & N_{k,\xi} & 0 & 0 & \cdots & 0 \\ N_{1,\eta} & \cdots & N_{k,\eta} & 0 & 0 & \cdots & 0 \\ N_{1,\zeta} & \cdots & N_{k,\zeta} & 0 & 0 & \cdots & 0 \\ 0 & \cdots & 0 & N_{k,\xi} & 0 & \cdots & 0 \\ 0 & \cdots & 0 & N_{k,\eta} & 0 & \cdots & 0 \\ 0 & \cdots & 0 & N_{k,\zeta} & 0 & \cdots & 0 \\ 0 & \cdots & 0 & 0 & N_{k,\xi} & \cdots & N_{18,\xi} \\ 0 & \cdots & 0 & 0 & N_{k,\eta} & \cdots & N_{18,\eta} \\ 0 & \cdots & 0 & 0 & N_{k,\zeta} & \cdots & N_{18,\zeta} \end{bmatrix} \begin{Bmatrix} u_1 \\ \vdots \\ u_k \\ v_k \\ w_k \\ \vdots \\ w_{18} \end{Bmatrix} \quad (\text{B4})$$

$$= \mathbf{P} \mathbf{q}$$

$$\mathbf{P} = \begin{bmatrix} N_{1,\xi} & \cdots & N_{k,\xi} & 0 & 0 & \cdots & 0 \\ N_{1,\eta} & \cdots & N_{k,\eta} & 0 & 0 & \cdots & 0 \\ N_{1,\zeta} & \cdots & N_{k,\zeta} & 0 & 0 & \cdots & 0 \\ 0 & \cdots & 0 & N_{k,\xi} & 0 & \cdots & 0 \\ 0 & \cdots & 0 & N_{k,\eta} & 0 & \cdots & 0 \\ 0 & \cdots & 0 & N_{k,\zeta} & 0 & \cdots & 0 \\ 0 & \cdots & 0 & 0 & N_{k,\xi} & \cdots & N_{18,\xi} \\ 0 & \cdots & 0 & 0 & N_{k,\eta} & \cdots & N_{18,\eta} \\ 0 & \cdots & 0 & 0 & N_{k,\zeta} & \cdots & N_{18,\zeta} \end{bmatrix} \quad (\text{B5})$$

$$\mathbf{q} = \{u_1 \quad \cdots \quad u_k \quad v_k \quad w_k \quad \cdots \quad w_{18}\}^T \quad (\text{B6})$$

where \mathbf{P} and \mathbf{q} are the derivative matrix of the shape functions and the nodal vector of each element, respectively.

Appendix C

For isoparametric elements, geometry and displacements within the element are interpolated by the same shape functions. Thus, the geometry and internal displacements are interpolated from discrete nodal coordinates \mathbf{x}_e and displacements \mathbf{q}_e by

$$\mathbf{x} = \mathbf{N}\mathbf{x}_e \quad (C1)$$

$$\mathbf{u} = \mathbf{N}\mathbf{q}_e$$

where the shape function matrix \mathbf{N} is defined as

$$\mathbf{N} = \begin{bmatrix} N_1 & \cdots & N_k & 0 & 0 & \cdots & 0 \\ 0 & \cdots & 0 & N_k & 0 & \cdots & 0 \\ 0 & \cdots & 0 & 0 & N_k & \cdots & N_{18} \end{bmatrix} \quad (C2)$$

The matrix of angular velocity components contributing the Coriolis' force can be written as

$$\mathbf{\Omega}_1 = \begin{bmatrix} 0 & -2\Omega_z & 2\Omega_y \\ 2\Omega_z & 0 & -2\Omega_x \\ -2\Omega_y & 2\Omega_x & 0 \end{bmatrix} \quad (C3)$$

The matrix of angular velocity components contributing the centrifugal stiffness matrix can be written as

$$\mathbf{\Omega}_2 = \begin{bmatrix} \Omega_y^2 + \Omega_z^2 & -\Omega_y\Omega_x & -\Omega_z\Omega_x \\ -\Omega_x\Omega_y & \Omega_z^2 + \Omega_x^2 & -\Omega_z\Omega_y \\ -\Omega_x\Omega_z & -\Omega_y\Omega_z & \Omega_x^2 + \Omega_y^2 \end{bmatrix} \quad (C4)$$

Finally, the vector of angular velocity and blade coordinates contributing the centrifugal force vector is given by

$$\begin{aligned}
 \mathbf{\Omega}_3 &= \mathbf{\Omega}_2 \begin{Bmatrix} h_x + x \\ h_y + y \\ h_z + z \end{Bmatrix} \\
 &= \begin{Bmatrix} (\Omega_y^2 + \Omega_z^2)(h_x + x) - \Omega_y \Omega_x (h_y + y) - \Omega_z \Omega_x (h_z + z) \\ (\Omega_z^2 + \Omega_x^2)(h_y + y) - \Omega_z \Omega_y (h_z + z) - \Omega_x \Omega_y (h_x + x) \\ (\Omega_x^2 + \Omega_y^2)(h_z + z) - \Omega_x \Omega_z (h_x + x) - \Omega_z \Omega_y (h_y + y) \end{Bmatrix} \quad (C5)
 \end{aligned}$$

국문초록

3차원 유한요소를 이용한 회전 복합재 블레이드의 구조동역학 특성에 관한 연구

기영중

서울대학교 대학원

기계항공공학부

본 논문에서는 회전 복합재 블레이드의 구조동역학 해석모델 생성을 위해 18 절점을 갖는 고체 유한요소를 적용하였다. 해석모델의 특성으로 두께방향의 전단변형과 Coriolis 효과 및 복합재료의 연성 효과와 함께 보, 평판 및 셸 이론이 갖는 특정한 가정 없이 면 외 방향의 워핑 효과를 고려할 수 있도록 하였다. 또한, 대변형과 대회전의 특성을 고려하기 위해 증분 형태의 total-Lagrangian 수식화를 사용하여 정형화하였다. 회전 블레이드의 운동방정식을 유도하기 위해 Hamilton의 원리를 이용하였으며, 비선형 방정식의 해법으로 하중제어와 함께 Newton-Raphson 반복법을 적용하였다. 두께방향으로의 전단 잠김 현상의 문제를 방지하기 위해 수정된 형태의 응력-변형률 관계식을 이용하였으며, 전단 잠김 현상 없이 신뢰할 만한 수준의 해석결과를 획득할 수 있었다. 자유도 증가에 따른 계산량 부담을 감소시키기 위해 Guyan 및 IRS 감소법을 적용하였으며, 해석

결과의 정확도를 유지하면서도 해석에 소요되는 시간을 감소시킬 수 있었다. 본 연구를 통해 정립된 수식과 해석방안의 검증을 위해 획득된 수치 결과들을 참고문헌에 제시된 실험값과 다른 형태의 유한 요소를 이용하여 도출된 결과들과 함께 비교하였으며, 서로 잘 일치함을 확인하였다. 쉘 형태의 블레이드 모델의 경우 블레이드 곡률과 비틀림 각 및 기하학적인 비선형성이 회전 블레이드의 동적인 특성에 미치는 영향이 상당함을 확인하였다. ‘deep shell’ 모델의 경우 기하학적인 비선형성을 고려함에 따라 고유진동수 값이 감소하다 일정한 회전속도 이후에는 급격히 증가하는 ‘frequency loci veering’ 현상이 포착되었다. 또한, 직선형태의 가로세로비가 큰 블레이드의 경우 1차원 보 모델과 3차원 모델의 해석결과가 비슷한 수준이었으나, 가로세로비가 감소함에 따라 두 모델의 결과 값에 현저한 차이가 발생함을 확인하였다. 블레이드 끝단에 후퇴각이 적용된 블레이드의 경우 굽힘-비틀림 연성효과에 의해 플랩 모드의 고유진동수는 감소하는 경향을 나타내었으며, 후퇴각이 증가함에 따라 비틀림 모드의 고유진동수는 증가함을 확인하였다. 이와는 반대로 하반각이 적용된 블레이드에서는 하반각이 증가함에 따라 비틀림 모드의 고유진동수 값이 감소함을 확인하였다.

주제어: 기하학적 비선형성, 고체요소, 구조동역학 모델, 진동해석,

회전 복합재 블레이드

학 번: 2011-30946